國立臺灣大學理學院大氣科學所

博士論文

Department of Atmospheric Sciences
College of Science

National Taiwan University

Doctoral Dissertation

地形引發中尺度環流對燦樹颱風(2021)快速增強之影響

A Study on the Mesoscale Flows Induced by Taiwan Terrain and Their Impacts on the Rapid Intensification of Typhoon Chanthu (2021)

方偉庭

Wei-Ting Fang

指導教授：楊明仁博士 李清勝博士

Advisor: Ming-Jen Yang, Ph.D. Cheng-Shang Lee, Ph.D.

中華民國 113 年 7 月

July 2024

doi:10.6342/NTU202403267

doi:10.6342/NTU202403267

國立臺灣大學博士學位論文
口試委員會審定書

本論文係 方偉庭 君（學號 D05229002 ）在國立臺灣大學大氣科學學系、所完成之博士學位論文，於民國 113 年 7 月 15 日承下列考試委員審查通過及口試及格，特此證明

口試委員：楊明仁、李清勝（簽名）

（指導教授）

廖宇慶　　

吳俊傑　　王重傑

郭鴻基　　張保亮

　　

系主任、所長 游政谷（簽名）

致謝

「我都念成方伯了才變成方博」，是我口試結束後腦中的第一個想法。當初開始進修就只是某天突然腦袋被大王椰子敲到(誤)，覺得取得博士學位似乎是人生該完成的一件事，就這麼開始了漫漫學研之路。雖然花了很多時間才完成，但我想先感謝自己有堅持住並完成了這件大王椰子所帶來的靈感(大誤)。在楊明仁老師與李清勝老師兩位指導教授的教導下，我不但從中獲得許多知識，也讓我原本的作業導向思維，能轉換到學術的角度去思考問題，並在兩者之間取得平衡。也非常感謝年度考核與口試委員們給予許多指導與建議，都讓我的論文更加完整。

完成博士學位這路上承蒙多位貴人相助，內心只有滿滿的感激。首先要感謝單位對於進修的鼓勵與支持、NWP 小組的技術支援以及同事願意在我赴校進修時，幫我接那無窮無盡的電話。謝謝葳芃學姊在我博班生涯一開始就幫了大忙，讓我不至於在入學第一學期就得開始休學。保亮學長對我來說是個亦師亦友的角色，這段時間跟他合作得非常愉快，也一同發表了幾篇文章，說我的博士論文是他一路推著我寫完的也不為過。同期一起在職進修的同事們應該是最能理解彼此的感受，有時互相吐吐苦水，也算是忙碌生活中的一點小調劑。這邊也要對研究室的學弟妹說聲抱歉，身為大學長的我因為大部分時間都在工作單位，沒能給研究室的大家什麼幫助，謝謝大家的體諒。同時，也要感謝身邊一直默默鼓勵我的好朋友們與一起運動的夥伴們，每週短短幾小時運動加上閒聊的時間，是我唯一能忘記煩惱的時候。最後要感謝一直全力支持我的家人，是我最重要的精神支柱，沒有你們當我的強力後盾我一定沒辦法走到最後。

「可以畢業了是不是很開心？」，是我最近很常聽到的問題。但可能在職進修的關係，學校的事情對我來說並不是那麼有強烈的感覺，而學位取得與否對我的生活也不會有什麼改變，所以心情反而是很平靜的。最近很多人提醒我，博班畢業只是個開始不是結束，而我也漸漸的意識到這個事實。希望我能保持這份對研究的熱情，持續往前邁進，並在研究上繼續貢獻一己之力。

doi:10.6342/NTU202403267

摘要

本研究主題為探討地形引發中尺度環流對熱帶氣旋內核結構演變之影響。2021 年燦樹颱風在通過臺灣東部海面時強度快速增加，並伴隨眼牆對流顯著的波數 1 不對稱性，這些現象均透過臺灣密集的雷達網進行完整觀測。因此，藉由分析雷達回波、速度場以及地面測站資料，提供了本研究難得的機會，探討燦樹颱風內核結構的演變過程以及其與環境流場之關聯；並可針對此類結構極端扎實的颱風，進行雷達資料同化以探討模式渦漩初始化的議題。

為修正颱風強風造成雷達都卜勒速度的折錯問題，本研究首先發展 vortex-based Doppler velocity dealiasing (VDVD)演算法，針對雷達都卜勒速度場進行品質控管。此演算法使用理想渦漩做為參考風場進行反折錯，並搭配內迴圈以 ground-based velocity track display (GBVTD)技術調整颱風風場結構、外迴圈以 GBVTD-simplex 技術調整颱風中心的內外雙迴圈架構進行。結果顯示 VDVD 在理想個案或實際個案中，即使渦漩因為徑向風、平均流或渦漩本身切向風所造成的波數 1 不對稱風場結構，均可有效修正受折錯的速度場。燦樹颱風的雷達速度場資料經過 VDVD 與本研究所發展另一套修正局部折錯資料的方法處理後，可有效進行反折錯，以確保資料品質並進行後續的分析。

使用 GBVTD 反演燦樹颱風在 3 公里高度之切向風場顯示，其最大風速於增強階段時，在 11 小時內增加約 18 m s^{-1}，並於減弱階段在 8 小時內減少 19 m s^{-1}；顯示燦樹颱風在 24 小時內經歷了快速增強(rapid intensification)與快速減弱(rapid weaking)的過程，此類強度劇烈變化的個案為預報作業上的一大挑戰。在增強過程期間，燦樹颱風眼牆波數 1 不對稱性的最大值區域，由原本位於颱風中心東側，以氣旋式方向迅速移動至北側，此轉換過程恰好發生於地面測站資料觀測到地形繞流的訊號之後。另外，此波數 1 不對稱對流的軸向變化與雷達資料所反演的 meso-β 尺度垂直風切方向隨時間具有一致性；但由重分析資料計算而得的 meso-α 尺度垂直風切方向，則與眼牆對流分布不具一致性。顯示當外部強迫機制主要由

doi:10.6342/NTU202403267

地形所引發時， meso-β 尺度的垂直風切可較 meso-α 尺度垂直風切更具代表性。利用此 meso-β 尺度垂直風切搭配地面測站資料進行分析，本研究推測燦樹颱風的快速增強過程與 1) 地形引發在颱風南側之邊界層入流、2) 風向指向上風切左側象限的低層平均流以及 3) 較弱的高層風切有關。

本研究進一步使用數值模式搭配雷達資料同化探討如何對於燦樹颱風此類風場結構極端扎實的颱風進行渦旋初始化。將雷達都卜勒速度內插至模式網格後進行資料同化的 VRC 實驗顯示其模擬之渦漩的強度變化與雷達觀測較為接近，從 9 月 11 日 1100 UTC 持續增強至 9 月 12 日 0000 UTC，且眼牆對流演變亦與雷達觀測之圓形眼牆較為一致。VRP 實驗模擬之渦漩雖然於 9 月 11 日 1800 UTC 前展現較 VRC 實驗更快的增強速率，但後續強度則呈現緩慢減弱的趨勢，加上眼牆對流的波數 3 的不對稱性，均與觀測資料不一致。上述實驗顯示 VRC 的同化策略可較為合理模擬渦漩的內核演變過程；然而，VRC 實驗所模擬的垂直風切仍明顯較觀測資料為弱，不適合探討與風切相關的增強機制。因此，未來將藉由增加水平解析度與低層垂直解析度，對地形引發的 meso-β 尺度現象進行合理的模擬，以利後續定量評估造成燦樹颱風增強的主要物理機制。

doi:10.6342/NTU202403267

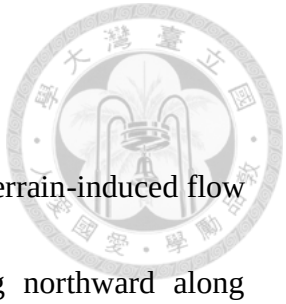

Abstract

The central theme of this study is to investigate the impacts of terrain-induced flow on the inner-core evolution of a tropical cyclone (TC) tracking northward along Taiwan's eastern coast. Typhoon Chanthu (2021) underwent rapid intensification (RI) and rapid weakening (RW) within the 24-hour analyzed period near Taiwan, posing challenges for intensity forecasts. Its intensification, characterized by a significant increase of 18 m s^{-1} at 3 km altitude within 11 hours and pronounced wavenumber-1 asymmetry in eyewall convection, was thoroughly observed by Taiwan's dense radar network. These comprehensive observations provide a valuable opportunity to explore the central theme of this study and the vortex initialization issue for such an extremely compact TC through radar data assimilation in numerical model simulation.

To address the challenge of recovering aliased Doppler velocities caused by strong TC winds, this study proposes a vortex-based Doppler velocity dealiasing (VDVD) algorithm specifically for TCs. The algorithm employs an inner-outer iterative procedure, adjusting the reference vortex structure using the ground-based velocity track display (GBVTD) technique, and utilizing the GBVTD-simplex algorithm for center correction. Both the VDVD and a local dealiasing method, also developed in this study, were applied to the aliased Doppler velocities. These methods effectively corrected the velocities and ensured the data were suitable for accurate analyses.

doi:10.6342/NTU202403267

Radar analyses for Typhoon Chanthu suggest that radar-derived meso-β scale vertical wind shear (VWS), which aligns better with the observed rotation of eyewall asymmetry, is more representative than meso-α scale VWS when terrain-induced forcing predominates. Further examination of the radar-derived VWS indicates that the VWS profile provided a more favorable environment for typhoon intensification. Observational analyses reveal that Chanthu's RI was influenced by three factors: 1) terrain-induced boundary inflow from the south of the typhoon; 2) upshear-left-pointing low-level mean flow; and 3) weak upper-level VWS.

To explore effective methods for initializing a compact TC vortex like Chanthu in numerical models, two radar data assimilation strategies were compared. The VRC experiment, which assimilates Doppler velocity interpolated onto the model grid, showed better consistency with radar observations regarding intensity change and eyewall evolution. In contrast, the VRP experiment, which assimilates thinned radar data in original coordinates, exhibited eyewall asymmetry dominated by a wavenumber-3 structure, differing from radar observations. However, the weak VWS in the VRC experiment, inconsistent with observations, hinders investigating intensification mechanisms. Future enhancements like increasing horizontal and vertical resolution are recommended to better capture meso-β scale features and assess the major mechanisms driving Chanthu's intensification.

doi:10.6342/NTU202403267

Table of Contents

doi:10.6342/NTU202403267

doi:10.6342/NTU202403267

List of Figures

doi:10.6342/NTU202403267

doi:10.6342/NTU202403267

doi:10.6342/NTU202403267

doi:10.6342/NTU202403267

doi:10.6342/NTU202403267

doi:10.6342/NTU202403267

doi:10.6342/NTU202403267

doi:10.6342/NTU202403267

doi:10.6342/NTU202403267

List of Tables

doi:10.6342/NTU202403267

1. Introduction

Taiwan is a mountainous island characterized geographically by the Central Mountain Range (CMR), which stretches south–north across most of Taiwan with the highest peak at approximately 4000 m. Consequently, as tropical cyclones (TCs) approach or move across Taiwan, terrain-influenced circulation frequently causes many unique features, such as extreme rainfall (Yang et al. 2008; Yang et al. 2011a,b; Yu and Cheng 2013; Wu 2013; Huang et al. 2014), the confluence of TC and secondary low-pressure circulation (Lee et al. 2008), track deflection/loop (Yeh and Elsberry 1993a,b; Jian and Wu 2008; Lin et al. 2002; Huang et al. 2011; Yeh et al. 2012; Hsu et al. 2018; Huang et al. 2020; Hsu et al. 2021), change in translation speed (Hsu et al. 2013), eyewall reintensification or reformation (Liou et al. 2016; Yang et al. 2018; Lin et al. 2020), coastal barrier jet (Kao et al. 2019), foehn winds (Chang and Lin 2011), and temporary intensification before making landfall with eyewall contraction (e.g., Jian and Wu 2008; Chang et al. 2009a; Chang et al. 2019; Kao et al. 2019).

The mechanisms for TC asymmetric structures are frequently dominated by environmental vertical wind shear (VWS), which is also highly connected to changes in TC intensity (e.g., Frank and Ritchie 2001; Corbosiero and Molinari 2003; Chen et al. 2006; Riemer et al. 2010; Ryglicki et al. 2021). A strong environmental VWS is considered a negative factor for TC intensification due to the vortex tilting and

doi:10.6342/NTU202403267

stabilization that it induces (DeMaria 1996). Additionally, the ventilation effect caused by VWS, which includes radial and downdraft pathways (Alland et al. 2021a, b, 2022), also exerts a negative impact on TC intensification. Meanwhile, TCs can still intensify under low to medium VWS environments (Rios-Berrios and Torn 2017), even undergoing RI through persistent convective bursts (CBs) in the inner-core region (Chen and Gopalakrishnan 2015; Heng et al. 2020). The sheared TCs may tilt toward the downshear side and consequently increase the eyewall convection asymmetry (Jones 1995; Frank and Ritchie 1999, 2001; Reasor et al. 2013). Studies conducting model simulations also indicate that the VWS-induced vertical differential advection to the vortex leads to ascent on the downshear side and descent on the upshear side (Jones 1995; Frank and Ritchie 1999, 2001). Therefore, the eyewall convection exhibits high wavenumber-1 asymmetry with a reflectivity maximum on the left-of-shear side.

A sudden change in the orientation of the eyewall wavenumber-1 asymmetry of TCs may be attributed to shifts in the direction of the VWS. Previous studies have extensively discussed the impact of terrain on the surrounding flow of TCs. Huang et al. (2019) indicated that TC tracks can be influenced when they are located within the typical distance range of 100 to 300 km from terrain. Simulations by Yeh and Elsberry (1993a, b) demonstrated that TC deflections occur when storms are approximately 200 km away from the terrain due to modifications in the mean steering flow induced by topographic

doi:10.6342/NTU202403267

barriers. Tang and Chan (2014, 2015) proposed that the presence of terrain can induce the formation of gyre pairs, leading to gyre-associated flow near the TC center that can influence the TC track prior to landfall. Wu et al. (2015) and Huang and Wu (2018) defined asymmetric flow as the mean state within a 50-km radius around the TC center, examining both the deep-layer mean and vertical distribution of asymmetric flows. Their findings revealed that as TCs approached Taiwan at a distance of approximately 200 km, terrain-induced asymmetric flows were primarily initiated below 625 hPa, while changes in the flow above this level were found to be insignificant. This suggests that terrain-induced flow can modulate the direction and magnitude of low-level flow, consequently modifying the VWS as well. Accordingly, estimating VWS that can properly capture the scale of environmental forcing where TCs are embedded is critical (Wong and Chan 2004; Reasor et al. 2009; Reasor and Eastin 2012; Reasor et al. 2013; Boehm and Bell 2021).

Under the shear-relative framework, a TC can be separated into downshear-left (DL), upshear-left (UL), upshear-right (UR), and upshear-left (UL) quadrants to discuss the inner core convective features induced by the VWS. The relative direction between the VWS and low-level mean flow (LMF) is also one of the essential factors for TC intensification. To investigate this issue during the tropical cyclogenesis stage, Rappin and Nolan (2012) conducted a numerical simulation. They found that if the orientations

doi:10.6342/NTU202403267

of the VWS and LMF were counteraligned (i.e., the LMF is upshear-pointing), the superposition of the TC main circulation and LMF induced a positive LMF anomaly and further moistened the boundary layer on the left-of-shear side. The moistened air parcels propagated cyclonically into the upshear region which promoted the axisymmetrization of the convection. This pattern has the potential to mitigate the vortex tilt and contribute to TC intensification. However, studies with opposite arguments have also been proposed. Chen et al. (2019) conducted idealized simulations with fixed Sea surface temperatures (SSTs) of 29.5 °C and 31.0 °C to investigate the effects of the direction of LMF under the same VWS on changes in TC intensity. The experiment with an SST of 31.0 °C was consistent with Rappin and Nolan (2012), but the experiment with an SST of 29.5 °C revealed a different result: a DL-pointing LMF is favorable for TC intensification. Chen et al. (2021) further used the European Centre for Medium-Range Weather Forecast (ECMWF) ERA5 reanalysis product (Hersbach et al. 2020) to examine the relationship between intensity change and LMF direction based on 720 TCs from multiple basins, and suggested that the DL-pointing LMF favors intensification.

In contrast to Rappin and Nolan (2012) and Chen et al. (2019), who initiated their simulations with relatively weak initial vortexes (less than 20 m s^{-1}), Lee et al. (2021) took a different approach by initiating their simulations with a strong vortex, starting at a strength of 70 kt. In their idealized experiments, they imposed a consistent 7.5 m s^{-1} VWS

doi:10.6342/NTU202403267

while manipulating the direction of the LMF. Results showed that the UL-pointing LMF prompted fast intensification by enhancing surface heat fluxes on the downshear side. These enhanced surface heat fluxes recovered the moist static energy of shear-enhanced downdrafts within the boundary layer over the inflow area. This recovery process prevents the TC eyewall from entraining low-energy air parcels. The convection in the UL quadrant can be maintained by reducing the downdraft ventilation (Alland et al. 2021a, b, 2022; Fischer et al. 2023). Consequently, the enhancement of axisymmetric heating benefits subsequent intensification.

According to the intensity data issued by the Joint Typhoon Warning Center (JTWC), Typhoon Chanthu (2021) intensified into a typhoon on Sep. 7 at 0600 UTC and reached its peak intensity with maximum sustained winds of 155 kts as it approached the ocean adjacent to northeastern Luzon Island in the Philippines (Table 1). Subsequently, it weakened slightly while passing through the Bashi Strait with a northwestward trajectory. After recurving towards the southeastern offshore area of Taiwan (Figure 1), its intensity further decreased to a maximum sustained wind of 130 kts. As Chanthu moved along and away from the east coast of Taiwan, intensity estimates from the Central Weather Administration (CWA), Japan Meteorological Agency (JMA), JTWC, and the Advanced Dvorak Technique (ADT) indicated that Chanthu either maintained its intensity or gradually weakened (Table 1).

doi:10.6342/NTU202403267

During this period, Chanthu was sequentially observed by the Ken-Ting (RCKT), Green Island (RCGI), Hua-Lien (RCHL), and Wu-Fen-Shan (RCWF) radars. Conversely, radar data indicated that Chanthu underwent a remarkable intensification, with an eyewall radius of 10–20 km, as it moved along the eastern coast of Taiwan at a distance of 100–150 km from the coast. The average distance between RCKT to RCGI, RCGI to RCHL, and RCHL to RCWF is approximately 100 km (Figure 1). This distribution of radar stations provided essential data for high spatial-temporal resolution analyses of the evolution of the TC inner core, including intensity changes and eyewall asymmetry during its passage. Consequently, Typhoon Chanthu offered a valuable opportunity to explore how the nearby terrain may have induced changes in TC intensity and the vortex initialization issue for such an extremely compact TC.

In this study, radar observations of Typhoon Chanthu were utilized to investigate the physical mechanisms underlying the dramatic changes in intensity and the evolution of the inner core during its passage near Taiwan. Single- and multiple-radar wind retrievals were performed to examine the evolution of the inner core structure and to discuss the relationship between eyewall asymmetry and radar-retrieved VWS. Additionally, numerical model simulations with radar data assimilation were utilized to explore effective methods for initializing such a compact TC in numerical models. This dissertation extensively employs the findings and methodologies detailed in two key

doi:10.6342/NTU202403267

journal articles. Chapter 2 introduces a vortex-based dealiasing algorithm, primarily based on the work presented in Chang et al. (2019), which is essential for improving radar wind field analysis. Chapter 3 focuses on the radar analysis and discussion of the rapid intensification of Typhoon Chanthu, as detailed in Fang et al. (2024). While most of the content from these articles is used in Chapters 2 and 3, some of the content is also incorporated into other chapters of this dissertation. Chapter 4 examines the methods for properly initializing a compact TC vortex, such as Typhoon Chanthu, by utilizing numerical model simulations with different radar data assimilation strategies. The final Chapter presents the conclusions and suggests directions for future work.

doi:10.6342/NTU202403267

Table 1. The intensity of Typhoon Chanthu (2021) issued by CWA, JMA, JTWC and estimated by ADT. The left and right columns under each official agency or objective method represent the minimum central pressure (hPa) and maximum sustained wind (m s^{-1}), respectively.

UTC		CWA		JMA		ADT		JTWC	
2021/9/10	00:00	925	53	935	55	940	54	928	69
	03:00	925	53	935	55	919	64		
	06:00	915	58	925	55	913	67	916	75
	09:00	915	58	920	55	885	78		
	12:00	915	58	910	60	885	78	911	77
	15:00	915	58	905	60	881	80		
	18:00	915	58	905	60	880	80	902	80
	21:00	920	55	905	60	880	80		
2021/9/11	00:00	925	51	905	60	884	78	915	75
	03:00	930	48	910	55	906	69		
	06:00	930	48	910	55	912	67	925	67
	09:00	940	45	910	55	918	64		
	12:00	940	45	920	55	925	60	945	57
	15:00	940	45	920	55	933	56		
	18:00	940	45	935	50	939	54	944	57
	21:00	940	45	935	50	939	54		
2021/9/12	00:00	940	45	935	50	944	51	948	54
	03:00	940	45	940	50	944	51		
	06:00	940	45	950	45	943	51	943	54
	09:00	940	45	955	45	961	42		
	12:00	945	43	960	40	961	42	949	49
	15:00	950	40	960	40	960	42		
	18:00	950	40	960	40	967	38	953	46

doi:10.6342/NTU202403267

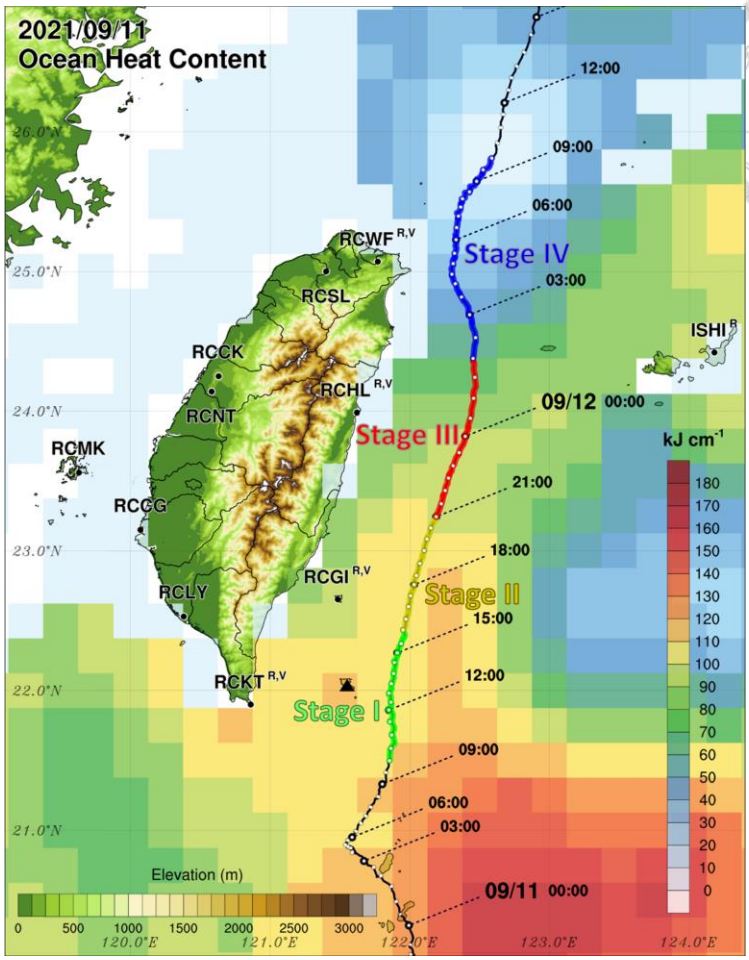

Figure 1. Track of Typhoon Chanthu (2021) determined by the tropical cyclone eye tracking (TCET) algorithm, overlaid with the distribution of ocean heat content (OHC) from the National Centers for Environmental Information (NCEI) on 11 Sep. Track covered by thick green, yellow, red and blue lines indicate the first intensifying (stage I), second intensifying (stage II), peak (stage III), and weakening stages (stage IV), respectively, as described in section 3.2. The numbers beside the tracks are the dates and times in UTC. The radars, for which the abbreviations with the superscript of "R" or "V" indicate the reflectivity or velocity, respectively, were used in this study for analysis. The black triangle denotes the location of the Lan-yu station on Orchid Island.

doi:10.6342/NTU202403267

2. Vortex-based Doppler velocity dealiasing algorithm

Doppler radars measure the velocity of precipitation particles along the viewing direction, and different flow patterns can be recognized from the signatures of the Doppler velocity field by employing pattern recognition approaches (e.g., Donaldson 1970; Wood and Brown 1992; Brown and Wood 2007). One of the most obvious characteristics observed in a Doppler velocity field for a vortex is a dipole signature. These approaches aid forecasters in preparing more accurate and timely warnings and short-term forecasts (Brown and Wood 2007).

To quantitatively retrieve winds from a single Doppler radar, many techniques have been proposed based on flow characteristics such as linear wind fields (Lhermitte and Atlas 1961; Waldteufel and Corbin 1979) and atmospheric vortices (e.g., Brown and Wood 1991; Lee et al. 1999; Jou et al. 2008). These algorithms provide good descriptions of weather events; however, applying these algorithms widely to all weather systems is difficult due to various flow patterns. For retrieving and constructing full three-dimensional wind fields, the multiple Doppler radar synthesis algorithms remain the most reliable techniques, although the analysis domain is limited to a particular region due to geometrical limitations (e.g., Lhermitte 1970; Frisch et al. 1974; Ray et al. 1975; Shapiro et al. 2009; Liou and Chang 2009).

Whether utilizing single- or dual-Doppler wind retrieval analysis, one of the

doi:10.6342/NTU202403267

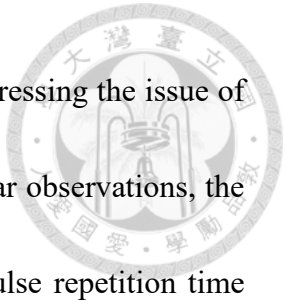

greatest challenges for both operational and research purposes is addressing the issue of velocity aliasing (folding) in the Doppler radar velocity field. In radar observations, the time interval between two successive pulses is referred to as the pulse repetition time (PRT) and is denoted by T_s. The Nyquist frequency can be represented by $(2T_s)^{-1}$, which is the highest frequency that can be unambiguously measured in the sampled sequence. This is because samples of a signal with a frequency $f > (2T_s)^{-1}$ have the same time dependence as a signal with $f < (2T_s)^{-1}$ (Doviak and Zrnic 1993). In addition, the Doppler velocity V_d is proportional to the Doppler frequency f and can be represented by

$$V_d = -\frac{f \cdot \lambda}{2}, \qquad (1)$$

where λ is the wavelength. Therefore, the radar velocity is folded when the Doppler frequencies exceed the maximum detectable frequency, resulting in Doppler velocity aliasing. Fundamentally, the observed Doppler velocity V_d and unfolded velocity V_u can be expressed by

$$V_u = V_d \pm 2n \times V_n, \qquad (2)$$

where n is an integer (0, 1, 2,...) and V_n represents the maximum unambiguous velocity, which is the Nyquist velocity.

In the dual-pulse repetition frequency (dual-PRF) technique, contiguous atmospheric volumes are probed at two different PRFs, and the two resulting velocity

doi:10.6342/NTU202403267

estimates are further processed to extend the Nyquist velocity (Altube et al. 2017). However, this technique can be compromised by various factors, such as strong horizontal wind gradients or the spread of the Doppler spectrum (Jorgensen et al. 2000; May 2001). Consequently, this procedure may lead to an increase in dealiasing failures and significantly affect the quality of radial velocity fields (Jorgensen et al. 2000; Altube et al. 2017). Furthermore, even if the radar operates in dual-PRF mode (Dazhang et al. 1984; Frush 1991; Loew and Walther 1995; Jorgensen et al. 2000) or multiple-PRT mode (Sirmans 1976; Zrnic and Mahapatra 1985; Tabary et al. 2006) to extend the maximum unambiguous velocity, the velocity folding problem in Doppler velocity observations remains unavoidable when observing very strong TCs and tornadoes.

Considering velocity based on upper air soundings or velocity azimuth displays (VADs), numerous algorithms (e.g., Eilts and Smith 1990; Gong et al. 2003) have been developed to adequately dealias the velocity for most weather events characterized by relatively uniform flow or widespread precipitation. Gong et al. (2003) combined gradient VAD (Tabary et al. 2001) and traditional VAD (Lhermitte and Atlas 1961) methods in VAD wind calculations with aliased velocities, without relying on external data. Zhang and Wang (2006) (hereafter ZW06) utilized the radial beam with minimum wind shear as an initial reference based on azimuthal continuity to initiate a dealiasing procedure in both clockwise and counterclockwise directions. However, dealiasing in

doi:10.6342/NTU202403267

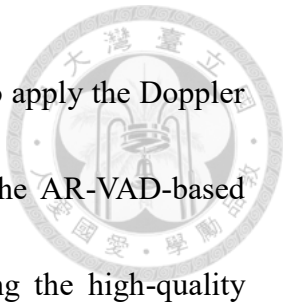

isolated and nearby terrain regions often lacks sufficient valid data to apply the Doppler velocity unfolding scheme effectively. Xu et al. (2011) proposed the AR-VAD-based dealiasing method to eliminate or prevent false dealiasing, meeting the high-quality standards and efficiency required for operational radar data assimilation. Nevertheless, the VAD uniform-wind approximation becomes poor or even invalid for intense rotational winds in a mesocyclone or hurricane core area, and for highly nonuniform winds near a sharp front. Therefore, dealiasing situations in environments characterized by high shear and curvature conditions, such as those in a mesocyclone and TC inner core, raise uncertainties when using a uniform-wind-based approximation, significantly reducing the performance of velocity dealiasing (ZW06; Xu et al. 2011).

To estimate the primary TC circulation, including the mean flow, axisymmetric tangential and radial winds, and asymmetric tangential winds, from single Doppler radar data, the ground-based velocity track display (GBVTD) technique was proposed as an objective approach for TC circulation retrievals (Lee et al. 1999). Since the GBVTD calculations are performed on a ring with a constant radius from the TC center, the quality of the GBVTD-retrieved TC circulation strongly depends on an accurate center position. Consequently, Lee and Marks (2000) proposed an algorithm using the simplex method to objectively estimate the TC vorticity center by maximizing the GBVTD-retrieved mean tangential wind. This method reduces uncertainties in

doi:10.6342/NTU202403267

estimating the TC center position and improves the quality of the GBVTD-retrieved TC circulation (Lee and Marks 2000; Bell and Lee 2002, 2012).

Focusing on the vortex circulation such as that of TCs, Wang et al. (2012) presented a gradient velocity track display (GrVTD) algorithm using aliased Doppler velocity data, achieving comparable results for the circulation structure to those obtained using the GBVTD algorithm based on manually dealiased Doppler velocity data. Since GrVTD uses only the gradient of Doppler velocity to accomplish wind retrieval, no dealiasing data can be extracted from the GrVTD algorithm, which could limit downstream applications and analyses for single- or dual-Doppler wind retrievals and radar data assimilations in real-time operations and research.

To enhance the accuracy of velocity dealiasing for TCs, this study proposes a vortex-based Doppler velocity dealiasing algorithm (VDVD) by integrating the GBVTD and GBVTD-simplex techniques with the Rankine combined vortex concept (e.g., Lemon et al. 1978; Wood and Brown 1992). The data and detailed methodology of the VDVD algorithm are described in the following section. Sensitivity tests and comparisons are provided in Section 2.2. The results and performance applications of the VDVD algorithm are discussed in Sections 2.3 and 2.4.

doi:10.6342/NTU202403267

2.1. Data and Methodology

2.1.1 Radar data

Currently the Central Weather Administration (CWA) and the Air Force Weather Wing in Taiwan operate a total of 10 weather radars (Figure 1): Wu-Fen-Shan (RCWF), Ken-Ting (RCKT), Hua-Lien (RCHL), Chi-Gu (RCCG), Ma-Kung (RCMK), Ching-Chuan-Kang (RCCK), Green Island (RCGI), Lin-Yuan (RCLY), Nan-Tuan (RCNT), and Shu-Lin (RCSL). Most of the radars (RCCK, RCMK, RCGI, RCLY, RCNT and RCSL) are operated in dual-PRF mode to increase the Nyquist (unambiguous) velocities. In contrast, the Nyquist velocities of those radars operated in single-PRF mode (RCWF, RCHL, RCCG, and RCKT) are less than 30.0 $\mathrm{m\,s^{-1}}$ (Table 2), and velocity folding is a problem when measuring wind speeds of very intense TCs.

As a consequence, an inadequate Doppler velocity dealiasing process would significantly raise the uncertainties of basic interpretations and downstream applications of TCs such as Doppler velocity pattern recognition, single- and dual-Doppler wind retrievals, and data assimilation. To improve the accuracy of velocity dealiasing for TCs for the radar observational domain, a vortex-based Doppler velocity dealiasing algorithm is proposed and discussed in the next section. The evaluation of the proposed dealiasing algorithm utilizes data from two S-band radars: RCWF (dual polarization) and RCHL (single polarization) (see Table 2).

doi:10.6342/NTU202403267

Table 2. Specifications of radar networks in Taiwan.

	RCWF	RCCG	RCKT	RCHL	RCLY
Observation Range of reflectivity/Doppler velocity at 0.5 degrees (km)	460/300	460/190	460/150	460/190	200/200
Elevation (m)	754	38	51	62	157
Wavelength (cm)	10	10	10	10	5
Polarization	Dual	Single	Single	Single	Dual
Nyquist Velocity (m s^{-1})	26.58	21.16	26.41	21.16	39.89
Location	25.07°N 121.77°E	23.15°N 120.07°E	21.90°N 120.85°E	23.99°N 121.63°E	22.53°N 120.38°E

	RCNT	RCSL	RCCK	RCMK	RCGI	ISHI
Observation Range of reflectivity/Doppler velocity at 0.5 degrees (km)	200/200	150/150	300/150	300/150	400/200	400/250
Elevation (m)	292	298	48	203	284	533.5
Wavelength (cm)	5	5	5	5	5	5
Polarization	Dual	Dual	Dual	Dual	Dual	Single
Nyquist Velocity (m s^{-1})	39.90	39.85	53.38	49.6	40.0	52.7
Location	24.14°N 120.58°E	25.00°N 121.40°E	24.25°N 120.63°E	23.56°N 119.63°E	22.65°N 121.48°E	24.43°N 124.18°E

2.1.2 Methodology

By combining the GBVTD and GBVTD-simplex techniques and profiles of the Rankine-like vortex (e.g., Lemon et al. 1978; Wood and Brown 1992) for TCs, the aliased Doppler velocity can be sequentially dealiased with the iterative procedures. In

doi:10.6342/NTU202403267

the VDVD algorithm, the radius of the maximum wind and the maximum velocity can be estimated from the GBVTD technique, and the circulation center can be estimated from the GBVTD-simplex technique. All the estimated information can then be applied to the Rankine-like vortex to extend that wind model to a larger radius.

Based on the original designs of the GBVTD and GBVTD-simplex algorithms, radar data should first be interpolated from raw data in polar coordinates (PPI, plan position indicator) to Cartesian coordinates (CAPPI, constant altitude plan position indicator) with the origin at the TC center. However, the aliasing points of the Doppler velocity can spread vertically and horizontally during this interpolation process. Additionally, even if a pre-dealiasing method is applied to eliminate contaminations from aliased Doppler velocity (Wang et al. 2012), converting dealiased data from CAPPI coordinates back to polar coordinates is irreversible. Consequently, the VDVD algorithm is calculated in polar coordinates to prevent data contamination by aliased velocity during interpolation into CAPPI coordinates.

The inner iterative loop of the VDVD algorithm is implemented to find a set of (V_{max}, R_{max}) to describe the TC structure that is used as a reference to dealias the Doppler velocity. However, an improper description of the TC structure (unrealistic asymmetric components) can be introduced by a displacement of the TC center (Lee et al. 1999), resulting in dealiasing failure. Therefore, the outer loop in the VDVD

doi:10.6342/NTU202403267

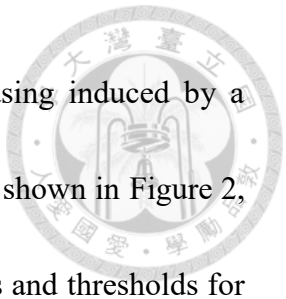

algorithm is designed to reduce the possibility of improper dealiasing induced by a shifted TC center. An overview flowchart of the VDVD algorithm is shown in Figure 2, and the default values or initial estimates of the empirical parameters and thresholds for the VDVD algorithm are listed in Table 3. The VDVD steps and parameters are described as follows:

1) Initially, estimate the vortex center (X^0, Y^0) with the origin at the radar site. At any given *n*-th iteration, the vortex center is represented as (X^n, Y^n).

2) Initially, estimate the radius of the maximum wind (RMW, $R_{max}^{n,0}$) and the maximum axisymmetric velocity ($V_{max}^{n,0}$). At any given *m*-th iteration, the RMW and maximum tangential velocity parameters are represented as $R_{max}^{n,m}$ and $V_{max}^{n,m}$, respectively.

3) Create a Rankine combined vortex profile via Eqs. (3) and (4) with (X^n, Y^n), $V_{max}^{n,m}$, $R_{max}^{n,m}$ and the predefined wind profile decay ratio (α).

$$V_T = V_{max}^{n,m} \frac{r}{R_{max}^{n,m}} \qquad if\ r \le R_{max}^{n,m} \qquad (3)$$

$$V_T = V_{max}^{n,m} \left(\frac{R_{max}^{n,m}}{r}\right)^{\alpha} \qquad if\ r \ge R_{max}^{n,m} \qquad (4)$$

where V_T is the tangential velocity at radius *r*.

4) Calculate the radial components of tangential velocities from step 3 in polar coordinates that are used as the references of Doppler velocities. The observed Doppler velocities are dealiased when the differences between the references of

doi:10.6342/NTU202403267

Doppler velocities exceed the criterion (1.5 times the Nyquist velocity) for individual radar bins in polar coordinates. The unfolded velocity V_u can be corrected from the observed Doppler velocity V_d with Eq. (2).

5) Calculate the $V_{max}^{n,m}$ and $R_{max}^{n,m}$ using the GBVTD algorithm with the unfolded Doppler velocity.

6) Verify whether the values between $V_{max}^{n,m}$ and $V_{max}^{n,m-1}$ and between $R_{max}^{n,m}$ and $R_{max}^{n,m-1}$ are identical. If yes, return to step 2 to continue the computation.

7) Use (X^n, Y^n) as the initial guess of the vortex center to calculate the new estimated vortex center (X^{n+1}, Y^{n+1}) with the GBVTD-simplex algorithm. The initial simplex search radius is set to 4 km, with a subsequent search process radius of 2 km repeated to achieve higher vortex center precision. Other parameters follow those outlined in Lee and Marks (2000).

8) Verify whether the difference between (X^n, Y^n) and (X^{n-1}, Y^{n-1}) exceeds the prescribed criterion C_0. If yes, return to step 1 to continue the computation. Otherwise, the iterative procedures stop.

doi:10.6342/NTU202403267

Table 3. Default values or initial estimates of the VDVD

Parameter	Value
$V_{max}^{n,0}$	Nyquist velocity (m s^{-1})
$R_{max}^{n,0}$	20 km
X^0, Y^0	X^n, Y^n at the previous time frame (from a forecast if the previous one is unavailable)
C_0	10 km
α	0.6

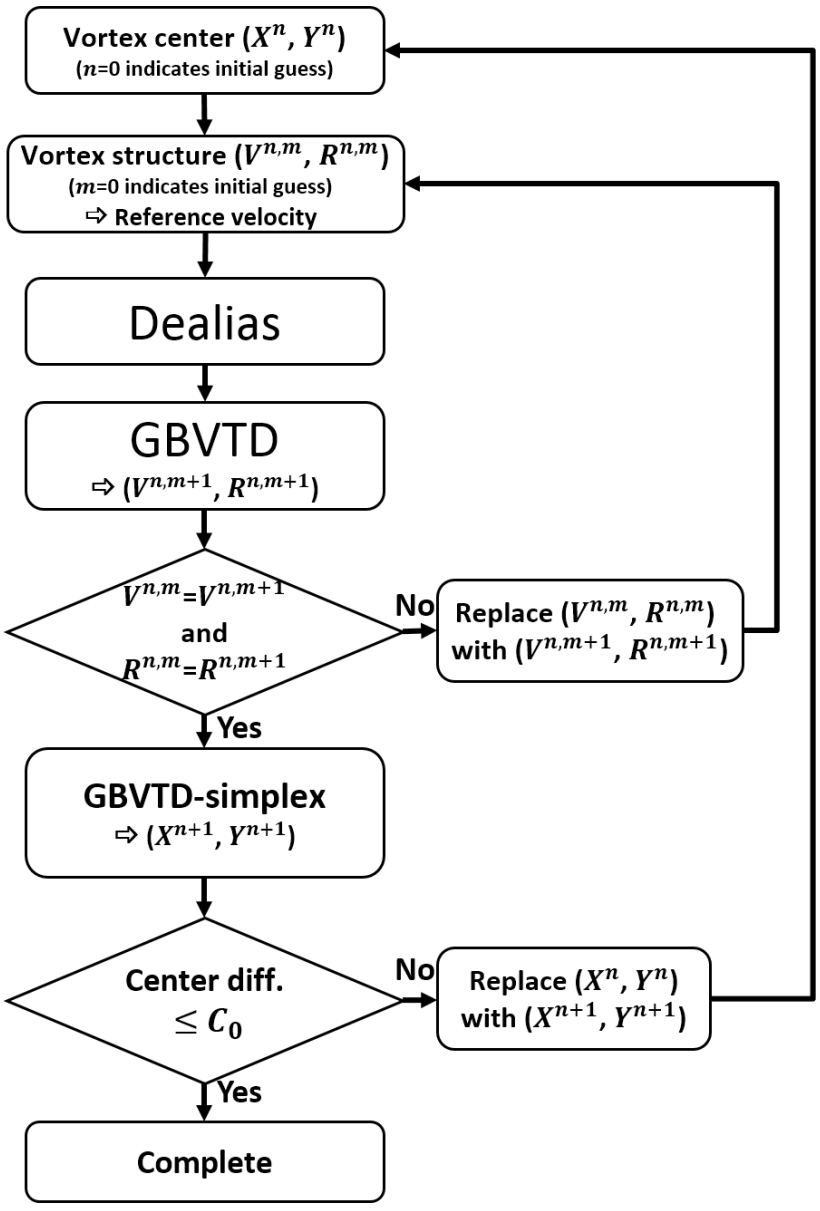

Figure 2. Overview flowchart of the VDVD algorithm.

doi:10.6342/NTU202403267

2.2. Sensitivity Tests

Based on the procedures described in the previous section, an analytic dataset is used for the sensitivity tests. This dataset is constructed at 0.25 km (radial) by 0.5 degrees (azimuth) to a range of 230 km and elevation angle of 0.5 degrees in polar coordinates. The Nyquist velocity (V_n) is set to 25 m s^{-1}, which is which is comparable to the lower value in the Taiwan radar network. The symmetrical vortex is represented as a Rankine combined vortex, with V_{max}= 60 m s^{-1}, R_{max}= 40 km and $\alpha = 0.5$, as shown in Figure 3a. Additionally, the axisymmetric radial flow V_R is constructed based on the following assumption used in Lee et al. (1999), which is similar to the pattern documented in Jorgensen (1984a, b):

$$V_R = C_1[(R_{max} - R)R]^{1/2} \qquad R \le R_{max}^m \quad (5)$$

$$V_R = -C_2(R - R_{max})^{1/2}R_{max}/R \qquad R > R_{max}^m \quad (6)$$

The values of C_1 and C_2 in Eqs. (5) and (6) are 0.1 s^{-1} and 3 m$^{0.5}$ s^{-1}, respectively, for V_R calculations, which are the same values set in Lee et al. (1999). The V_T asymmetry (V_{T1}) is represented by a wavenumber 1 pattern with an amplitude of 20% of V_T at a phase of 0° or 90°. The mean flow (V_M) is set to 5 m s^{-1} or 10 m s^{-1} with various directions from 0° to 360° at 90° intervals. All the sensitivity tests discussed in the following subsections in this study were conducted by referring to the experiments in Lee et al. (1999) and are summarized in Table 4. Subsections 2.2.1-2.2.4

doi:10.6342/NTU202403267

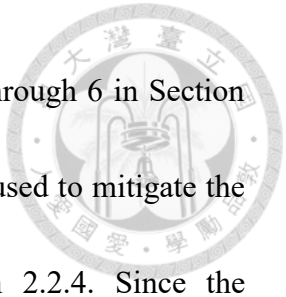

introduce the dealiasing ability of the inner iterative loop (steps 2 through 6 in Section 2.1.2). The outer iterative loop (steps 1 through 8 in Section 2.1.2), used to mitigate the effect of a displaced vortex center, is described in Subsection 2.2.4. Since the discussions in Subsections 2.2.1-2.2.4 use only the inner loop, the notations of V_{max} and R_{max} are simplified by using V_{max}^{m} and R_{max}^{m} instead of $V_{max}^{n,m}$ and $R_{max}^{n,m}$.

Table 4. Sensitivity tests of the inner loop of the VDVD algorithm for various combinations of V_T, V_{T1}, V_R, and V_M (see details in the text). The iteration number in boldface indicates that the test is not completely dealiased. Success rate indicates the ratio of the tests which are successfully dealiased.

	$\boldsymbol{V_{T1}}$ **(20%$\boldsymbol{V_T}$) (0°/90°)**	$\boldsymbol{V_R}$	$\boldsymbol{V_M}$ **(5 m $\boldsymbol{s^{-1}}$) (0°/90°/180°/270°)**	$\boldsymbol{V_M}$ **(10 m $\boldsymbol{s^{-1}}$) (0°/90°/180°/270°)**	**iteration**	**Success rate**
A00					2	100%
A01	✓				3/4	100%
A02		✓			2	100%
A03			✓		3/2/3/2	100%
A04				✓	4/3/4/2	100%
A05	✓	✓			3/4	100%
A06	✓		✓		4/3/4/3/ 3/4/5/4	100%
A07	✓			✓	6/3/7/3/ 3/4/10/3	100%
A08	✓	✓	✓		4/3/4/3/ 3/4/6/4	100%
A09	✓	✓		✓	***6***/3/7/3/ 3/4/12/3	82.5%

doi:10.6342/NTU202403267

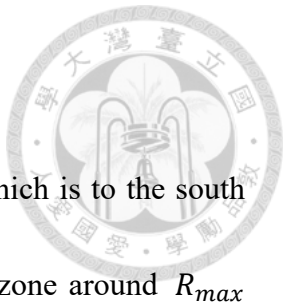

2.2.1 Rankine combined vortex

The analytic axisymmetric vortex is located at (0.0, -150.0), which is to the south of the radar at (0, 0). The clear cyclonic flow field and high wind zone around R_{max} centered at the vortex center are illustrated in Figure 3a. The V_{max} and R_{max} of the Rankine combined vortex and the GBVTD-derived results in each iteration are shown in Table 5 and Figures 3b-f, respectively. In the initial iteration, the reference vortex (Figure 3b) is significantly different from the simulated vortex , resulting in only partial dealiasing of the Doppler velocities from the raw data (Figure 3d), with aliased velocities still present near the eyewall (Figure 3e). The GBVTD-derived V_{max} and R_{max} values are 43.19 m s^{-1} and 29 km, respectively, closer to the simulated vortex values (V_{max}= 60 m s^{-1}, R_{max}= 40 km) than the initial estimates (V_{max}^{0}= 25 m s^{-1}, R_{max}^{0}= 20 km). The differences (ΔV and ΔR) are 18.19 m s^{-1} and 9 km, respectively. In the second iteration, the GBVTD-derived values (V_{max}^{1} and R_{max}^{1}) are 60.08 m s^{-1} and 40 km, respectively, very close to the simulated vortex values. With no differences between (V_{max}^{0}, R_{max}^{0}) and (V_{max}^{2}, R_{max}^{2}), the iterations stop after the third iteration. When combining axisymmetric V_T and V_R (Figure 4a), the flow field shows no significant difference, but the velocity dipole rotates slightly clockwise (Figure 4d). Figures 4d-f show that the extra V_R component does not increase the number of iterations due to its relatively small magnitude compared to V_T. With this symmetric

doi:10.6342/NTU202403267

vortex, the aliased Doppler velocity is correctly recovered in only three iterations.

To further investigate the performance of the initial estimates V_{max}^0 and R_{max}^0 for the initial reference vortex, a range of V_{max}^0 of 1-80 m s^{-1} and R_{max}^0 of 1-80 km were used to understand how the procedure guides V_{max}^0 and R_{max}^0 to approach the actual V_{max} and R_{max}. A convergent feature diagram presents the convergence path and tendency during the iteration calculations. The differences ($\Delta Vs, \Delta Rs$) between all the (V_{max}^0, R_{max}^0) and (V_{max}^1, R_{max}^1) are calculated and illustrated in vector form (Figure 5a). Nearly all vectors point toward V_{max}= 60 m s^{-1} and R_{max}= 40 km , with adjustments being less significant when the initial guesses (V_{max}^0,R_{max}^0) are closer to the true values. This diagram reveals that most combinations of V_{max}^0 and R_{max}^0 are suitable for initial estimates. However, extreme combinations of high V_{max}^0 and low R_{max}^0 or high V_{max}^0 and high R_{max}^0 could result in an irreversible unfolding process. When combining axisymmetric V_T and V_R (Figure 5b), the convergence paths are similar to those of V_T, pointing toward the given values of the simulated vortex (V_{max}= 60 m s^{-1} and R_{max}= 40 km).

doi:10.6342/NTU202403267

Table 5. GBVTD derived V_{max} (m s^{-1}) and R_{max} (km) at each iteration

Iteration	$V_{max}^{n,m}$	$R_{max}^{n,m}$	$V_{max}^{n,m+1}$	$R_{max}^{n,m+1}$
0	25.0	20	43.99	29
1	43.99	29	60.08	40
2	60.08	40	60.08	40

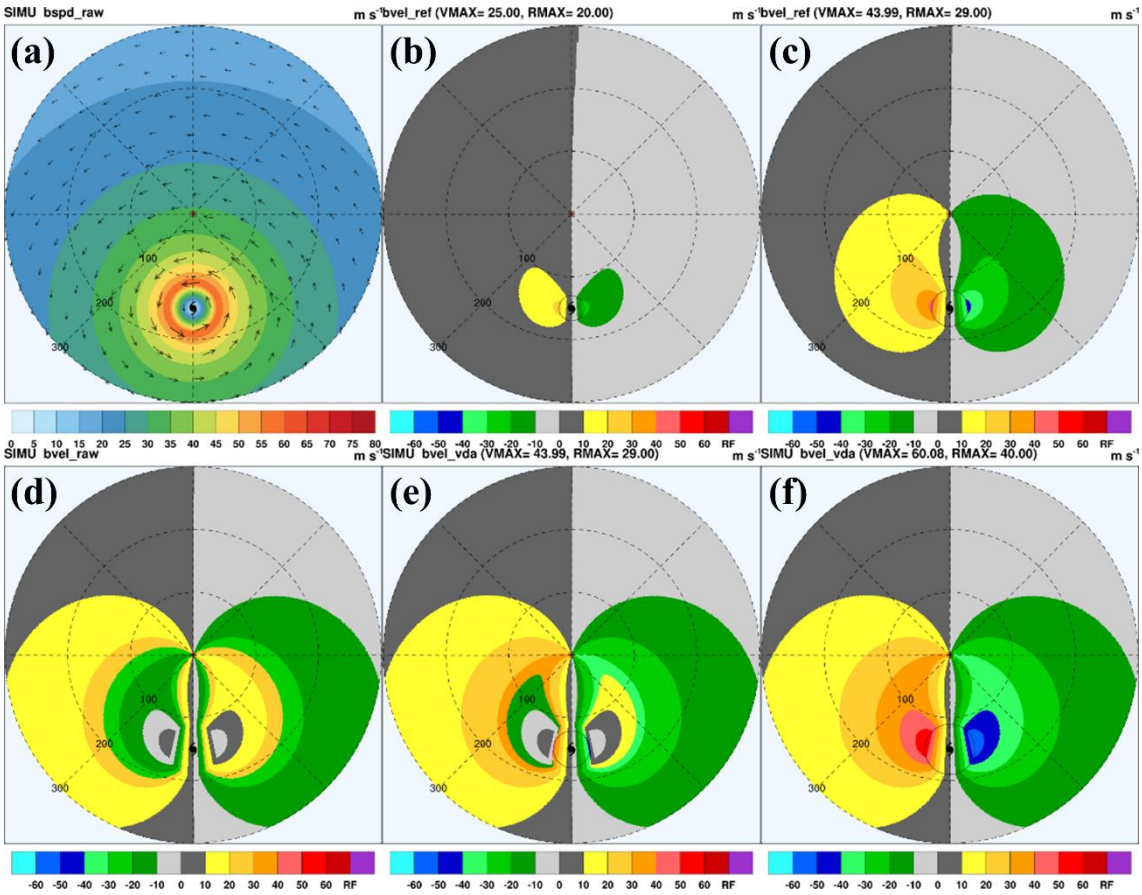

Figure 3. (a) Axisymmetric V_T flow field and (d) its projected Doppler velocity. (b) The initial reference Doppler velocity in iteration 0, with the R_{max} and V_{max} listed in Table 3, used to dealias (d). The dealiased field in interation 0 is shown in (e). (c) The reference Doppler velocity in iteraion 1, with the R_{max} and V_{max} retrieved from (e) utilizing the GBVTD algorithm. (c) is then utilized to dealiase (e) and generate (f) the final dealiasd velocity. The color scale indicates the amplitude, and the gray circle centered on the typhoon symbol indicates the maximum wind radius.

doi:10.6342/NTU202403267

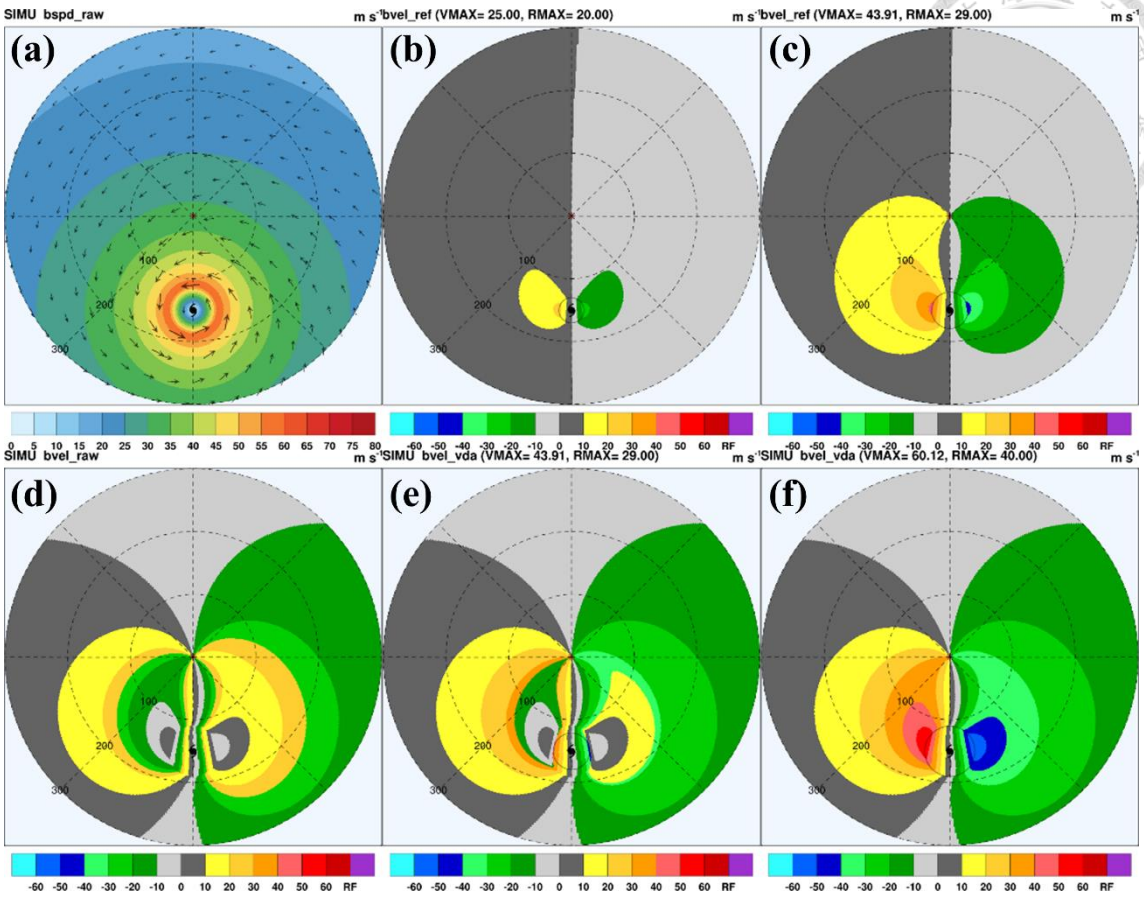

Figure 4. Same as in Figure 3 but for the superposition of the axisymmetric V_T and V_R.

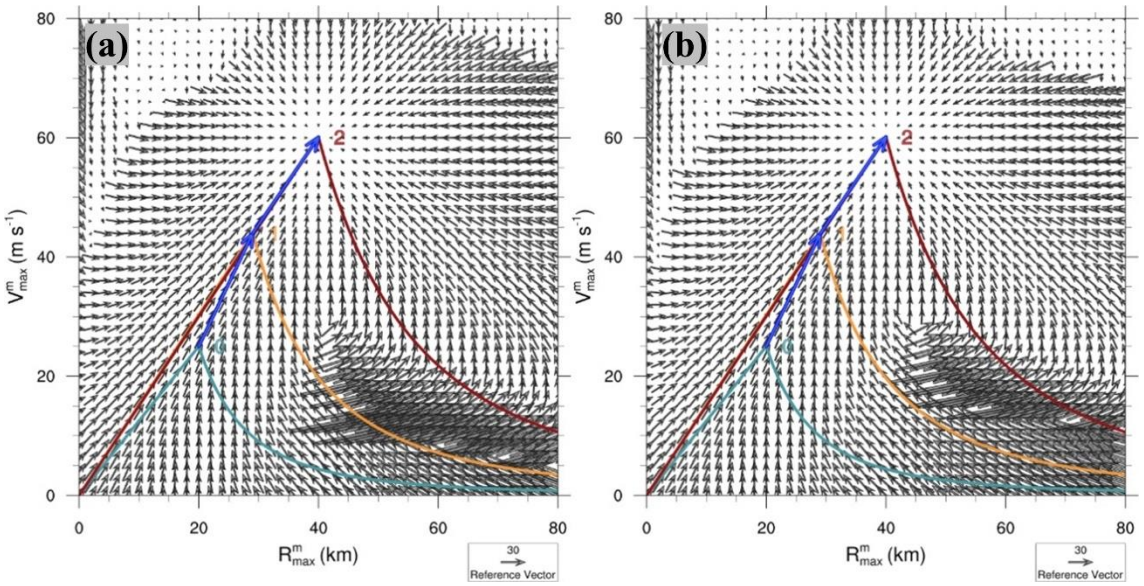

Figure 5. The convergent feature diagram for (a) axisymmetric V_T and (b) the superposition of the axisymmetric V_T and V_R. The arrows in black show the iteration path. The Rankine combined wind profiles used in consecutive iterations are indicated by solid lines and iteration numbers based on an initial estimate. The color scale indicates the square root of the sum of the differences between the estimated and true value of R_{max} and V_{max} during the calculations (see the text for details).

doi:10.6342/NTU202403267

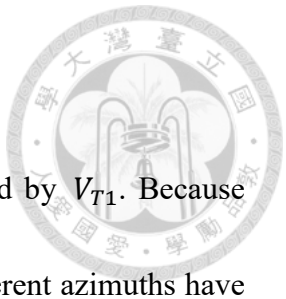

2.2.2 Effect of Doppler velocity asymmetry

The first part of this section emphasizes the asymmetry caused by V_{T1}. Because the conditions of the wavenumber 1 component of V_T (V_{T1}) on different azimuths have similar influences on testing the asymmetric effects between 0° (90°) and 180° (270°) relative to the vortex center, V_{T1} values located at azimuths 0° and 90° superimposed on the basic flow (Rankine combined vortex) are chosen to examine the effects of asymmetry. Figure 6a shows that the Doppler velocity pattern for V_{T1} at 0° is antisymmetric with respect to the y axis , with the peak magnitude in the Doppler velocity dipole being approximately 5 -10 m s^{-1} higher than that in the basic flow. The final V_{max} and R_{max} values derived from the GBVTD algorithm are 61.64 m s^{-1} and 40 km, respectively, which are very close to the idealized vortex values (Figure 6b). The convergent feature diagram also shows that nearly all vectors are pointing toward V_{max} = 60 m s^{-1} and R_{max} = 40 km (Figure 6c). However, it also indicates a potentially irreversible unfolding process under conditions of a higher V_{max} with a smaller R_{max}, which could result in inadequate dealiased Doppler velocity. The Doppler velocity pattern for V_{T1} at 90° is shown in Figure 6d. An obvious asymmetric pattern for the Doppler velocity dipole is observed , with a difference of approximately 20 m s^{-1} between the peak magnitudes of inbound and outbound Doppler velocities. Similar to the results shown in Figure 6b, the aliased Doppler velocity can be recovered by the

doi:10.6342/NTU202403267

inner loop of the VDVD algorithm (Figure 6e), while the number of iterations is four (Figure 6f), slightly higher than that in Figure 6c due to the asymmetry in the Doppler velocity field.

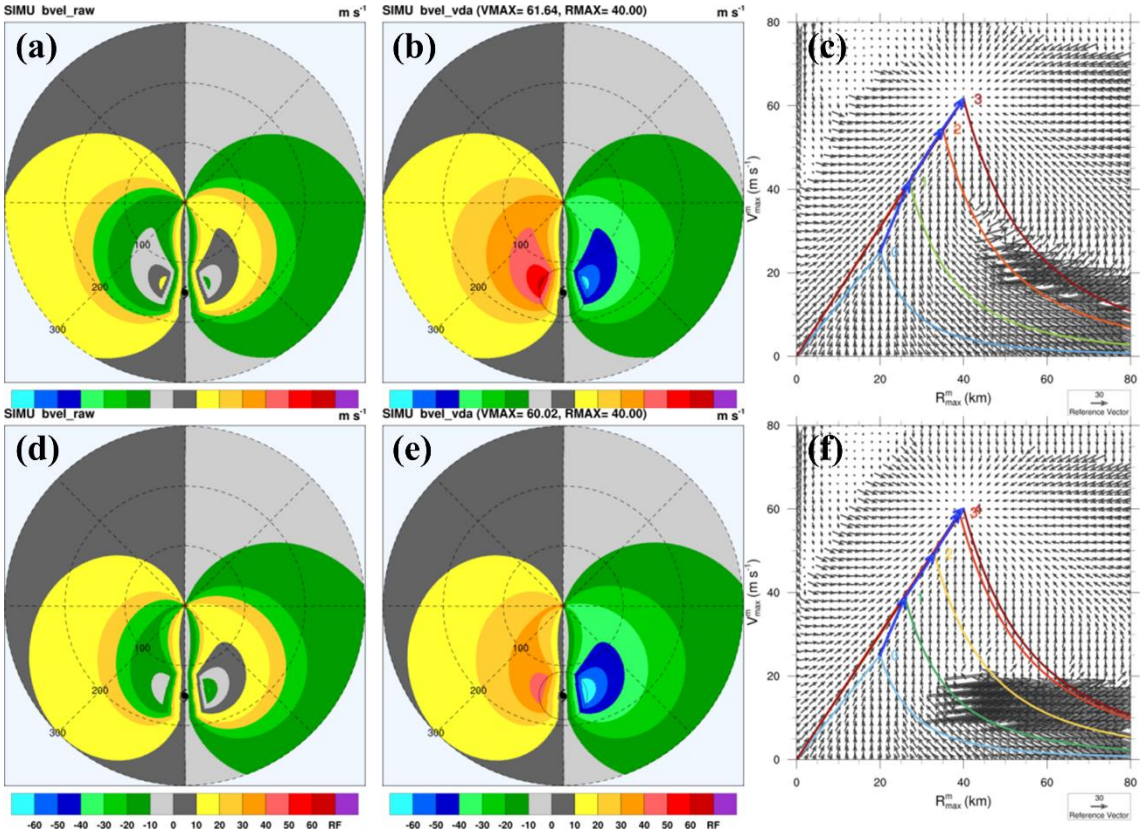

Figure 6. (a) Doppler velocity fields of the original, (b) final iteration, and (c) the convergent feature diagram for the superposition of the axisymmetric V_T and V_{T1} at 0°. (d), (e) and (f) are the same as (a), (b) and (c) but for the superposition of the axisymmetric V_T and V_{T1} at 90°.

The second part of this section focuses on the asymmetry caused by V_M. The Doppler velocity patterns are characterized by the directions of V_M. Figure 7 presents the Doppler velocity patterns of 10 m s^{-1} along-beam northerly and cross-beam easterly V_M components superimposed on the axisymmetric V_T flow. The definitions of the

doi:10.6342/NTU202403267

along- and cross-beam are consistent with those in Lee et al. (1999). When combining the along-beam V_M (Figure 7a), the zero isodop of Doppler velocity and the peak magnitude of the Doppler velocity dipole show remarkable change compared to those from the cross-beam V_M (Figure 7d). The easterly V_M enhances the Doppler velocity of the axisymmetric vortex because the effect is a function of the beam angle, as documented in Lee et al. (1999).

The final V_{max} and R_{max} values derived from the GBVTD are 60.08 (62.78) m s^{-1} and 40 (40) km, respectively, for northerly (easterly) V_M components (Figure 7b and Figure 7e). The final V_{max} is slightly greater than the analytic vortex due to the uncertainty in retrieving the V_{max} from the GBVTD when the cross-beam V_M component is superimposed with basic flow (Lee et al. 1999). Despite this slight overestimation, the VDVD performs well because the tolerance of the difference (1.5 times the Nyquist velocity) between the reference and aliased velocities is relatively large (Eq. 2).

doi:10.6342/NTU202403267

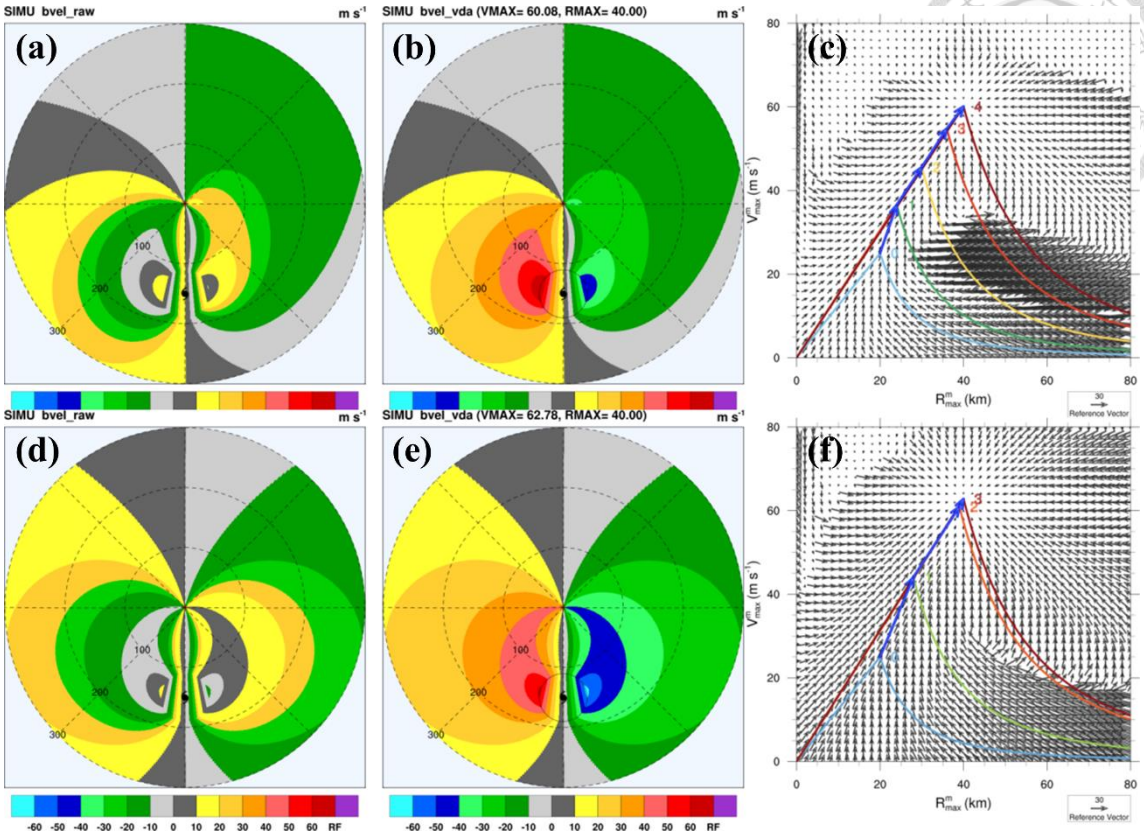

Figure 7. Same as in Figure 5 but for (a), (b), (c) the superposition of the axisymmetric V_T and northerly V_M, and (d), (e), (f) the superposition of axisymmetric V_T and easterly V_M.

doi:10.6342/NTU202403267

The third part of this section highlights the asymmetry caused by the combined effects. To further evaluate the performance and limitations of the VDVD algorithm, all the axisymmetric and asymmetric components are superimposed on the Rankine combined vortex to create an analytic dataset. Figure 8 presents two representative examples with extreme asymmetry of the Doppler velocity pattern combined V_T with 1) 20% V_T as V_{T1} at azimuth 0°, V_R, and 10 m s^{-1} northerly V_M and 2) 20% V_T as V_{T1} at azimuth 90°, V_R, and 10 m s^{-1} southerly V_M.

For the first test (Figure 8a), the Doppler velocity field is characterized by a bending zero isodop and asymmetric dipole structure. The final V_{max} and R_{max} values derived from the GBVTD algorithm are 61.68 m s^{-1} and 40 km, respectively (Figure 8b). Although these values approximate the true vortex values, the aliased Doppler velocities in a limited area near the northwestern direction at a range of approximately 70 km from the vortex center cannot be well recovered. This failure is due to the high asymmetry of the combined vortex contributed by V_{T1} in the northern vortex and the northerly V_M superimposed on symmetric V_T flow. The convergent feature diagram (Figure 8c) shows the conversion paths for vectors similar to those in Figures 7-8, but the number of iterations increases to 8.

The asymmetric Doppler velocity structure for the second test is shown in Figure 8d. The magnitude difference between peak inbound and outbound Doppler velocities

doi:10.6342/NTU202403267

reaches approximately 30 m s^{-1}. Even under such extreme conditions, the VDVD successfully recovers the aliased Doppler velocities. The final V_{max} and R_{max} values derived from the GBVTD algorithm are 60.07 m s^{-1} and 40 km, respectively (Figure 8e), values closer to the simulated vortex values than those from the first test. However, the number of iterations increases to 12 (Figure 8f) , considerably higher than in previous tests. This finding suggests that a more asymmetric Doppler velocity dipole requires a greater number of convergence iterations.

Table 4 summarizes the sensitivity tests for various combinations from the wavenumber 1 of V_T (V_{T1}) given with 20% of V_T and V_M given with a value of 5 m s^{-1} and 10 m s^{-1} with various directions from 0 to 360°. The results show that the number of iterations is less than 5 and generally increases with the vortex asymmetry. This finding indicates that the aliased velocities from almost all the tests can be recovered by the VDVD algorithm except the first experiment in test A09 shown in Figure 8b, which is combined with symmetric V_T, V_R, asymmetric V_{T1} at azimuth 0°, and northerly V_M. The unsuccessful recovery of aliased Doppler velocity in this test occurs because the simulated vortex is far from the Rankine vortex assumption when the direction of V_M is parallel to the radar beam. The aliased Doppler velocity can be successfully corrected with a V_M of 5 m s^{-1} in all directions due to the reduced asymmetry in the analytic vortex. In practice, the uncertainty in dealiasing Doppler velocity increases with higher

doi:10.6342/NTU202403267

V_M values. This uncertainty could be mitigated by incorporating the short-term motion of TCs or previous V_M analysis from the GBVTD algorithm.

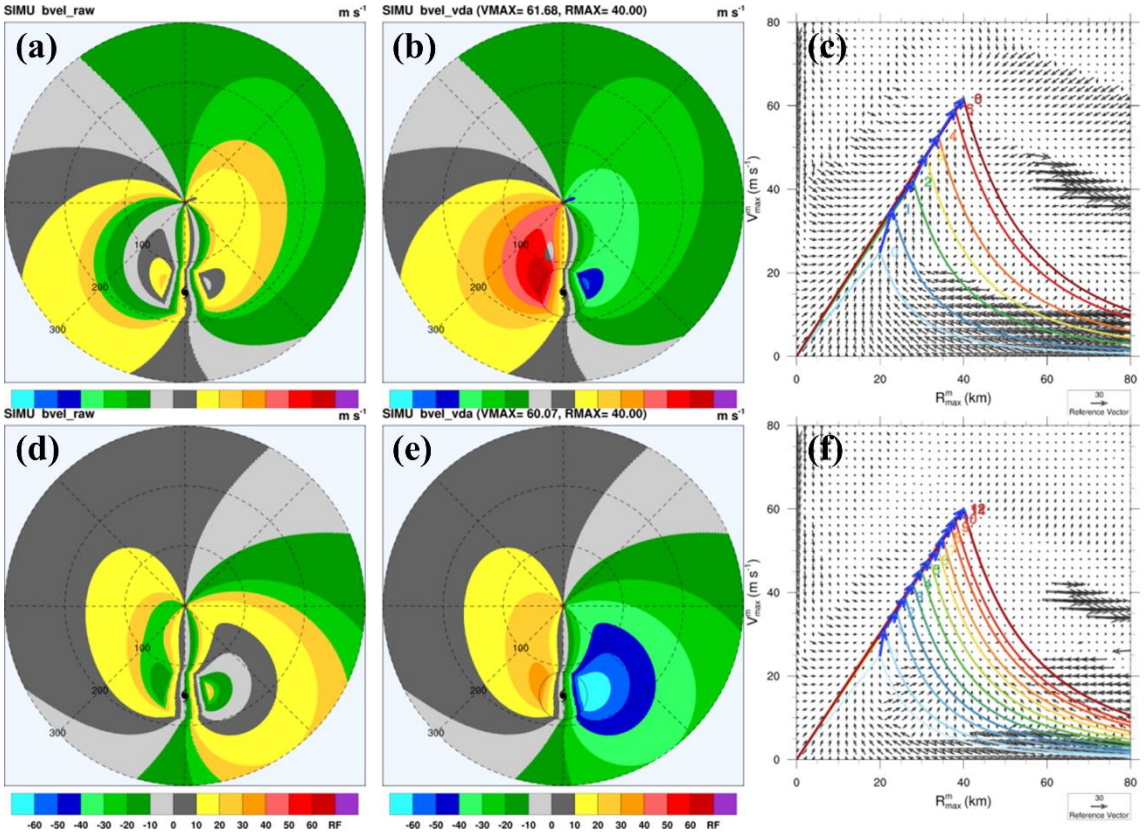

Figure 8. Same as in Figure 5 but for (a), (b), (c) the superposition of the axisymmetric V_T, V_R, V_{T1} at 0°, and northerly V_M, and (d), (e), (f) the superposition of the axisymmetric V_T,V_R, V_{T1} at 90°, and southerly V_M.

doi:10.6342/NTU202403267

2.2.3 Effect of TC center displacement

The subsections above focus on the sensitivities of the inner loop in the VDVD algorithm with the correct vortex center. The sensitivity for the effect of vortex center displacement is discussed in this subsection. From the overview flowchart of the VDVD algorithm (Figure 2), the necessary inputs of the initial estimation are the vortex center location (X^0, Y^0), V_{max}^0, and R_{max}^0. In practice, typhoon centers can be provided by the best track analysis, which is issued every hour by the CWB in Taiwan, for example. However, this track information usually has a 20-30 minute timing delay because it takes time to integrate the information from all available data such as radar, satellite, and surface observations. Alternatively, the approximate center position can be estimated using the current TC center location, and the track can be forecasted with a linear extrapolation.

The vortex asymmetry, especially for the wavenumber-1 structure that is computationally generated during the GBVTD calculation, exhibits a displacement of the TC center of an axisymmetric vortex, as documented by Lee and Marks (2000). To simulate the effect of a shifted vortex center in the inner loop of the VDVD algorithm, four experiments are conducted with a displacement of 8 km (20% of simulated RMW) in 4 directions (north, east, south, and west) from the true value based on the analytics vortex shown in Section 2.2.1 and Figure 3a. All the experiments reveal obvious

doi:10.6342/NTU202403267

convergence patterns, and the convergence approximately points to the given values of the idealized vortex ($V_{max} = 60\ m\ s^{-1}, R_{max} = 40\ km$) (Figure 5). The aliased Doppler velocities can be recovered by the reference wind field based on those approximated V_{max} and R_{max} values even at a weaker V_{max} and larger R_{max}. It is shown that the R_{max}^{m} and V_{max}^{m} gradually increase toward the true values. The ΔVs are greater than ΔRs in magnitude initially but are contrary at the end of iteration. An obvious curved convergence path is presented that is slightly different from that in Section 2.2.1 (Figure 5). Generally, a displacement of the vortex center makes the convergence pattern less significant and increases the number of iterations during the structure-finding procedure in this sensitivity test of the VDVD algorithm. However, the uncertainty of the VDVD algorithm tends to increase with a larger center displacement, potentially leading to a failure in convergence. (discussed in the Section 2.4).

doi:10.6342/NTU202403267

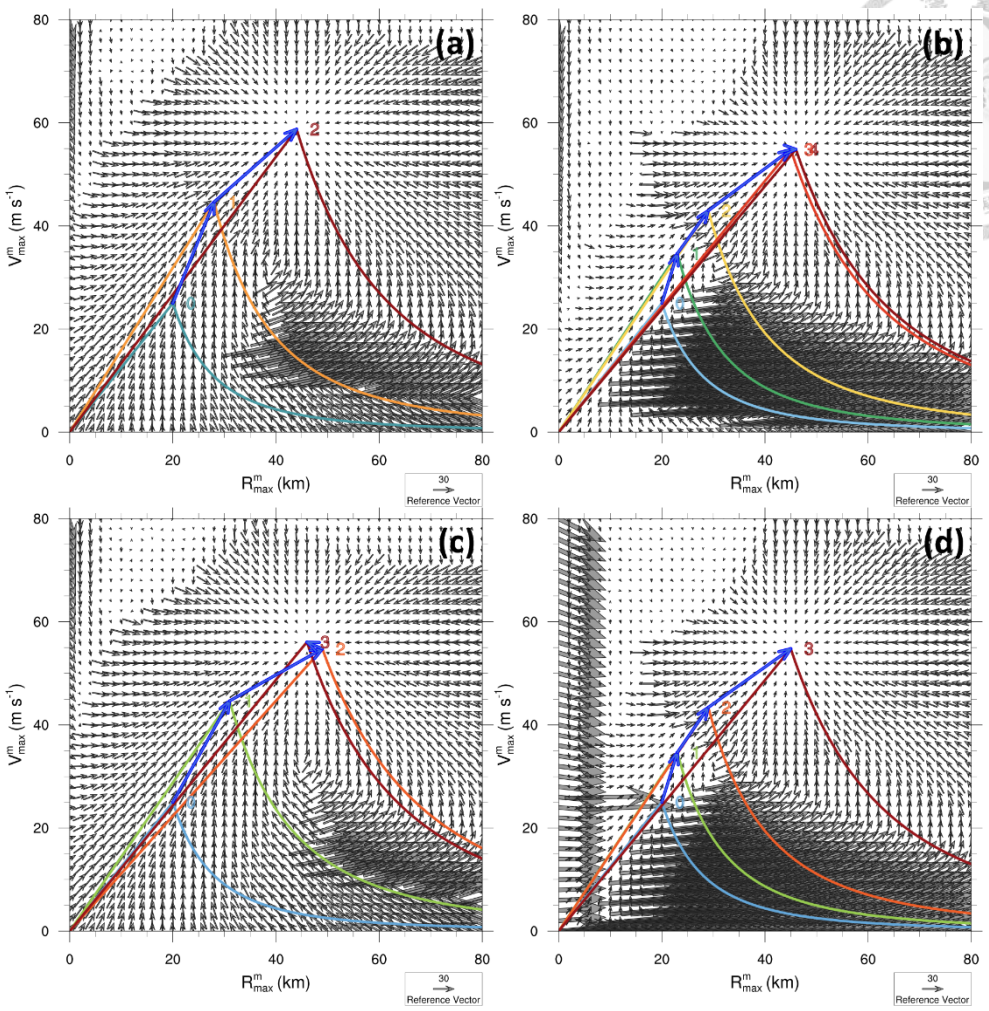

Figure 9. Same as in Figure 5 but for the centers at (a) (0,-142), (b) (8,-150), (c) (0,-158) and (d) (-8,-150).

2.2.4 Mitigation of the TC center displacement effects

To mitigate the effects of center displacement in the VDVD algorithm, as described in the previous subsection, the GBVTD-simplex (Lee and Marks 2000) center-finding algorithm is combined with the GBVTD-based unfolding algorithm. The GBVTD-simplex technique was proposed to determine the TC center from Doppler velocity, assuming the vortex center is where the local maximum of V_{max} is derived from the GBVTD algorithm. The simplex method, used to approximate the location of

doi:10.6342/NTU202403267

this local maximum, is combined with GBVTD to provide a proper vortex center in the GBVTD-simplex algorithm. Therefore, if the eye of the TC is not apparent, GBVTD-simplex can provide a more accurate center compared to the reflectivity-based algorithm (Chang et al. 2009a). Accordingly, the VDVD algorithm incorporates two loops to mitigate the effect of a shifted TC center. The inner loop (GBVTD iteration) aims to dealias the Doppler velocities, as discussed above. The outer loop (GBVTD-simplex iteration) is designed to determine the vortex center based on the Doppler velocity field obtained from the inner loop (Figure 2).

To examine the mutual influence between the outer and inner loops, the same symmetric V_T superimposed with 20% of V_T (V_{T1}) at 90°, V_R, and 5 m s^{-1} southerly V_M with an eastward 8-km displacement (20% of the simulated RMW) centered at the vortex center $(X^0, Y^0) = (8, -150)$ are applied. For the initial outer iterative loop, the inner loop converges within 3 iterations to a set of $(V_{max}^{0,3}, R_{max}^{0,3}) = (22.18\ m\ s^{-1}, 49\ km)$, which is substantially different from the structure of the analytic vortex due to the improperly dealiased velocity field (Figure 10a). Subsequently, a first apparent center $(X^1, Y^1) = (-9.25, -134.65)$ is determined from the GBVTD-simplex algorithm in the outer loop. With the new TC center, a set of $(V_{max}^{1,4}, R_{max}^{1,4}) = (48.54\ m\ s^{-1}, 44\ km)$ is calculated using the VDVD algorithm with a better dealiased Doppler velocity field (Figure 10b). The second apparent center

doi:10.6342/NTU202403267

determined from the GBVTD-simplex technique is $(X^2, Y^2) = (-2.12, -147.79)$, which is very close to the center location of the analytic vortex. Combined with the outer loop (GBVTD-simplex iteration), the Doppler velocities can be subsequently fully recovered in two iterations (Figure 10c), resulting in $(V_{max}^{2,4}, R_{max}^{2,4}) = (58.38\ m\ s^{-1}, 39\ km)$ from the inner loop.

A series of experiments are conducted to understand the improvements of the VDVD algorithm compared to the VDVD without the GBVTD-simplex technique, hereafter referred to as VDVD-inner (Table 6). The combinations of V_{T1} with 10% or 20% of V_T at 90° and V_M with 5 or 10 $\mathrm{m\,s^{-1}}$ from 180° are selected to induce the greatest asymmetry of a TC structure, along with an 8-km (20% of the simulated RMW) displacement of the TC center. The success rate is determined by the proportion of experiments that are completely dealiased. For the experiments with 10% V_T as V_{T1}, the success rate of the VDVD-inner is less than 75%. The VDVD algorithm provides a success rate 25 to 50% higher than that of the VDVD-inner, except in experiment B03, which has extreme conditions of 20% of V_T as V_{T1} and 10 $\mathrm{m\,s^{-1}}$ V_M. In these cases, the outer loop of the VDVD successfully approximates the vortex center to the true value. However, higher V_{T1} and V_M could increase uncertainties, resulting in a decreased success rate for the VDVD algorithm.

doi:10.6342/NTU202403267

Table 6. Sensitivity tests of the VDVD algorithm for various combinations of V_T, V_{T1}, V_R, and V_M and displacement of the TC center. A simplex center difference in italic format indicates that the test is not completely dealiased by the VDVD algorithm, and one in bold format indicates that the test is not completely dealiased by the VDVD without GBVTD simplex (VDVD-inner). The information in the second and third row of V_{T1} and V_M are the same as that in Table 3.

	V_{T1} (20%V_T) (90°)	V_{T1} (10%V_T) (90°)	V_R	V_M ($5\ m\ s^{-1}$) (180°)	V_M ($10\ m\ s^{-1}$) (180°)	Center Shift 8 km at (0°/90°/ 180°/270°)	Simplex Center Differences (km)	Success rate of VDVD	Success rate of VDVD-inner
B00		✓	✓	✓		✓	1.0/**1.1**/ 1.0/1.0	100%	75%
B01		✓	✓		✓	✓	2.4/**4.1**/ ***19.7***/1.9	75%	50%
B02	✓		✓	✓		✓	**3.3**/**3.1**/ 3.3/3.5	100%	50%
B03	✓		✓		✓	✓	***3.6***/***18.1***/ ***13.8***/***11.4***	0%	0%

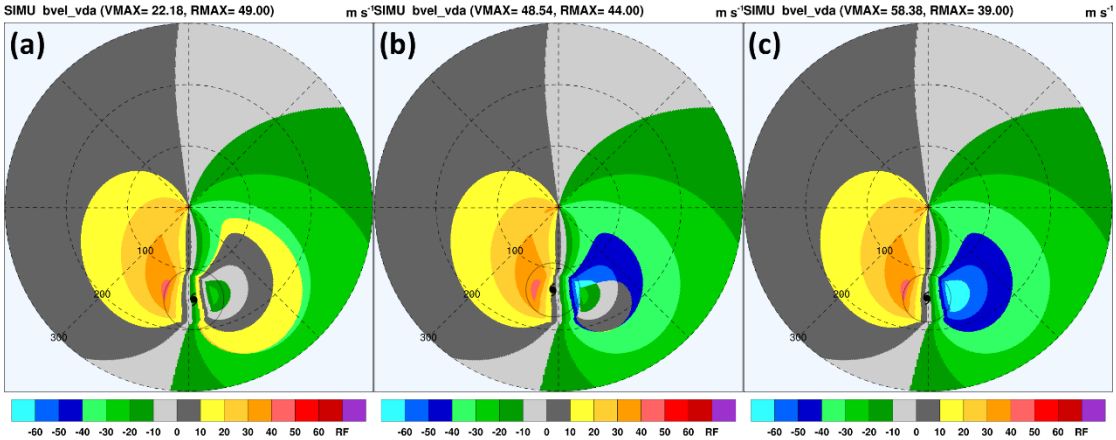

Figure 10. The dealiased Doppler velocity in the VDVD outer loop (a) 1st (b) 2nd (c) 3rd iteration used the condition that the superposition of axisymmetric V_T, 20% V_T as V_{T1} at 90°, V_R, and 5 m s^{-1} southerly V_M with eastward 8-km displacement (20% of simulated RMW).

doi:10.6342/NTU202403267

2.3. Results and Evaluations

Two typhoon cases, one with and one without landfall in Taiwan, were observed by the Wu-Fen-San radar (RCWF) and Hua-Lien radar (RCHL) to evaluate the success rates of the VDVD algorithm. The first case was Typhoon Fitow (2013), which passed over the ocean northeast of Taiwan with its center more than 100 km from the northern tip of Taiwan. The second case was Typhoon Nesat (2017), which followed a westerly track similar to that of Typhoon Fitow but made landfall in northeastern Taiwan. Since the strongest winds typically occur at lower altitudes in TCs (Marks and Houze 1987; Lee et al. 2000), radar PPI data from the first (0.5-degree) and second (1.4-degree) elevation angles were selected for the VDVD algorithm calculations. Additionally, a manually dealiased Doppler velocity dataset was used to verify the performance of the VDVD algorithm proposed in this study, as well as the 2D multipass velocity dealiasing algorithm (ZW06).

2.3.1 Typhoon Fitow (2013)

Figures 11-12 illustrate extreme examples of the ZW06 and VDVD algorithms for Typhoon Fitow (2013), as observed by the RCWF radar, respectively. The center of Typhoon Fitow was located over the ocean northeast of Taiwan at a distance of ~240 km from the radar site at 2311 UTC 5 Oct 2013. Typhoon Fitow exhibited a weakly circular-symmetric eyewall structure with a radius of ~50 km (Figure 11a).

doi:10.6342/NTU202403267

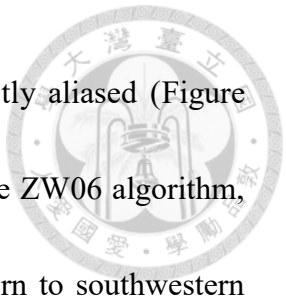

The raw Doppler velocities around the eyewall areas are mostly aliased (Figure 11b) because the wind speeds exceed the Nyquist velocity. Using the ZW06 algorithm, unreasonable Doppler velocities were observed near the northwestern to southwestern quadrants of the TC center, occasionally due to relatively noisy data around the eyewall regions (Figure 11c). This resulted in the lowest success rate of 74.5% compared to subjective dealiasing analysis (Figure 11e). In contrast, the VDVD algorithm achieved a success rate of more than 99% at that time (Figure 11d). Approximately 9.5 hours later, Typhoon Fitow moved to the ocean north of Taiwan, about 150 km from the radar site (Figure 12a). The reflectivity structure showed a more intense circular-symmetric eyewall compared to that at 2311 UTC 5 Oct (Figure 11a). Figure 12c displays the dealiasing result of Doppler velocity using the VDVD algorithm, showing an overly unfolded low-velocity region near the east side of the radar site due to sea clutter. Similarly, the ZW06 algorithm also exhibited the overly unfolded phenomenon in the same region (Figure 12b). Therefore, it is crucial to adequately remove sea clutter signals before applying the dealiasing algorithms to potentially improve the dealiased velocity performance.

To quantitatively evaluate the VDVD algorithm performance, comparisons are conducted with a subjective dealiasing analysis based on PPI pixels. Approximately 21.5% of the pixels were aliased in the Doppler velocity data over a 23-hour period

doi:10.6342/NTU202403267

(from 1907 UTC 5 Oct to 1757 UTC 6 Oct). On average, the VDVD and ZW06 algorithms successfully recovered 99.4% and 98.3% of the aliased velocity data, respectively. Table 7 presents the success rates from a total of 472 elevation sweeps. A total of 87% and 70% of the elevation sweeps exhibit success rates exceeding 99% for the VDVD and ZW06 algorithms, respectively. The statistical results indicate that the VDVD algorithm demonstrates more stable performance in providing high-quality data. Additionally, only approximately 2% of the elevation sweeps have a success rate under 97% for the VDVD algorithm, compared to 14% for the ZW06 algorithm.

As previously mentioned, the VDVD algorithm effectively dealiases Doppler velocity and concurrently provides an accurate center and inner core wind structure for TCs. Figure 13 illustrates the track of Typhoon Fitow derived from the GBVTD-simplex, which aligns well with the official track issued by the CWA. This indicates the potential usability of GBVTD-simplex track information for real-time operations. For the wind structure of Typhoon Fitow, Figure 14 presents the time series of V_{max} and R_{max} from the first elevation angle data derived from the VDVD algorithm. At 1907 UTC on Oct. 5, V_{max} and R_{max} were 40 m s^{-1} and 100 km, respectively. Sequentially, the V_{max} fluctuated slightly between 40-50 m s^{-1} before weakening to approximately 35 m s^{-1} around 1300 UTC on Oct 6. The R_{max} decreased from 100 km to 60 km between 0000 UTC on Oct. 5 and 0900 UTC on Oct. 6, with a

doi:10.6342/NTU202403267

further contraction from 90 km to 60 km occurring around 1100 UTC on Oct. 6. Generally, V_{max} and R_{max} are out of phase, consistent with previous studies on eyewall contraction (Marks and Houze 1987).

Table 7. Numbers of elevation sweeps falling between the criteria of raw data for VDVD and the algorithm in ZW06. The numbers in parentheses are the percentages of the 472 total sweeps.

Success rate%	**Raw data (%)**		**VDVD (%)**		**ZW06 (%)**	
99–100	1	(0.2)	411	(87.1)	333	(70.6)
98–99	7	(1.5)	40	(8.5)	43	(9.1)
97–98	10	(2.1)	11	(2.3)	28	(5.9)
< 97	454	(96.2)	10	(2.1)	68	(14.4)

doi:10.6342/NTU202403267

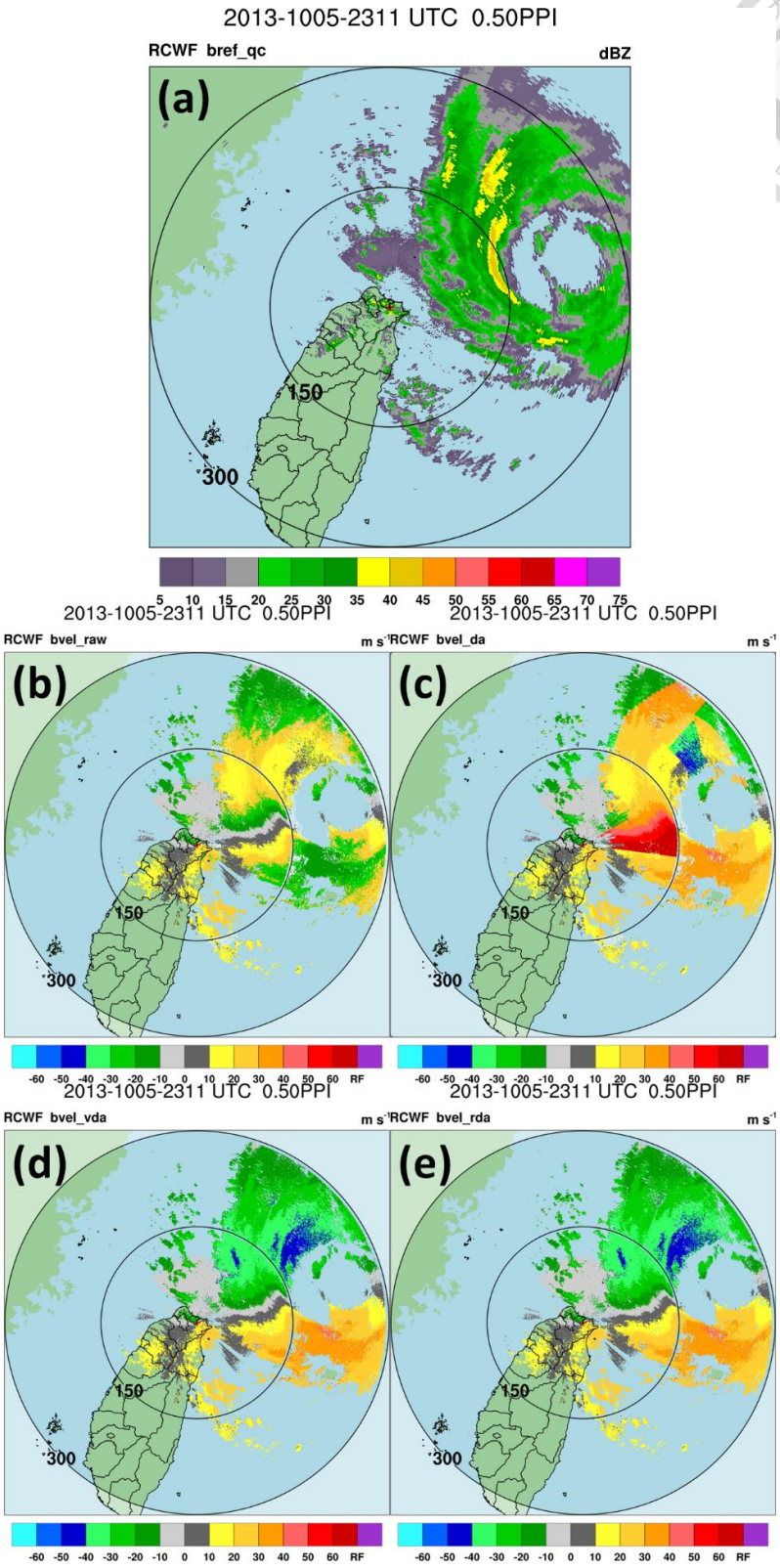

Figure 11. Radar observations of Typhoon Fitow (2013) at 0.5 degrees elevation from RCWF at 2311 UTC on October 5: (a) base reflectivity (dBZ), and Doppler velocities (m/s) of (b) raw data, (c) processed using the ZW06 algorithm, (d) processed using the VDVD algorithm, and (e) subjective analysis. Two range rings are indicated at 150 and 300 km from the radar site.

doi:10.6342/NTU202403267

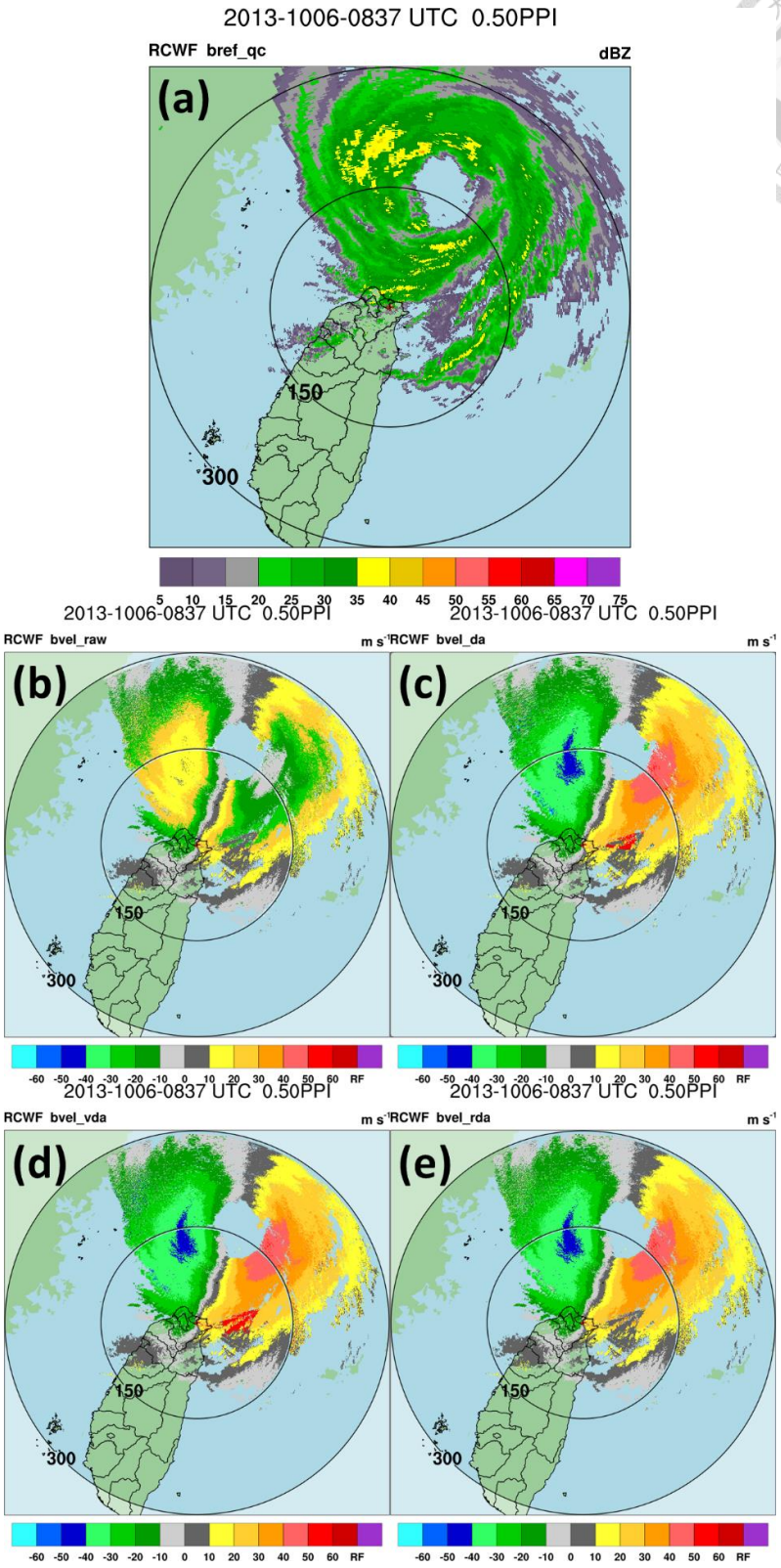

Figure 12. Same as Figure 11 except at 0837 UTC Oct. 6.

doi:10.6342/NTU202403267

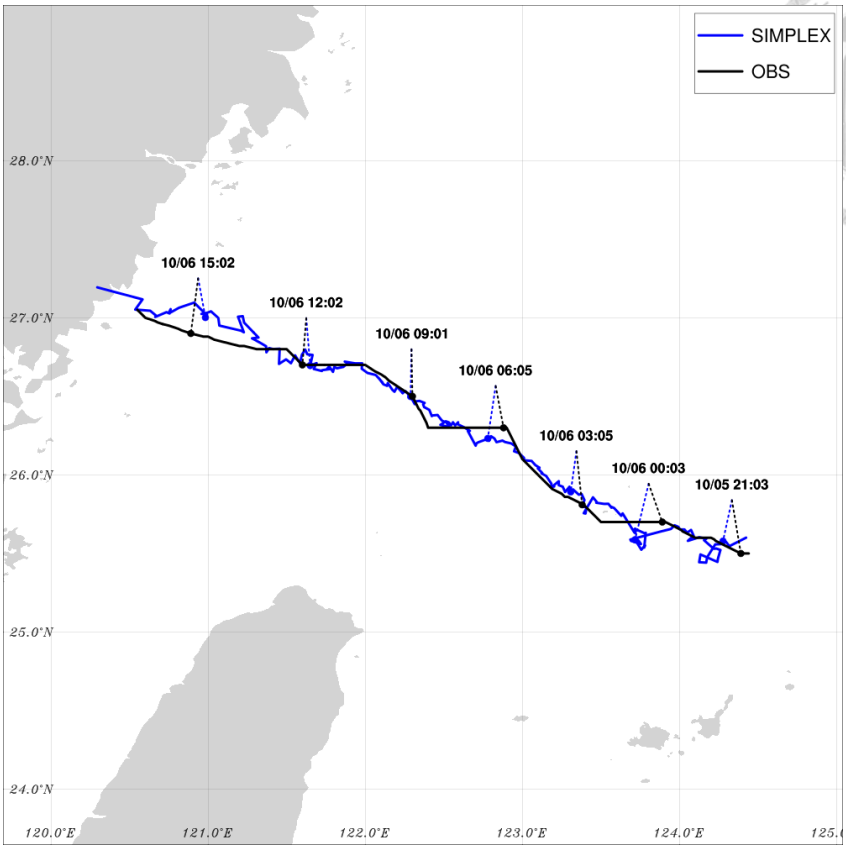

Figure 13. Track of Typhoon Fitow (2013) derived from GBVTD-simplex (blue line) and observations (black line). The numbers above the tracks are the dates and times in UTC.

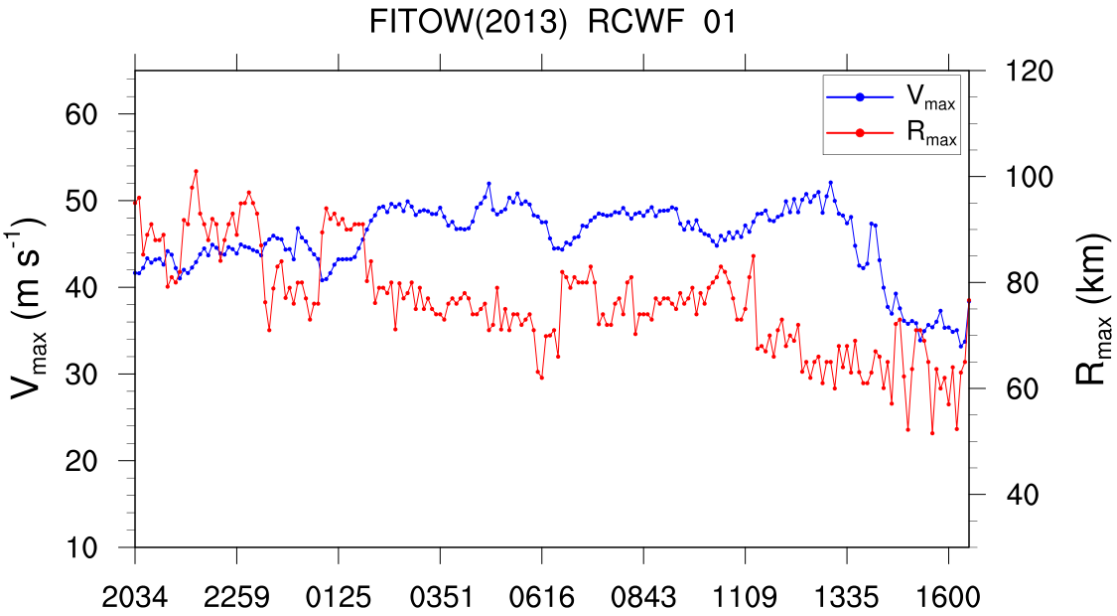

Figure 14. Time series of V_{max} (blue line) and R_{max} (red line) derived from the GBVTD-simplex technique with the first elevation data of RCWF.

doi:10.6342/NTU202403267

2.3.2 Typhoon Nesat (2017)

Figure 15a shows the reflectivity field of Typhoon Nesat observed from RCHL at 0622 UTC on July 29. An obvious asymmetric eyewall structure with strong reflectivity was located in the southern quadrant of the typhoon center. The center was approximately 130 km northeast of the radar site, and the eyewall radius was approximately 55 km. Notably, there are no valid data on the mountainside west of the RCHL because the electromagnetic wave emissions were turned off, as mentioned previously. A narrow beam blockage wedge to the northeast of the radar is the result of a tall building near the radar site. The aliased Doppler velocities from raw data occurred over the eyewall and surrounding area (Figure 15b.) Using the ZW06 algorithm, some aliased Doppler velocities are not adequately dealiased in the inbound region near the eyewall and its surrounding area (Figure 15c). In contrast, the VDVD algorithm successfully recovers these aliased Doppler velocities (Figure 15d).

When Typhoon Nesat moved toward the east coast of Taiwan, most of the aliased velocity data are recovered near eyewall regions (Figure 16a). However, there are some discontinuities in the Doppler velocities that are overly dealiased near the offshore regions of southeastern Taiwan. It results from the flow direction of terrain-induced local circulation that deviates from that of the Rankine combined vortex (e.g., Wu and Kuo 1999; Wu et al. 2002; Chang and Lin 2011). As a result, the Rankine combined

doi:10.6342/NTU202403267

vortex assumption of the VDVD algorithm cannot be adequately applied due to these local circulations. To address this issue and extend the applicability of the VDVD algorithm, a procedure of radial-by-radial verification, similar to the beam checking in ZW06, is used to correct the discontinuities resulting from inadequate unfolding. This concept is illustrated in Figure 17. Two radials passing through two tangential points of the RMW are chosen as initial references. The radial-by-radial verification procedure begins counterclockwise from the inbound side of the Doppler velocity and clockwise from the outbound side. This procedure is also applied to the regions inside the RMW with opposite directions to those outside the RMW. The procedure stops at the azimuth of the circulation center determined by the VDVD algorithm.

Figure 16b demonstrates the dealiased velocity field from the VDVD algorithm using the radial-by-radial verification procedure. The discontinuous regions are significantly reduced, indicating that this verification procedure can recover inadequately dealiased Doppler velocities, particularly when local circulations outside the TC inner core regions deviate from the Rankine combined profile assumption.

doi:10.6342/NTU202403267

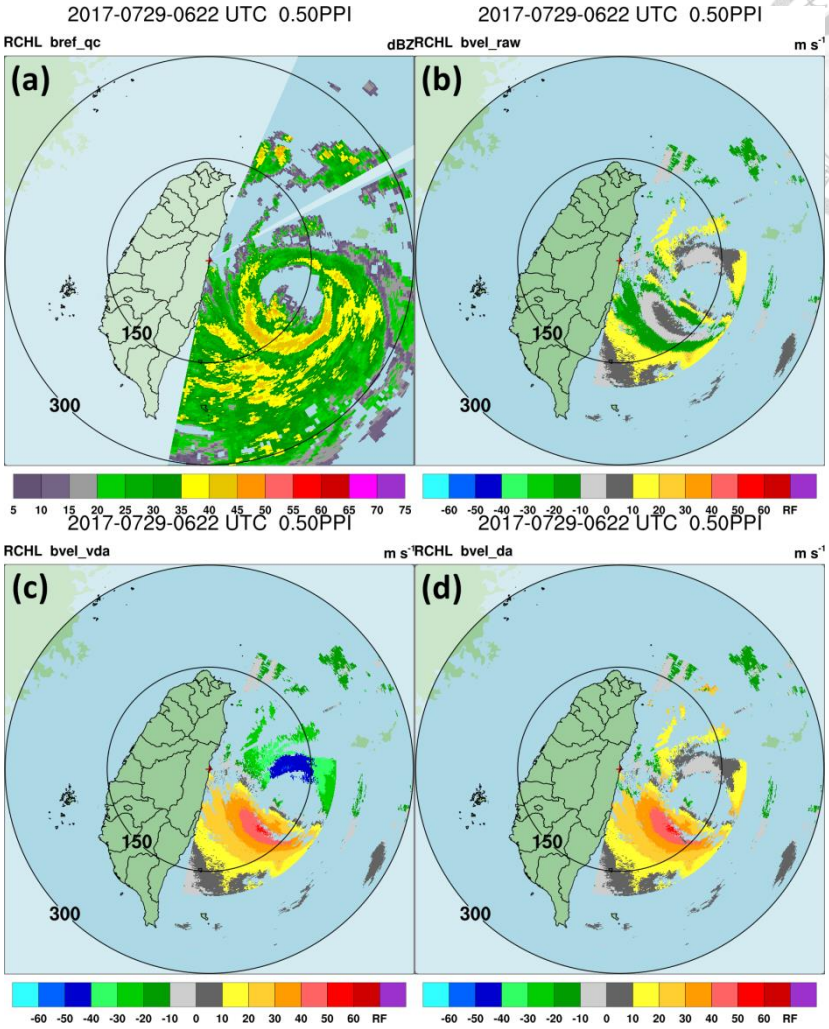

Figure 15. Radar observations of Typhoon Nesat (2017) at 0.5 degrees from RCHL at 0622 UTC on July 29: (a) base reflectivity (dBZ), and Doppler velocities (m/s) of (b) raw data, (c) processed using the ZW06 algorithm, (d) processed using the VDVD algorithm. Two range rings are indicated at 150 and 300 km from the radar site.

doi:10.6342/NTU202403267

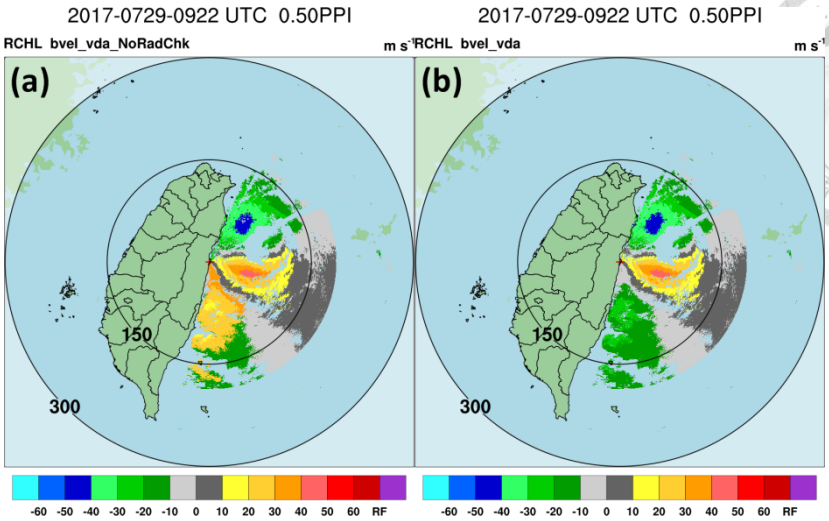

Figure 16. Radar observations of Typhoon Nesat (2017) at 0.5 degrees from RCHL at 0922 UTC on July 29: (a) processed using the VDVD algorithm and (b) processed using the VDVD algorithm with radial verification procedure. Two range rings are indicated at 150 and 300 km from the radar site.

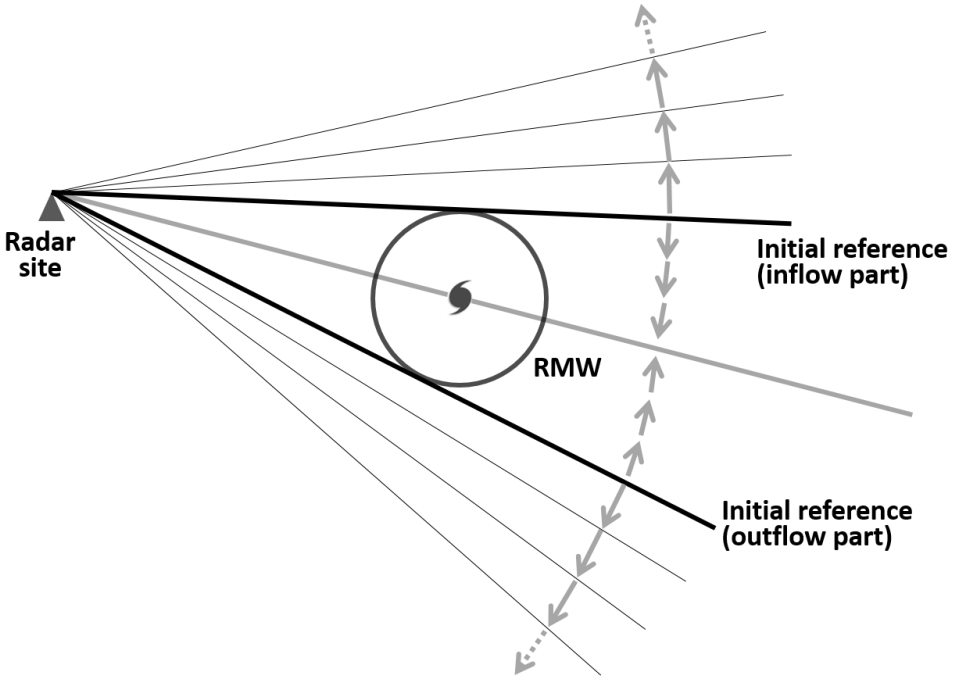

Figure 17. Schematic diagram of radial-by-radial verification procedure. The black circle indicates the maximum wind radius centered on the typhoon symbol. The thick black lines denote the initial references from the inflow and outflow parts. The gray arrows represent the beam verification in the clockwise and anticlockwise directions.

doi:10.6342/NTU202403267

2.4. Discussion

Several sensitivity tests and two typhoon cases are examined to evaluate the VDVD algorithm proposed in this study. The VDVD algorithm, based on the vortex dealiasing concept, demonstrates the capability to provide high-quality Doppler velocity. The uncertainties caused by factors such as TC asymmetry, center displacement, and data quality that could potentially degrade the results of the VDVD algorithm were also found. As demonstrated in the sensitivity tests in Section 2.2.2, the uncertainties of the VDVD algorithm increase when large V_{T1} or V_M are superimposed on an axisymmetric vortex. This issue is related to the inherent limitations of the GBVTD algorithm, as discussed by Lee et al. (1999). However, a deviated Rankine combined vortex wind structure retrieved from GBVTD can still be used as a reference vortex as long as the difference between the reference and observed Doppler velocities is less than 1.5 times the Nyquist velocity.

The uncertainty of the VDVD algorithm generally increases with the center displacement of the axisymmetric vortex as discussed in Section 2.2.3. In such conditions, the magnitude of the GBVTD-retrieved maximum axisymmetric tangential wind decreases and the RMW increases slightly (Lee and Marks 2000). To mitigate the effect of center displacement in the VDVD algorithm, the GBVTD-simplex center-finding algorithm can be applied to reduce the uncertainty of the vortex center. In

doi:10.6342/NTU202403267

practice, the radial gradient of the mean tangential wind is relatively flat in most weak TCs, making it difficult for the simplex algorithm to find the exact maximum, as addressed by Lee and Marks (2000). To further improve the accuracy and consistency of TC center estimates, the objective statistical center-finding GBVTD-simplex method can be enhanced by applying the spatial and temporal continuities of RMW, V_{max}, and TC center (Bell and Lee 2012). Additionally, the official best track analysis can provide typhoon centers to ensure accuracy and serve as a reference for the VDVD algorithm.

Radar data quality is also an important factor affecting the results of the VDVD algorithm. As described above, Taiwan is a mountainous island surrounded by the ocean, leading to significant challenges in radar observations due to sea clutter, ground clutter, and beam blockage. From the evaluation of Typhoon Fitow (2013) in Section 2.3, it is evident that unsuccessful pixels, primarily resulting from the influence of sea clutter, are often embedded with weather echoes, thereby reducing the success rate of the VDVD algorithm. Additionally, ground clutter can significantly affect the velocity dealiasing results, particularly when TCs are near the coastline or making landfall. Consequently, nonweather echoes should be adequately removed (Chang et al. 2009b; Lakshmanan et al. 2007; Liu and Chandrasekar 2000; Berenguer et al. 2007) in advance to ensure the quality of the data used in the VDVD algorithm.

doi:10.6342/NTU202403267

3. Rapid Intensification of Typhoon Chanthu (2021)

3.1. Data and method

As Typhoon Chanthu moved semiparallel to the eastern coast of Taiwan, the dramatic intensity change was observed not only by the RCKT, RCGI, RCHL, and RCWF radars but also by the ISHI radar of Japan. The specifications of the 5 radars are listed in Table 2. The data observed by the above 5 radars show that Chanthu's eyewall was well organized with a clear eye during its passage near Taiwan (Figure 1). The ground-based velocity tracking display algorithm (GBVTD; Lee et al. 1999) is a single-radar wind retrieved technique that can estimate various aspects of the primary circulation of a TC, including the axisymmetric tangential and radial winds, and asymmetric tangential winds. However, the accuracy of the retrieved TC circulation using the GBVTD is highly dependent on the precise determination of the center position, as the calculations are based on a ring with a fixed radius from the center of the TC. Chang et al. (2009a) introduced the TCET (Tropical Cyclone Eye Tracking) algorithm, which was developed to objectively detect and track the eye and center of a TC using radar reflectivity data. The results demonstrate that it can enhance the quality of the GBVTD-retrieved circulation for TC with well-organized eyewall structures when compared to the utilization of the TC center derived from the GBVTD-simplex algorithm (Lee and Marks 2000). Therefore, the TCET algorithm was utilized to estimate the TC

doi:10.6342/NTU202403267

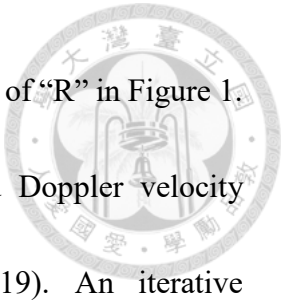

center from five radars, for which the abbreviations have a superscript of "R" in Figure 1. The aliased Doppler velocity was recovered by the vortex-based Doppler velocity dealiasing (VDVD) algorithm described in Chang et al. (2019). An iterative surface-fitting dealiasing algorithm, which is an enhanced version of the two-step QC procedure described in Chang et al. (2020), was also applied for local dealiasing and noise filtering (interested reader can find the introduction in the appendix). Then, the GBVTD algorithm was used for single-Doppler radar retrieval with the data from four radars, for which the abbreviations have a superscript of "V" in Figure 1. Both radar reflectivity and Doppler velocity data are interpolated to achieve a spatial resolution of 1 km by 1 degree, centered on the TCET centers. The temporal resolutions are 6–8 minutes, as determined based on the volume scan times of multiple radars. Furthermore, the dense radar network provides the opportunity for dual-Doppler synthetic analysis (Ray et al. 1975; Shapiro et al. 2009; Liou and Chang 2009), offering valuable information for the analysis and evaluation of the accuracy of single-Doppler wind retrievals. The composite dual-Doppler synthetic wind (DDW) data result from six sets of dual-Doppler analyses (Chang et al. 2019), incorporating data from RCKT, RCGI, RCHL, and RCWF radars. This dataset features a high spatial resolution of 1 km in both horizontal and vertical dimensions, along with a temporal resolution of 10 minutes.

The azimuthal gaps in the radar data and the gap-filling process may influence both

doi:10.6342/NTU202403267

the magnitude and phase of the Fourier decomposition. To primarily extract the characteristics of wavenumber-0 axisymmetric tangential wind, a gap size of 180 degrees is considered acceptable (Lorsolo and Aksoy 2012; Cha and Bell 2021). Consequently, the GBVTD technique is applied to retrieve the mean tangential wind when the azimuthal coverage of the available data exceeds 50%. In cases where there are gaps in the Doppler velocity data, linear interpolation is used to fill the azimuthal gaps, allowing for the utilization of fast Fourier transform (FFT) (Heideman et al. 1985) decomposition in the GBVTD algorithm. For the azimuthal average of reflectivity data, the same 50% azimuthal coverage criterion is applied, but no attempts are made to fill any data gaps. The temporal coverage of the GBVTD retrieval from each radar is limited to a specific portion of the overall analyzed period. To capture a comprehensive temporal evolution of the wind structure within the inner core of the TC (within a 60 km radius from the TCET centers) from these four radars, the GBVTD-retrieved winds from each radar were composited within 10-minute intervals using the inverse distance weighting.

In addition to the retrieval of the main circulation of Chanthu, the VWS of the embedded TC is also an essential information corresponding to its convection asymmetry. However, an accurate estimate of the mean flow of a TC is not straightforward to obtain in real time, especially when the terrain is nearby and terrain-induced flow is enhanced. While the DDWs were indeed conducted for the analysis of Typhoon Chanthu, which can

doi:10.6342/NTU202403267

provide more accurate wind information compared to the single radar retrieval method, there are certain limitations to be considered. Specifically, the winds near the baseline between two radars cannot be directly retrieved using the DDW. During the major intensification stage of Typhoon Chanthu, which occurred from 1600 to 2100 UTC on Sep 11, the storm happened to be located near the baseline between the RCGI and RCHL radars. As a result, the DDW data was unavailable for the western to northwestern sides of the typhoon (Figure 18b). To ensure comprehensive analysis and maintain continuity in the dataset, the GBVTD method was employed for wind retrieval during this specific period. Moreover, the horizontally uneven distribution of the DDW makes the calculation of mean flow difficult. The directions of the mean flow derived from the DDW dataset were found to be unstable over time and did not consistently align with the observed eyewall asymmetry.

In order to address this limitation and obtain a more reliable estimate of the mean flow, the author conducted a further application of the GBVTD method. This involved utilizing two adjacent radars capable of simultaneously observing the Doppler velocity within the inner core of the typhoon. The detailed methodology for this approach is documented in the Appendix of Murillo et al. (2011). They argued that the unresolved cross-beam mean flow is one of the sources of error when estimating the mean tangential wind using the GBVTD. Building upon this concept, the author extended and applied this

doi:10.6342/NTU202403267

method in the present study for the estimation of the mean flow of a TC. This allowed for a more comprehensive examination of the mean flow, which could be further correlated with the observed TC eyewall asymmetry. Area-average V_M (the magnitude of mean flow) and θ_M (the direction of mean flow) with different radii criteria of rings (0–60, 10–60, 20–60, and 30–60 km) were first evaluated. The results showed a significant fluctuation of the mean flow time series if the strong wind data near the RMW (radius of maximum wind) were included (e.g., 0–60, 10–60, 20–60 km) for calculation. Therefore, V_M and θ_M averaged within 30–60 km radii (2 to 4 times of the RMW) were utilized for improved data interpretability. Note that the mean tangential winds presented in this study were corrected by the GBVTD-derived mean flow according to the Eq. (20) in Lee et al. (1999). The other mean flow utilized in this study, derived from ECMWF ERA5 reanalysis data, was the mean wind within a 500-km radius from the TC center (Reasor and Eastin 2012). The VWS is commonly determined by calculating the vector difference of the mean flow between 200 and 850 hPa. However, due to reduced radar data density at higher elevations, the calculation of radar-derived mean flow is not feasible above 8 km. To facilitate a more comprehensive and comparable analysis between radar data and ERA5 data, the selected layers of the ERA5 dataset are at 800, 700, 600, 550, 450, 400, and 350 hPa, which closely correspond to the altitude of 2, 3, 4, 5, 6, 7, and 8 km, respectively. As a result, the VWS derived from GBVTD was computed by taking the

doi:10.6342/NTU202403267

vector difference of the mean flow between 8 and 2 km, corresponding to the pressure levels of 350 and 800 hPa, along with the ERA5-derived VWS.

It is important to note that the mean flows analyzed in section 3.4 contain the information of typhoon motion speeds and are exclusively used for the calculation of the deep-layer mean (DLM). However, for the subsequent analysis discussed in section 3.5, the mean flows were adjusted by subtracting the motion speeds to specifically focus on the discussion of the relative direction between the VWS and the LMF. To evaluate the agreement between the TC motion and the DLM derived from these mean flows, the author utilizes the DLM definition provided by Velden and Leslie (1991) and Hu and Zou (2021). The original formula is as follows:

$$DLM = \frac{75\vec{V}_{300}+100\vec{V}_{400}+150\vec{V}_{500}+175\vec{V}_{600}+175\vec{V}_{700}+150\vec{V}_{850}}{825} \quad (7)$$

where $\vec{V}_{300}$, $\vec{V}_{400}$, $\vec{V}_{500}$, $\vec{V}_{600}$, $\vec{V}_{700}$ and $\vec{V}_{850}$ indicate the wind vector at 300, 400, 500, 600, 700 and 850 hPa, respectively. As discussed above, the author has adjusted the vertical layers in the ERA5 data to 800, 700, 600, 550, 450, 400, and 350 hPa to align more closely with the 2 to 8 km vertical range, where the radar data provide more comprehensive coverage. Accordingly, the above formula has been modified to:

$$DLM_{ERA5} = \frac{75\vec{V}_{350}+100\vec{V}_{400}+150\vec{V}_{550}+175\vec{V}_{600}+175\vec{V}_{700}+150\vec{V}_{800}}{825} \quad (8)$$

The corresponding formula for radar-derived DLM is:

$$DLM_{GBVTD} = \frac{75\vec{V}_{8km}+100\vec{V}_{7km}+150\vec{V}_{5km}+175\vec{V}_{4km}+175\vec{V}_{3km}+150\vec{V}_{2km}}{825} \quad (9)$$

doi:10.6342/NTU202403267

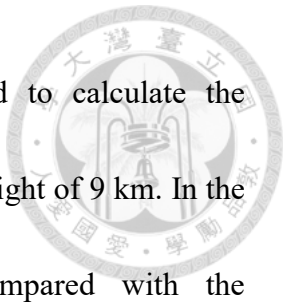

Six layers of mean flow from 2 km to 8 km were used to calculate the GBVTD-derived DLM because of insufficient data samples at the height of 9 km. In the following sections, the GBVTD-derived mean flow was compared with the ERA5-derived mean flow and was used to interpret the connection between the movement and convection asymmetry of TY Chanthu.

3.2. Overall structure

Figure 1 shows the TCET track with a 10-min interval from the radars, for which the abbreviations have an upper index of "R". A northwestward track with a speed of approximately less than 3 m s^{-1} before 0600 UTC Sep 11 was found when Typhoon Chanthu moved into the Bashi Strait. Afterward, Chanthu slowed, recurved to a northeastward motion, and started to accelerate to ~6 m s^{-1}. Chanthu moved northward with a similar speed as it moved into the eastern offshore region of Taiwan. Later, it accelerated after 0000 UTC on Sep 12 and exhibited a north–northwestward motion when it was close to the northeastern tip of Taiwan. After 0400 UTC on Sep 12, the track turned back to northeastward motion and slowed to a speed of approximately 5 m s^{-1} in the northeastern offshore area of Taiwan as it moved to the East China Sea.

Figure 18 shows the composite dual-Doppler wind retrievals every 6 hours from 1000 UTC Sep 11 to 0400 UTC Sep 12. Very intense cyclonic structures were found as the typhoon moved northward from the southeastern to the northeastern offshore area of

doi:10.6342/NTU202403267

Taiwan. The significant eyewall circulation had a maximum wind speed of more than 50 m s^{-1} and an RMW of approximately 15–20 km at altitudes of 3–4 km. The wind speeds were rapidly reduced to 20–25 m s^{-1} at a radius of 50 km from the circulation center. This strong radial gradient of tangential wind indicates that Chanthu was a compact TC. In the outer rainband regions over the northern part of Chanthu, the winds were characterized by southeasterly winds with wind speeds of approximately 15 to 20 m s^{-1} (Figure 18a).

As the typhoon moved northward, the wind speeds increased, with a maximum wind speed of more than 60 m s^{-1} within the inner core (Figure 18b). At 2200 UTC Sep 11, the wind speeds were further enhanced, with a maximum wind speed of more than 65 m s^{-1} in the eastern quadrant (Figure 18c). In addition, the presence of echo-free areas was consistently observed in the southeastern offshore region of Taiwan. This phenomenon, which has been observed in numerous typhoon cases, including Haitang (2005), Talim (2005), Matsa (2005), and Krosa (2007), has been hypothesized to be associated with the adiabatic warming of downslope flow induced by the eastward wind component originating from the southern quadrant of the typhoon circulation across the CMR (Chen et al. 2010; Hsu et al. 2018). At 0400 UTC Sep 12, the typhoon intensity gradually weakened with a maximum wind speed of approximately 55 m s^{-1} as it approached the northeastern tip of Taiwan (Figure 18d). The echo-free areas exhibited a consistent spatial position, but their size notably expanded.

doi:10.6342/NTU202403267

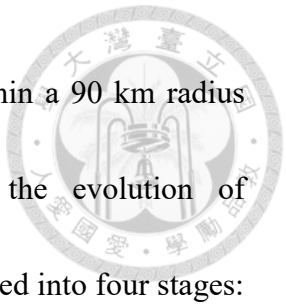

Figure 19 illustrates the temporal evolution of reflectivity within a 90 km radius from the TCET center of Typhoon Chanthu. According to the evolution of GBVTD-retrieved V_{max} and RMW, the analyzed period can be divided into four stages: the first (or minor) intensification, second (or major) intensification, peak, and weakening stages (Figure 20). During stages I and III, the eyewall convection prominently displayed wavenumber-1 azimuthal asymmetry. In stage I, the maximum asymmetry was observed in the eastern sector (Figures 19a, b). By the end of Stage I, the asymmetry had decreased moderately, resulting in a more axisymmetric eyewall (Figure 19c). At 1600 UTC, the wavenumber-0 signal became most pronounced (Figure 19d). However, this axisymmetric structure persisted for only approximately 2 hours before the wavenumber-1 signal regained dominance, albeit with a shift in the maximum from the eastern to northeastern sector (Figures 19e, f). Subsequently, the area of high reflectivity above 45 dBZ extended beyond the northeast sector, encompassing the downstream sector on the northwestern side (Figures 19g-i).

The comparison between ERA5-derived and radar-derived VWS revealed discrepancies after 1200 UTC. Prior to 1200 UTC, the eyewall asymmetry correlated well with both VWS datasets (Figures 19a, b). Between 1400 and 1600 UTC, the eyewall displayed an increased axisymmetric structure, aligning with the weak VWS obtained from radar (Figures 19c, d). After 1600 UTC, the VWS intensified and shifted from

doi:10.6342/NTU202403267

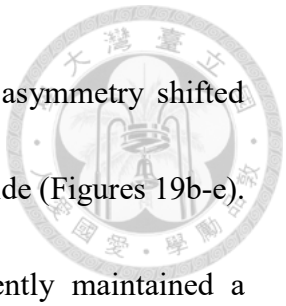

northerly to northwesterly. Simultaneously, the maximum eyewall asymmetry shifted from the eastern sector to the northeastern sector, located on the DL side (Figures 19b-e). However, it is noteworthy that the ERA5-derived VWS consistently maintained a northerly direction throughout stages I to III, which contrasts with the observed eyewall asymmetry.

doi:10.6342/NTU202403267

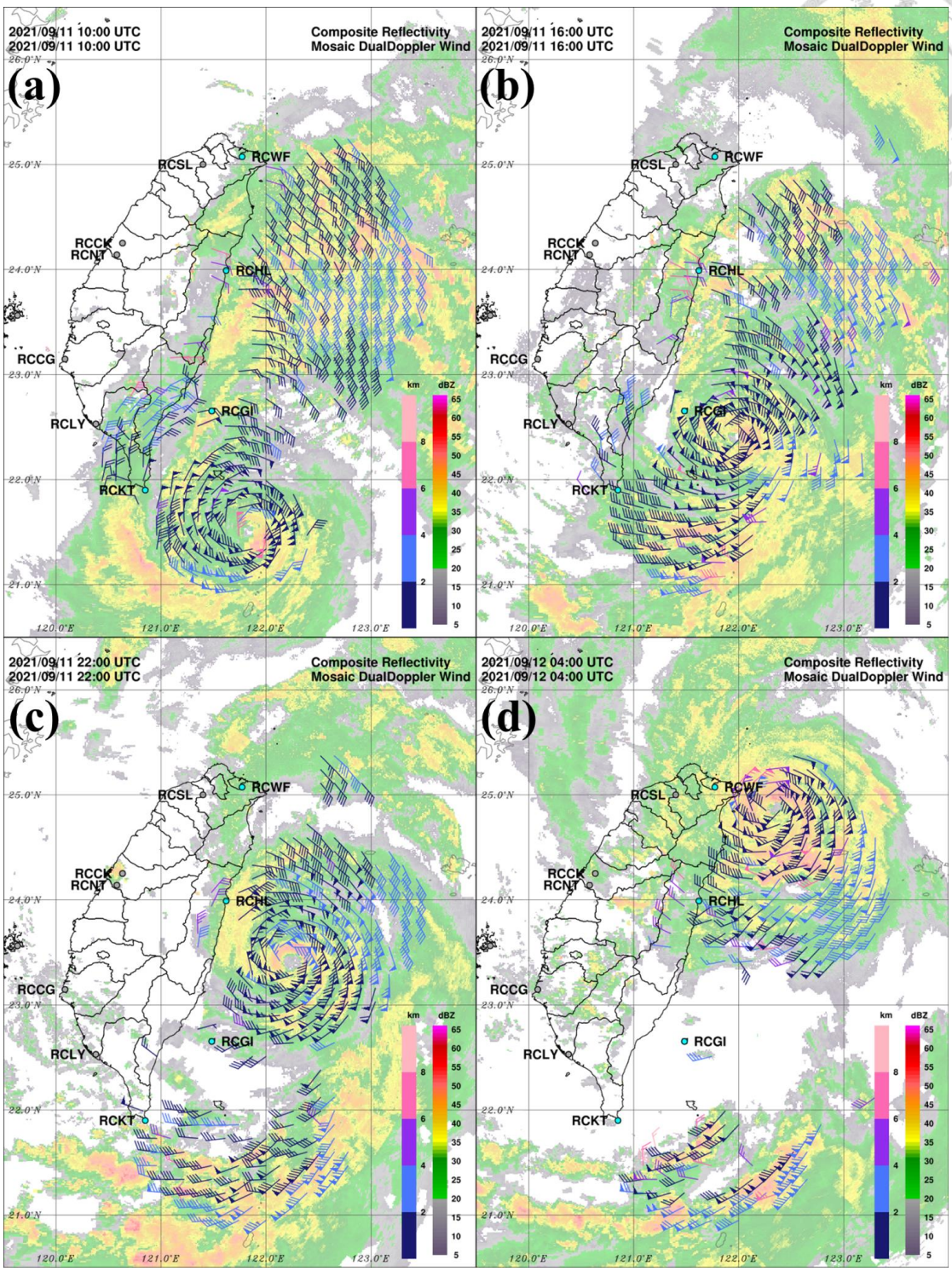

Figure 18. The lowest available DDW at (a) 1000 UTC on Sep 11, (b) 1600 UTC on Sep 11, (c) 2200 UTC on Sep 11, and (d) 0400 UTC on Sep 12, 2021. The wind barbs, depicted in dark blue, blue, purple, red–pink, and pink, represent wind retrievals from altitudes of 0–2 km, 2–4 km, 4–6 km, 6–8 km, and above 8 km, respectively. The color shading corresponds to the composite reflectivity.

doi:10.6342/NTU202403267

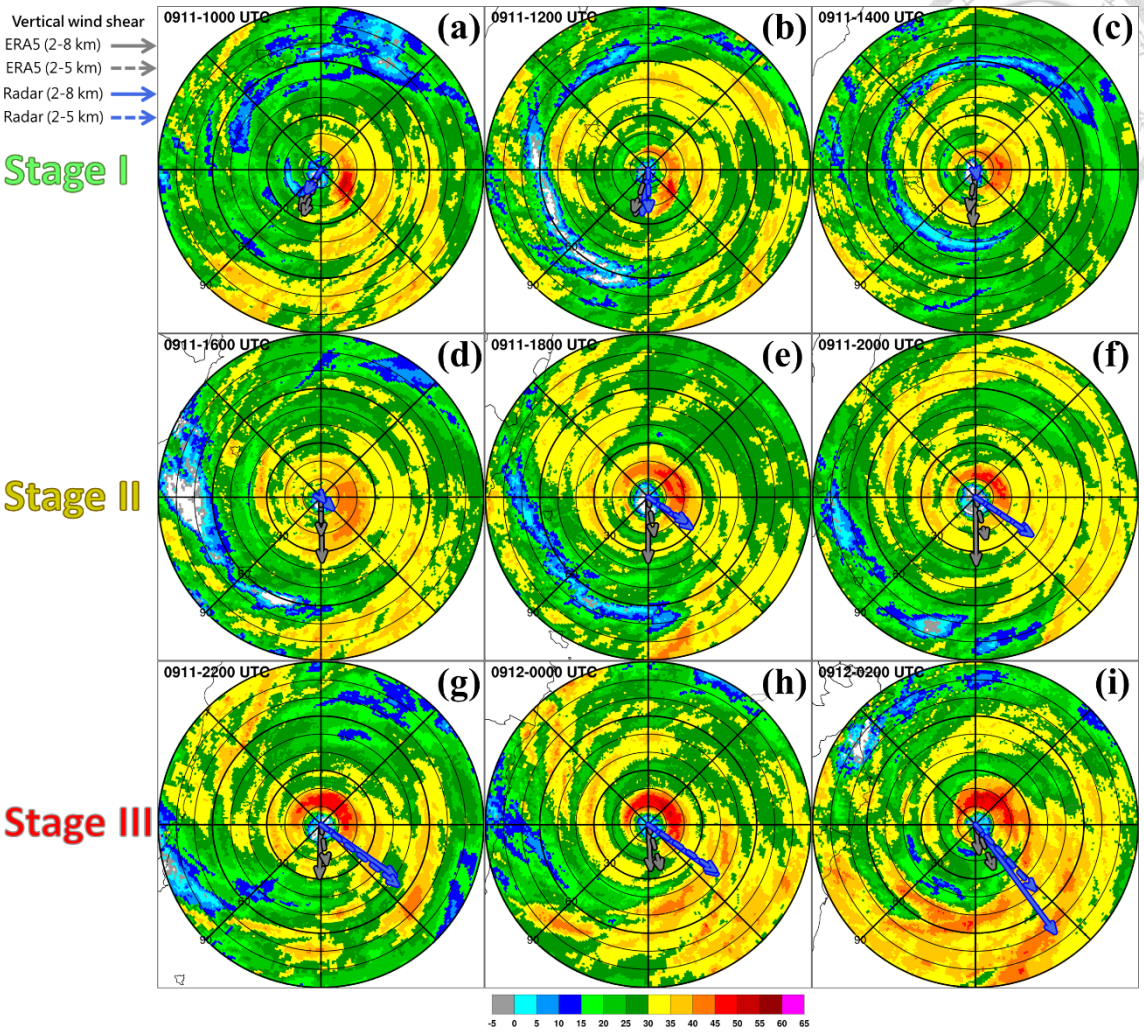

Figure 19. Reflectivity snapshot at 3-km altitude centered on the TCET centers at (a) 1000, (b) 1200, (c) 1400 (stage I; first row), (d) 1600, (e) 1800, (f) 2000 (stage II; second row), (g) 2200 Sep 11, (h) 0000, and (i) 0200 Sep 12 (stage III; third row). The blue arrows indicate GBVTD-derived VWS, while the gray arrows represent ERA5-derived VWS. Solid arrows denote VWS between 2 and 8 km, and dashed arrows correspond to VWS between 2 and 5 km. The interval between the thick circles is 30 km, and between the thin circles is 10 km. The interval between thin circles also represents 3 m s^{-1} for VWS.

The previous paragraphs provide a general and qualitative review of the kinetic and convective features of Typhoon Chanthu. Quantitative information on the V_{max} and RMW of Chanthu derived from the GBVTD at 3-km altitude is described in the following (Figure 20). During the first intensification stage (denoted by stage I), the V_{max} had a

doi:10.6342/NTU202403267

minor increase from ~48 m s^{-1} to 52 m s^{-1} accompanied by a significant RMW contraction from 20 km to 12 km (e.g., reduced 40%) from 1000 UTC to 1600 UTC on Sep 11. At approximately 1600 UTC, the RMW dramatically expanded from 12 km to 20 km, however, V_{max} remained at ~50 m s^{-1}. After the stage I, the RMW started to contract again from 20 to 12 km between 1600 UTC and 2100 UTC on Sep 11 which was defined as the major intensification stage (denoted by stage II) in this study. The V_{max} significantly increased from ~50 m s^{-1} to ~64 m s^{-1} in only five hours during this stage. Later, Chanthu evolved into the most intense stage and remained at a V_{max} of 58–62 m s^{-1} in the following five hours (denoted by stage III). Finally, Chanthu weakened quickly after 0200 UTC with an average rate of ~2.4 m s^{-1} h^{-1} in the last 8 hours of the analysis time (denoted by stage IV). The V_{max} and RMW evolution derived from GBVTD is consistent with that of DDW, indicating that GBVTD is a robust algorithm for retrieving TC winds, as documented by Cha and Bell (2021).

Overall, the 3-km-altitude GBVTD-retrieved V_{max} increased by ~18 m s^{-1} in 11 hours (1000 UTC to 0200 UTC Sep 11). The intensification rate can be considered RI, which is commonly defined as the maximum surface wind intensifying by more than 20 kt (10.3 m s^{-1}) in 12 hours (Kaplan et al. 2015). Although the definition of RI is based on surface wind change, Franklin et al. (2003) found that the ratio of wind speed from the eyewall surface to 700 hPa is approximately 0.9. Therefore, the change in wind speed at 3

doi:10.6342/NTU202403267

km should generally reflect the increasing rate near the surface. In the weakening stage, the 3-km altitude V_{max} decreased significantly by 19 m s^{-1} in 8 h, which is also considered rapid weakening (RW), defined as the TC intensity decreasing by 20 kt (10.3 m s^{-1}) or more in 24 h (DeMaria et al. 2012). The decrease in intensity of Chanthu reached 10.3 m s^{-1} only during an ~3 h period from 0200 UTC to 0500 UTC and sequentially weakened to the end of the analysis period. Notably, Chanthu experienced both RI and RW within 24 hours. Such a dramatic change in intensity is a serious challenge for operation centers to issue and forecast the intensity of the TC. The possible factors that caused the intensification and weakening of Typhoon Chanthu will be further discussed in the following section.

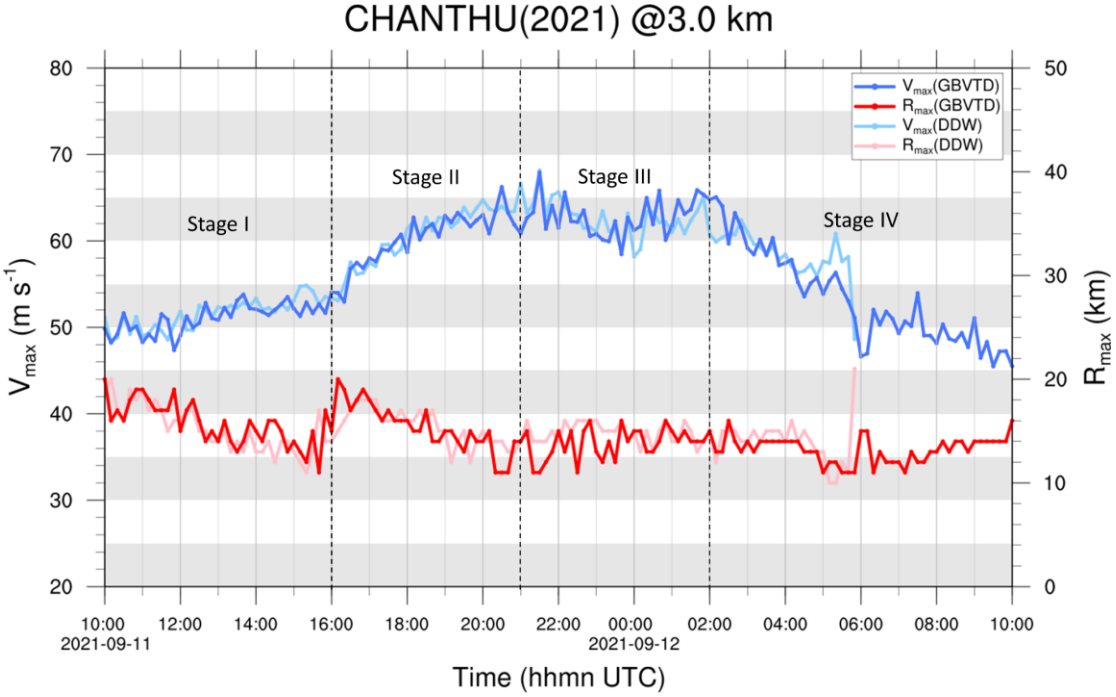

Figure 20. Temporal evolutions of the V_{max} (blue line) and RMW (R_{max}, red line) of Typhoon Chanthu at 3 km altitude. The V_{max} and RMW derived from dual-Doppler synthetic winds are indicated in light blue and light red, respectively.

doi:10.6342/NTU202403267

3.3. Evolution of the inner core structure

The Hovmöller diagram of axisymmetric tangential winds reveals that Chanthu retained its compact wind structure over the whole analysis period (Figure 21a). Typhoon Chanthu not only had an extremely small eyewall radius compared with the climatology value of 54.7 km in the western Pacific (Knapp et al. 2018), but also had an extremely strong near-core (RMW to 3×RMW) radial gradient of tangential wind of 0.8–0.9 m s^{-1} km^{-1} compared with that of TCs in the same intensity category (Vinour et al. 2021).

Due to the RMW dramatically expanding from 12 km to 20 km at approximately 1600 UTC on Sep 11 (Figure 20), it is suggested that Chanthu was experiencing an eyewall replacement cycle (ERC). However, the tangential wind did not present an apparent secondary eyewall formation (SEF) at 3 km altitude during the first intensifying stage (Figure 21a), and V_{max} remained at a value of ~50 m s^{-1}. To highlight the presence of the double wind peak associated with the ERC, Hovmoller diagrams of tangential wind were constructed at elevations ranging from 2 to 7 km, with contour intervals of 1 m s^{-1} (Figure 22). Analysis of the Hovmoller diagrams at 2 to 4 km revealed that the RMW was predominantly situated between 12 and 15 km. Notably, a significant jump in the RMW occurred at approximately 1600 UTC; however, a clear double wind peak pattern was not found. In contrast, at higher elevations of 5 to 7 km, a progressive increase in wind speed was observed within the radius range of 20 to 30 km, starting from 1400 UTC and

doi:10.6342/NTU202403267

extending radially until 1430 UTC. Over the subsequent 2.5 hours, this secondary wind maximum ceased its radial extension, and the radius of this secondary wind maximum exhibited a slight contraction. The presence of a distinct double wind peak pattern was most pronounced at 1600 UTC. Following this time, the primary eyewall dissipated, and the secondary eyewall underwent a gradual contraction. Based on these findings, it is proposed that Typhoon Chanthu underwent an ERC between 1400 and 1700 UTC. Notably, the primary and secondary eyewalls of Chanthu were separated by a mere 10 km. The observed ERC in this case, characterized by the merging of the secondary eyewall with the primary eyewall rather than complete replacement, shares similarities with the flight-level tangential wind pattern observed during the second ERC event of Hurricane Irma (2017), as documented by Fischer et al. (2020; see their Fig. 5).

Moreover, the radius-time Hovmöller diagram of azimuthally averaged reflectivity at an altitude of 3 km provides further evidence, indicating that the secondary eyewall began to form at 1430 UTC, which is 1.5 hours prior to the completion of the ERC, with a radius of 27 km from the TC center (black cross in Figure 21). This observation is consistent with the tangential wind field observed at elevations between 5 and 7 km. A contraction of the eyewall, similar to RMW evolution, was found in both the first and second intensification stages. The eyewall radius changed dramatically from ~12 km to ~18 km between the end of the first intensification stage and the beginning of the second

doi:10.6342/NTU202403267

intensifying stage. Another noteworthy observation is the displacement of the eyewall, defined by the region of peak reflectivity, relative to the RMW before and after the ERC. Prior to the ERC, the eyewall was situated inward of the RMW. However, after the ERC, the eyewall shifted outward and aligned with the RMW. The eyewall reflectivity reached 40–50 dBZ at approximately 0000 UTC on Sep 12 when the TC was evolving to the end of the peak stage. At the same time, the eyewall width started to increase and became much larger in the following weakening stage. Generally, the eyewall radii varied from 12 to 18 km during the first three stages.

doi:10.6342/NTU202403267

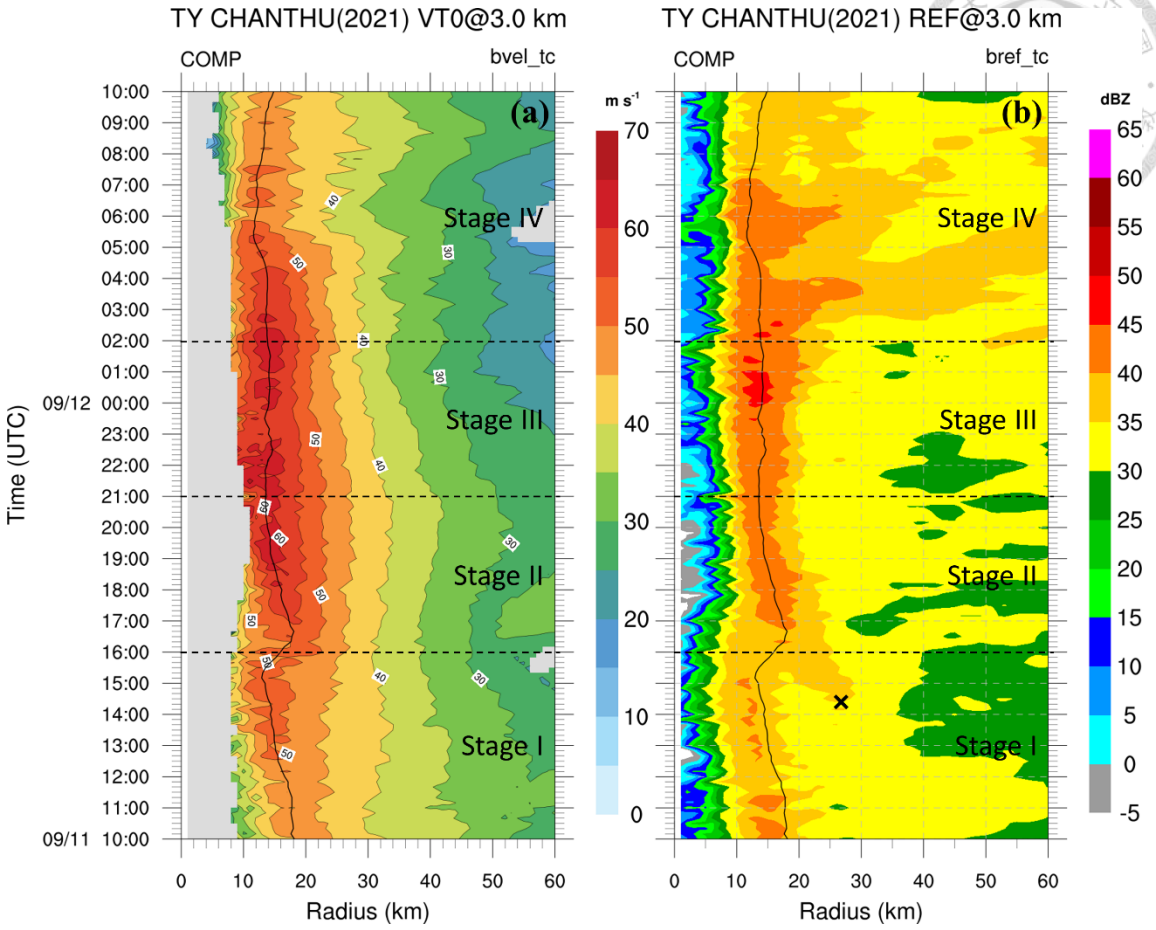

Figure 21. (a) Radius-time Hovmöller diagram of the GBVTD-derived axisymmetric tangential wind at 3-km altitude for Typhoon Chanthu, observed by the RCWF, RCHL, RCGI, and RCKT radars between 1000 UTC Sep 11 and 1000 UTC Sep 12, 2021. The shading intervals are every 5 m s^{-1}, and the black solid lines indicate the RMW. (b) Same as (a) but for the azimuthally averaged reflectivity field. The shading intervals represent the reflectivity every 5 dBZ, and the black solid lines indicate the RMW as shown in (a). The black cross marks the formation time of the secondary eyewall. The blue line along the ordinate indicates the time period with mean flow correction.

doi:10.6342/NTU202403267

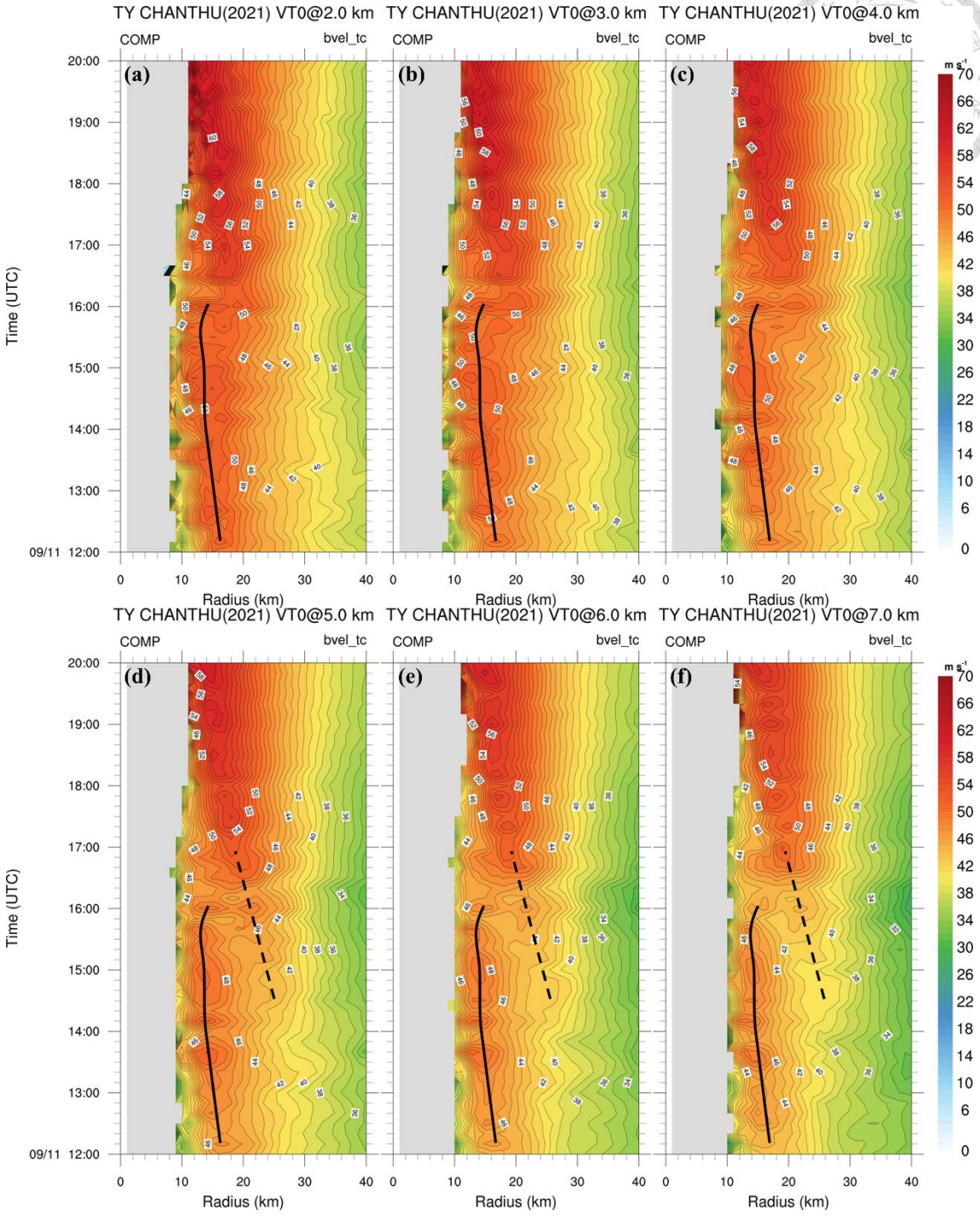

Figure 22. Same as Figure 21a, but for elevations from (a) 2 km to (f) 7 km with a 1 km interval. The contour intervals are 1 m s^{-1}. The black solid line indicates the RMW. The black dash line indicates the radius of secondary tangential wind maximum.

doi:10.6342/NTU202403267

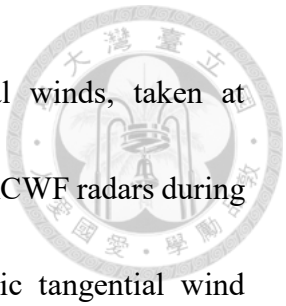

Figure 23 shows four snapshots of axisymmetric tangential winds, taken at approximately 6-hour intervals, from the RCKT, RCGI, RCHL, and RCWF radars during the analysis period. At 1010 UTC (Figure 23a), the axisymmetric tangential wind maximum reached 50 m s^{-1}, and the RMW was approximately 15 km at an altitude of 1 km. Additionally, a double-peak signal between altitudes of 3 and 6 km at radii of 15 km and 22 km was found. Approximately six hours later, axisymmetric tangential winds increased for all levels with a maximum wind speed of more than 55 m s^{-1} at 2 km. The double-peak signals were still apparent and could reach an altitude of 8 km (Figure 23b). The double peak in the tangential wind observed in Typhoon Chanthu resembles that observed in Hurricane Irma (2017) (Fischer et al. 2020; see their Fig. 11). At 2200 UTC (Figure 23c), the RMW contracted to 13 km, and tangential winds dramatically increased. The maximum wind speed reached more than 65 m s^{-1} at an altitude of 1 km, whereas the double-peak signal disappeared and reached sharper gradients horizontally and vertically compared with that at the previous analysis time. The tangential winds generally decreased with a maximum wind speed of 55–60 m s^{-1} occurring at an altitude of 1 km, as the typhoon center was located offshore of northeastern Taiwan, where the distance to the RCWF radar was 59 km at 0400 UTC (Figure 23d). Generally, the axisymmetric structure of tangential winds changed obviously during the analysis period. The vertical extent of tangential winds greater than 50 m s^{-1} varied from an altitude of 2 km to more than 10 km

doi:10.6342/NTU202403267

during the first three times analyzed. In addition, the horizontal extent for tangential winds greater than 35 m s^{-1} at an altitude of 2 km showed no significant difference from 40 km to 45 km during the intensifying stages. At the weakening stage, the radius for the horizontal extent of 35 m s^{-1} at an altitude of 2 km decreased to 30 km.

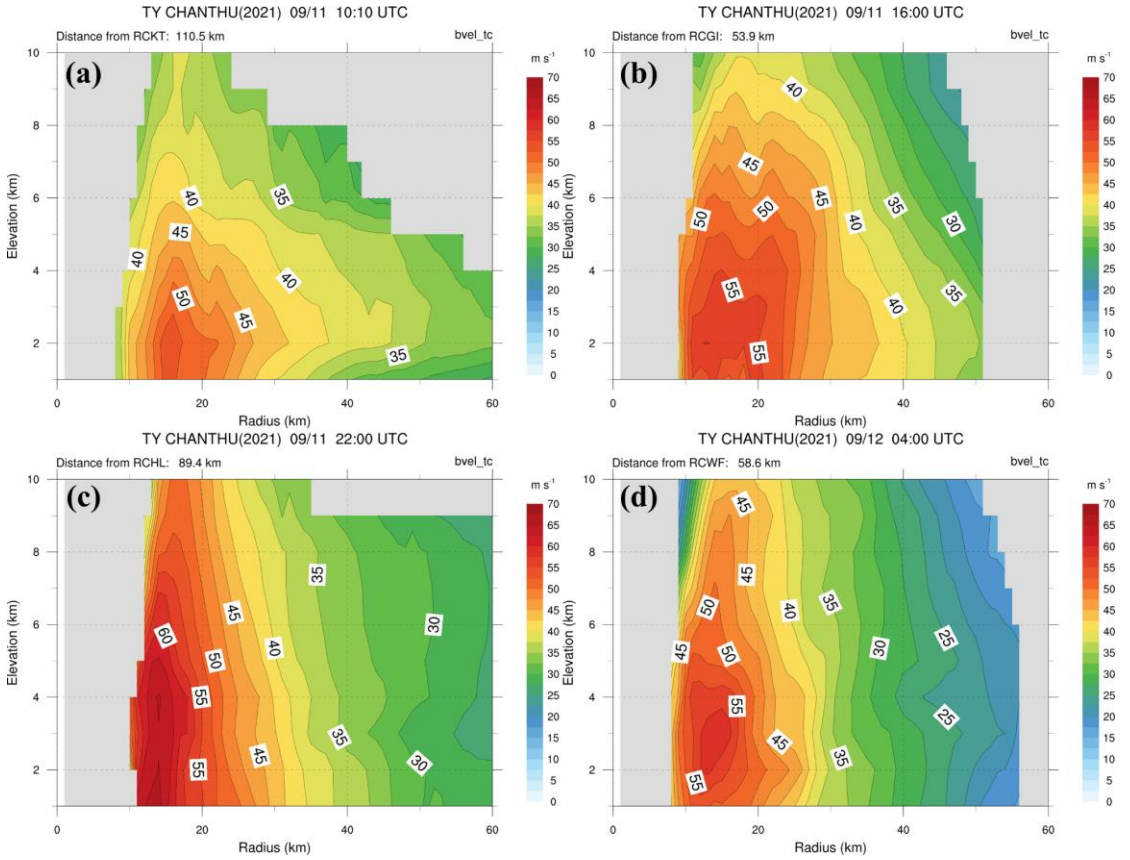

Figure 23. Axisymmetric structure of tangential winds at (a) 1010 UTC from RCKT, (b) 1600 UTC from RCGI, (c) 2200 UTC Sep 11 from RCHL, and (d) 0400 UTC Sep 12 from RCWF.

doi:10.6342/NTU202403267

3.4. Radar-derived mean flow and VWS

Figures 24a, b present the GBVTD-derived mean flow from 2 to 8 km altitude and the ERA5-derived mean flow from 800 to 350 hPa, respectively (see section 3.1 for details). The moving speed and direction of Chanthu calculated from the TCET track from 1000 UTC Sep 11 to 1000 UTC Sep 12 are also illustrated in Figure 24. The moving speeds of Typhoon Chanthu were mainly between 3 m s^{-1} and 12 m s^{-1}, with the moving directions distributed from north–northwest to north. The ERA5 DLM flow speeds were mainly between 3 m s^{-1} and 7 m s^{-1}, and the directions were mainly from the south–southwest, roughly agreeing with the typhoon motions. The GBVTD-derived DLM flow contained more detailed information because of its high spatial and temporal resolution and showed a better consistency with the TC moving speeds and directions than those from ERA5. In particular, the GBVTD-derived DLM flows accelerated after 2300 UTC on Sep 11, which is consistent with the apparent increasing speeds of Chanthu's movement. This indicates that the GBVTD-derived mean flow can approximately represent the steering flow when Chanthu is near Taiwan.

However, the VWSs derived from the two datasets were remarkably different. Both VWSs ranged from north–northeasterly to north–northwesterly before 1400 UTC on Sep 11. After 1600 UTC, the ERA5-derived VWS remained northerly, but the GBVTD-derived VWS apparently turned northwesterly. The magnitudes of the mean

doi:10.6342/NTU202403267

flows derived from the two datasets at an altitude of 8 km were similarly small. The major factor influencing the VWS difference between the two datasets was the direction of the LMF. The directions of both the GBVTD-derived and ERA5-derived mean flows were vertically homogeneous (e.g., south–southwesterly) between 1400 and 1600 UTC. Only the GBVTD-derived LMF turned from south–southwesterly to south–southeasterly after 1600 UTC. This change might be caused by the terrain blocking effect as the TC moved to the southeast offshore of Taiwan, which drove the LMF to turn south–southeasterly from the open ocean without being blocked. As the height of the southern part of the Taiwan terrain is lower than 2000 m, the flows above 3 km remained south–southwesterly. The mid- to upper-level mean flows decreased from ~5 to ~3 m s^{-1} and turned southwesterly after 1800 UTC. This change in direction resulted in a gradual increase in the GBVTD-derived VWS. It is worth emphasizing that the mean flow obtained from GBVTD characterizes the spatially averaged state within an annulus ranging from 30 to 60 km radii from the TC center, signifying a meso-β scale mean flow. In contrast, the ERA5-derived mean flow represents the mean wind within a 500-km radius from the TC center, corresponding to a meso-α scale mean flow. Consequently, the ERA5-derived LMF exhibited only minor changes in direction, which may have resulted from the inability of the ERA5 data to resolve the terrain-induced flow.

doi:10.6342/NTU202403267

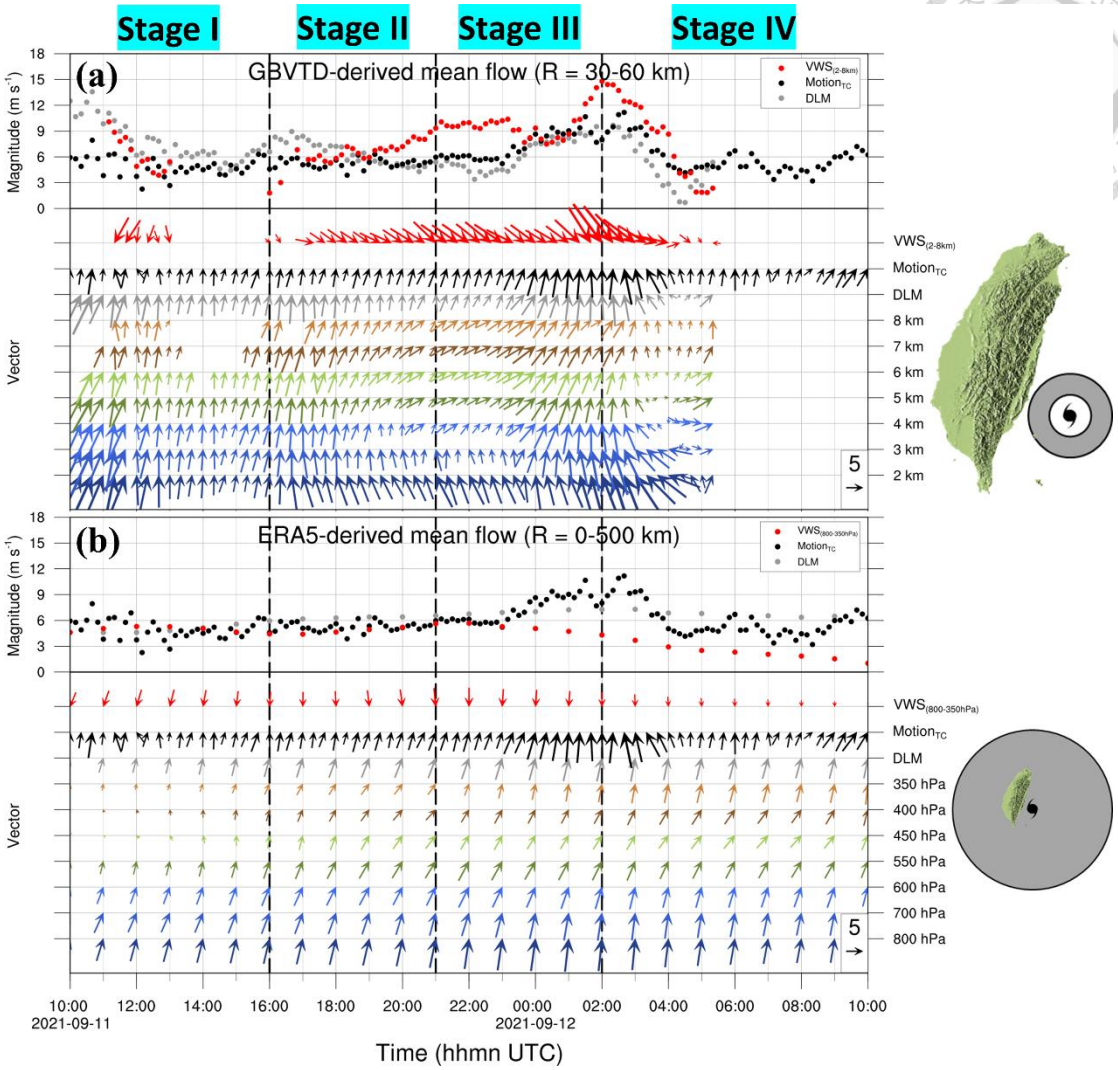

Figure 24. Temporal evolution of the mean flow in different layers (blue, green, and brown colors), along with the associated DLM (gray color) and VWS (red color) fields for Typhoon Chanthu. The mean flow is derived from (a) GBVTD retrievals and (b) ERA5 reanalysis data. TC motion derived from TCET centers is depicted in black. The GBVTD and TC motion fields are presented at 20-minute intervals, while the ERA5 reanalysis data are displayed at 60-minute intervals. The magnitude and direction of each field are represented by dots and arrows, respectively. A reference arrow length of 5 m s^{-1} is provided at the bottom right corner of the figure. The spatial coverage of the region represented by the GBVTD- and ERA5-derived mean flows relative to the geographical extent of Taiwan is illustrated on the right-hand side of panels (a) and (b).

doi:10.6342/NTU202403267

Wong and Chan (2004) suggested that the VWS estimated by different area-mean criteria could significantly affect the relationship between the VWS and TC intensity change. They found that the shears within areas close to the TC center (i.e., 200, 200–400, and 400–600 km) are larger than those within areas far from the TC center (i.e., 600–800 and 800–1000 km). The former shear also has larger temporal variations than the latter shear. Reasor et al. (2009) and Reasor and Eastin (2012) used airborne Doppler analyses to estimate the local VWS within 60 km from the center of Hurricane Guillermo (1997), and their results showed remarkable agreement with those of the Statistical Hurricane Intensity Prediction Scheme (SHIPS; DeMaria and Kaplan 1994; DeMaria et al. 2005). Reasor et al. (2013) utilized 75 TC flights of airborne Doppler radar data through a composite approach to examine the TC asymmetry induced by the VWS. However, they found that the local deep-layer shear from radar is on the clockwise side of large-scale shear by approximately 40°. This direction bias was also found in Cha et al. (2021), who used ground-based radars and airborne Doppler radar to analyze the ERC process of Hurricane Matthew (2016) influenced by a strong VWS. The above studies showed that estimating the VWS that can reflect what the TC core actually "feels" is important (Reasor and Eastin 2012; Boehm and Bell 2021). Therefore, a new estimation of the local VWS near the inner core region derived from ground-based radar is proposed in this study. The consistency of the GBVTD-derived (i.e., meso-β scale) and ERA5-derived (i.e.,

doi:10.6342/NTU202403267

meso-α scale) VWSs with eyewall asymmetry were also examined and compared as follows.

Figure 25 illustrates the time-azimuth distribution of reflectivity within the eyewall region, averaged over radii of RMW±2 km from the center of the TC. This analysis follows the methodology employed by Cha et al. (2021) to examine the asymmetric structure of the eyewall. Throughout the entire analysis period, a significant wavenumber-1 asymmetry was consistently observed, also depicted in Figure 19. Additionally, a counter-clockwise orientation of the eyewall wavenumber-1 asymmetry occurred just after the completion of the ERC. For the GBVTD-derived mean flow, the low-level mean flow turned from south–southwesterly to south–southeasterly after 1600 UTC, which caused a change in the VWS direction from northeasterly to northwestly (Figure 24). Accordingly, the DL quadrant of the GBVTD-derived VWS was initially observed approximately between east–southeast and south–southwest at 1100 UTC and subsequently rotated to a direction approximately between north–northeast and east–southeast after 1700 UTC (Figure 25b). This rotation of the VWS direction aligns well with the continuous presence of the reflectivity maximum on the left side of the shear. In contrast, the DL quadrant of the ERA5-derived VWS only exhibited a slight rotation to a direction approximately between east and south after 1600 UTC (Figure 25a). The reflectivity maximum was in the UL quadrant, which is inconsistent with previous studies

doi:10.6342/NTU202403267

when the eyewall asymmetry is contributed by the VWS. Thus, the direction of the GBVTD-derived VWS was 40~50° to the left of that of the ERA5-derived VWS when Chanthu was ~100 km from the Taiwan coast. This finding indicates that the GBVTD-derived meso-β scale VWS can properly reflect the sudden change in direction caused by the terrain and shows better agreement with the asymmetry of the TC eyewall. The above analyses reveal that a dense radar network can provide additional information, such as VWSs with high temporal resolution, for real-time diagnosis. It also indicates that when the TC was near the Taiwan terrain, the applicability of the ERA5-derived meso-α scale VWS may have been reduced.

doi:10.6342/NTU202403267

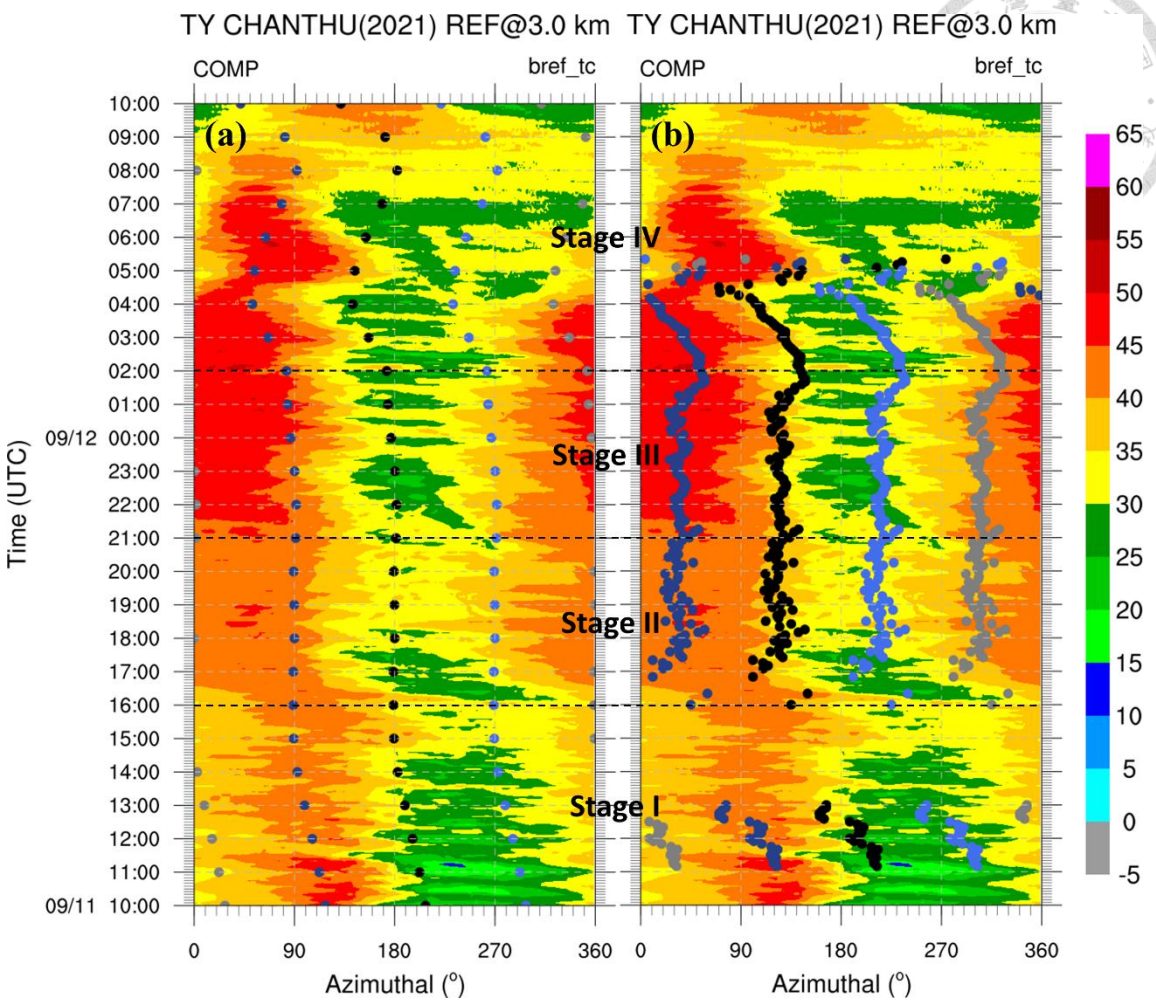

Figure 25. Same as Figure 21b but for the reflectivity averaged between over radii of RMW±2 km from TCET centers. The shading intervals indicate the reflectivity every 5 dBZ. Dots of black, gray, navy blue and royal blue color indicate the downshear, upshear, left-of-shear and right-of-shear sides determined from (a) ERA5 reanalysis data every 60 minutes and (b) GBVTD data every 10 minutes, respectively.

doi:10.6342/NTU202403267

3.5. Discussion

Typhoon Chanthu underwent RI when it moved roughly parallel to the eastern coast of Taiwan at a distance of approximately 100 km. Because the TC was very close to Taiwan, terrain effects might have played an important role in modulating the TC circulation at low levels that potentially contributed to TC intensification. In addition, this extremely compact (e.g., small RMW and strong near-core radial wind gradient) TC was also embedded in a moderate VWS. Shimada (2022) found that small TCs are less impacted by waters with relatively low ocean heat content (OHC) if the SST is sufficiently high; however, they are more vulnerable to VWS than large TCs. During the RI period in Typhoon Chanthu, the SST and OHC encountered by the storm remained above 29 ℃ and 100 kJ cm^{-1} (Figure 1), respectively. This indicates that Chanthu's RI was not primarily attributed to a positive change of the OHC. Consequently, Typhoon Chanthu's intensification relies on the support of additional internal or environmental factors to counteract the adverse effects of VWS. In this section, possible factors or processes, such as terrain effects and VWS profile patterns, will be discussed.

3.5.1 Terrain effects

To investigate the effects of flow detouring around the CMR near the surface on TC intensity change, wind observations from two island surface stations on Orchid Island (e.g., Lan-yu station) and Green Island in offshore areas of southeastern Taiwan and one

doi:10.6342/NTU202403267

weather buoy station in the north offshore of Orchid Island were analyzed. Figure 26 shows the composite dual-Doppler retrieval winds between 1400 and 1700 UTC on Sep 11 overlaid with surface wind observations. At 1400 UTC, the surface winds were generally consistent with the dual-Doppler retrieval winds aloft but with lower speeds. The surface wind directions near Orchid Island (green and cyan windbarb) were dominated by TC cyclonic circulation (Figure 26a). However, a change in wind direction was observed at the surface near Orchid Island starting from 1500 UTC, with winds turning more radially inward toward the TC center compared to earlier analyzed times at 1700 UTC (Figure 26d). This change in wind direction was not found at higher altitudes. In contrast, similar changes were not observed near Green Island. Therefore, the radial-inward change in surface wind direction near Orchid Island may have been induced by detouring flow around the terrain, which has the potential to converge with the primary circulation on the southeastern side of Chanthu.

To further investigate the vertical extent of terrain-induced circulation influence, the author analyzed the evolution of vertical wind profiles. These profiles were constructed from surface wind data from Lan-yu station and upper-level wind data from DDW, with the TC motion speed subtracted (Figure 27). As the TC moved northward from the southeastern to north–northeastern side of the Lan-yu station between 1000 and 1800 UTC on Sep 11 (Figure 1), the wind directions at every elevation roughly turned from

doi:10.6342/NTU202403267

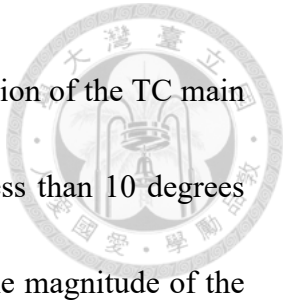

northwest, north to northeast, primarily agreeing with the wind direction of the TC main circulation. The inflow angles above Lan-yu station are basically less than 10 degrees because of the lack of the effect from surface friction. In contrast, the magnitude of the inflow angles near the surface wind are significant with a trend initially increasing (i.e. became more outward) at 1130 UTC and then decreasing (i.e. became more inward) at 1330 UTC again (Figure 27). This observed trend aligns with a dropwindsonde-based parametric model proposed by Zhang and Uhlhorn (2012), which performs a sequential change in inflow angles from the left-front, left, to left-rear quadrant relative to a TC's motion direction. However, the magnitudes of the inflow angles significantly exceeded those estimated by the parametric model, particularly after 1500 UTC, indicating that the influence was not only from friction but also from terrain. While both friction and terrain significantly alter the inflow angles, their effects are primarily confined to the boundary layer region.

To clarify whether the aforementioned inflow angles in the TC boundary layer were mainly driven by friction or terrain, a comparison was made between the inflow angles estimated by the parametric model proposed by Zhang and Uhlhorn (2012) and those obtained in this study. The parametric model indicated that for a TC with similar characteristics to Typhoon Chanthu, with a translational speed of 6 m s^{-1} and a maximum wind speed of 55 m s^{-1}, the storm-relative inflow angles in the left-rear quadrant are less

doi:10.6342/NTU202403267

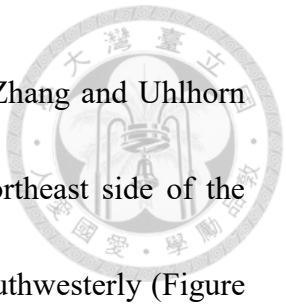

than 20 degrees (see the third row and third column of Fig. 14 in Zhang and Uhlhorn 2012). However, after 1400 UTC, when Chanthu moved to the northeast side of the Lan-yu station, the wind direction turned from northerly to west–southwesterly (Figure 26). The storm-relative inflow angles (Figure 27) exceeded 30 degrees (indicated by brown shading), surpassing the values estimated by the parametric model. It is thus suggested that the terrain effect can partly contribute to the increase in the inflow angle.

The sudden change in wind direction at Lan-yu station from northerly to west–southwesterly serves as an indicator for identifying the initiation of terrain-induced detouring flow (TDF), which is a unique phenomenon that occurs when TCs approach the east coast of Taiwan. As TCs approach the east coast, the airflow direction on the western side of Taiwan gradually transitions from being dominated by northerly components to westerly components. During this transition, the component of the airflow direction perpendicular to the terrain becomes more prominent, resulting in airflow blockage by the terrain and causing the airflow to shift in a south–southeast direction parallel to the terrain. This blockage persists until the airflow reaches the southern tip of Taiwan, where the blocking effect of the terrain diminishes, enabling the airflow to resume its movement toward the TC center. Finally, this detouring process forces the airflow to approach the TC center with a larger inflow angle. A demonstration of the surface streamlines of TDF can be found in Figure 28 (Figure 1a in Yeh and Elsberry 1993b).

doi:10.6342/NTU202403267

During the study period, the wind direction at Lan-yu station underwent a sudden change from northerly to west–southwestly within a span of 3 hours (1400 to 1600 UTC, Figure 27), which clearly indicated the initiation of TDF. The occurrence of TDF depends on the relative positions between the typhoon and Taiwan Island, the size of the typhoon's wind field structure, and the preexisting background flow direction. In cases where a TC approaches Taiwan from the eastern side with a much larger size than that of Chanthu, the initiation of TDF occurs earlier, even when the TC is still far from Taiwan. For instance, during the passage of Typhoon Soudelor (2015) with a 15 m s^{-1} radius extending over 400 km, as it approached Taiwan from the eastern ocean, the initiation of TDF was observed when the TC was over 200 km away from Lan-yu station. Although the impact of the TDF on TC intensification change is not fully understood and well documented, a numerical model simulation study of Typhoon Maria (2018) revealed the possibility that the TDF can cause TC intensification. Huang et al. (2020) claimed that when a TC moved to the northeast offshore of Taiwan, the terrain-enhanced low-level southerly flow east of Taiwan transported angular momentum to the eyewall, resulting in TC intensification. Therefore, the author suggests that the occurrence of TDF is a significant factor influencing the angles of TC inflow and a possible factor prompting TC intensification.

To further examine the vertical extent over which the circulation was influenced by terrain, the evolution of vertical wind profiles that combine the surface wind at the Lan-yu

doi:10.6342/NTU202403267

station and the DDW aloft were analyzed (Figure 27). The TC motion speed was subtracted from the wind profiles for quantitative comparisons with the theoretical tangential wind direction. It is found that the influence of TDF is related to the distance from the station to the RMW of the typhoon. Since the TDF speed is relatively small (~ 10 m s^{-1}) compared to the wind speed near the RMW, its impact on the wind direction becomes more evident as the station is located further away from the RMW. Therefore, when the station is approximately 2 times the RMW away, the observed wind direction deviates from the tangential wind due to the influence of TDF. With the TC moving northward and the distance between the station and the TC center increasing to more than 30 km (2 times the RMW), the TDF started to dominate the local circulation, and the wind direction turned west–southwesterly at approximately 1600 UTC (Figure 27), containing an inflow component compared with the tangential wind (brown shading in Figure 27). This process only extended to an altitude of approximately 1 km.

The direction of the GBVTD-derived VWS showed a transition from northeasterly to northwestly at approximately 1600 UTC (Figure 25b). According to the conceptual model proposed by Black et al. (2002), the VWS-induced updraft also shifted from the southern to southeastern section of the eyewall. The substantial inflow angle observed at the Lan-yu station after 1600 UTC, as illustrated in Figure 27, suggests that the TDF and the primary circulation of the TC may converge in the southeastern quadrant of the TC

doi:10.6342/NTU202403267

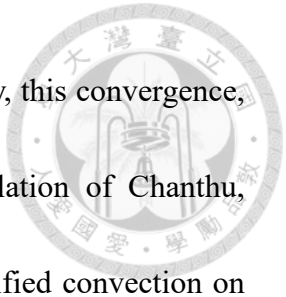

eyewall within the boundary layer (Huang et al. 2016). Consequently, this convergence, resulting from the interaction of the TDF and the primary circulation of Chanthu, coinciding with the updraft area induced by VWS, may have intensified convection on the downshear side. This enhanced convection can provide more energy transport to the cyclonic downstream to mitigate the radial ventilation effect due to VWS in the UL quadrant. The radius-time Hovmöller diagram of the averaged reflectivity in the eastern, northern, western, and southern quadrants within 100 km from the TC center is shown in Figure 29. Note that these quadrants also represent the DL, UL, UR, and DR quadrants only for stages II and III, as the VWS direction was approximately toward the southeast during these two stages (Figure 24). In stage II, the eyewall asymmetry was obvious. The eyewall on the left-of-shear semicircle accompanied by stronger reflectivity and a wider thickness than that on the right-of-shear semicircle was observed. This convection distribution generally agrees with the schematic illustration of the shear-induced eyewall convection asymmetry in Black et al. (2002) and Eastin et al. (2005). However, the narrower eyewalls with reflectivities above 35 dBZ in the UR and DR quadrants still underwent development. The development over the right-of-shear side indicated axisymmetric heating on the eyewall, benefiting TC intensification. The reflectivity enhancement on the UR side of the eyewall may have been caused by the VWS profile pattern, which will be further discussed in the following subsection.

doi:10.6342/NTU202403267

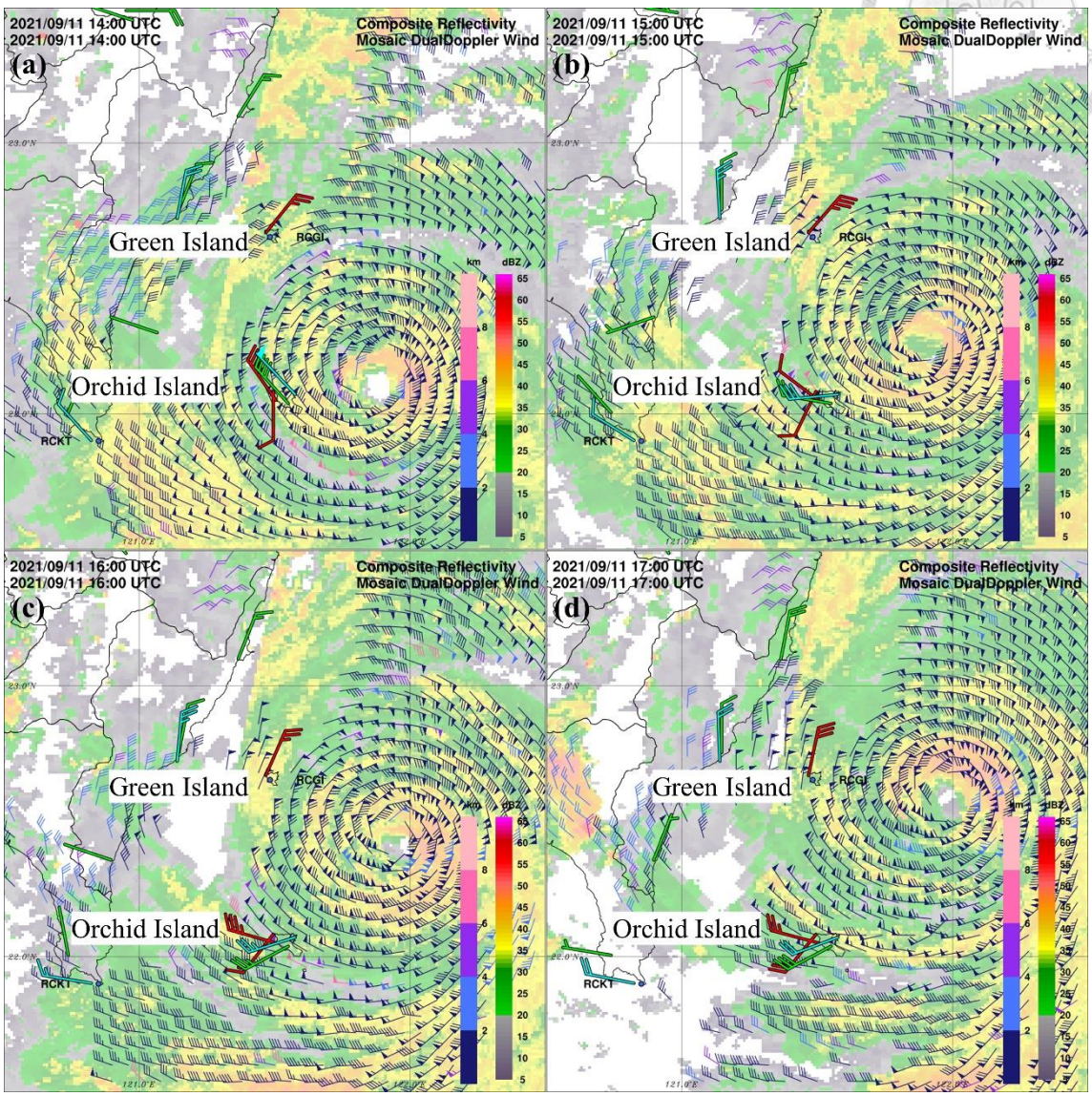

Figure 26. The composite dual-Doppler wind retrievals overlaid with surface wind observations at (a) 1400, (b) 1500, (c) 1600, and (b) 1700 UTC on Sep 11. The color bars of the DDW bars are the same as those in Figure 18. The green, red and cyan colors indicate the observations from surface stations, automatic surface stations and buoys, respectively.

doi:10.6342/NTU202403267

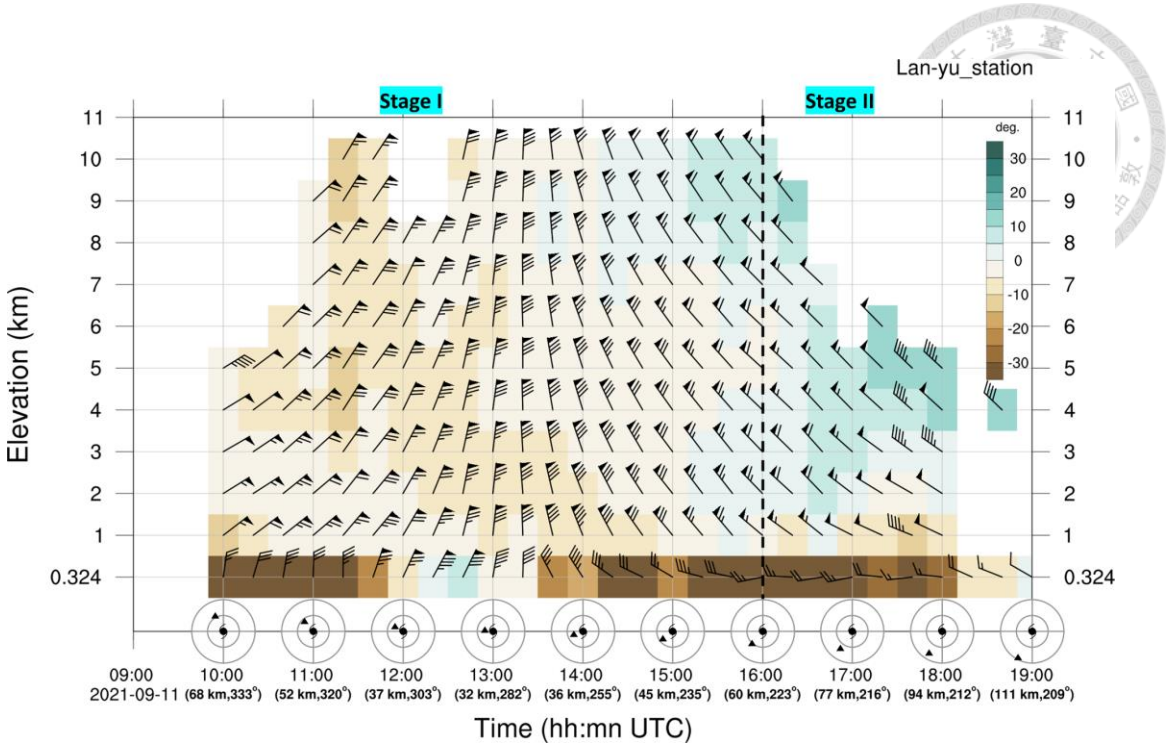

Figure 27. Temporal plot of storm-relative horizontal wind at the Lan-yu station, including data from the surface level (324 m) and altitudes ranging from 1 to 10 km. The background shading indicates positive (e.g., outflow; green color) and negative (e.g., inflow; brown color) degree differences compared with the tangential wind direction. The distance and azimuthal angle shown in parentheses beneath the UTC time indicate the position of Lan-yu station relative to the TC center. Illustrations along the abscissa depict the relative location between the TC center (typhoon symbol) and Lan-yu station (solid triangle). The interval between each circle of the illustrations is 60 km.

doi:10.6342/NTU202403267

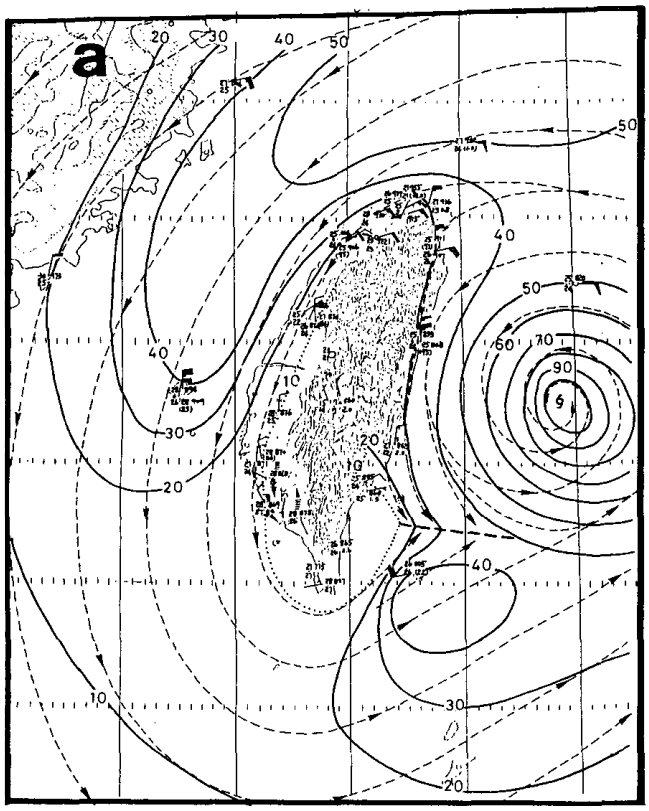

Figure 28. A demonstration of the surface streamlines of TDF. Adopted from Figure 1a of Yeh and Elsberry (1993b).

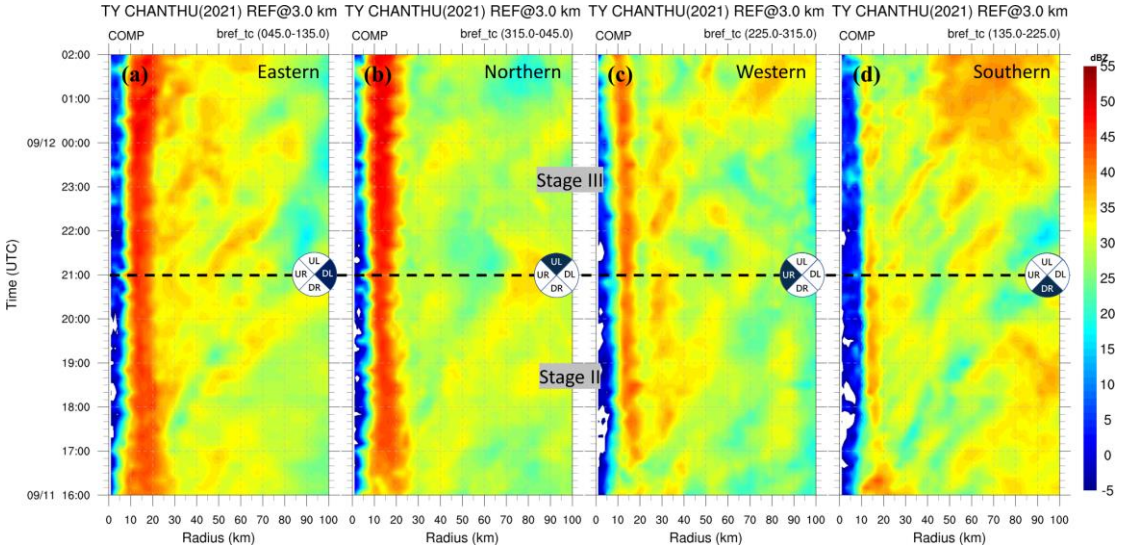

Figure 29. Same as Figure 21b but showing the azimuthally averaged reflectivity with 1 dBZ interval shading in the (a) eastern, (b) northern, (c) western, and (d) southern quadrants during stages II and III. Note that these quadrants correspond to (a) DL, (b) UL, (c) UR, and (d) DR, respectively, as the VWS direction was approximately toward the southeast during these two stages. The quadrants filled with a dark blue background in the circles indicate the shear-relative quadrants.

doi:10.6342/NTU202403267

3.5.2 VWS profile patterns

The consistency between the deep-layer (2 to 8 km) VWS and the eyewall asymmetry is discussed in Section 3.4. This subsection will focus on the possible impacts on TC intensification according to the VWS profile patterns. The deep-layer VWSs were further separated into lower-layer (2 to 5 km or 800 to 550 hPa) and upper-layer (5 to 8 km or 550 to 350 hPa) VWSs for a more detailed discussion. The characteristics of the lower- and upper-layer VWSs are detailed as follows. The GBVTD-derived lower-layer VWS magnitude decreased at 1100 UTC and approached nearly zero by 1400 UTC. The small-magnitude VWS remained for approximately 2 hours (Figure 30a; gray dots), during which Chanthu experienced the ERC process and the eyewall asymmetry was also reduced (Figure 25). The GBVTD-derived lower-layer VWS started to increase after 1600 UTC at a rate of 2 m s^{-1} per hour in the following 6 hours, and the shear direction turned from northerly to northwesterly. With variations in both direction and magnitude, the direction of the ERA5 VWS turned from north–northeasterly to north–northwesterly and only showed a minor change in magnitude (1.5–5.0 m s^{-1}) in the same period (Figure 30b; gray dots). The GBVTD-derived lower-layer shear direction also agrees well with the reflectivity maximum shift described in section 3.3 (Figure 25). The GBVTD-derived upper-layer VWS was very weak during almost the whole analysis period (Figure 30a; black dots). The magnitude only slightly increased after 0000 UTC Sep 12.

doi:10.6342/NTU202403267

Although an increasing VWS has been considered a negative factor for TC intensification, certain patterns of the VWS profile can provide a relatively favorable environment for eyewall convection to develop and cause axisymmetric heating (Rappin and Nolan 2012; Chen et al. 2019; Lee et al. 2021; Wadler et al. 2022). Figure 30a shows that the VWS derived from the GBVTD, especially at the lower level, increased during stage II as the TC rapidly intensified. During stage II of the study, the VWS direction estimated using the GBVTD analysis exhibited a southeastward orientation, while the LMF exhibited a north–northwestward direction (Figure 30a). This LMF, which imposed a UL-pointing flow onto the TC's primary flow, has the potential to augment the surface wind speeds and the associated heat fluxes within the downshear quadrant. These increased fluxes, advected by the TC's primary flow, resulted in a higher energy supply to the UL quadrant and enhanced the convection. (Lee et al. 2021; Rappin and Nolan 2012). Even though Chen et al. (2019, 2021) revealed that a DL-pointing LMF is favorable for TC intensification, the disagreement between their studies and this study may result from the relatively high initial intensity at which Chanthu underwent RI, differing from typical RI cases (Fischer et al. 2020). Statistical analyses (Chen et al. 2021) and idealized simulations (Chen et al. 2019) employing weak initial vortices may not be suitable for comprehensively elucidating the intensification mechanisms of Chanthu.

In addition to the relative direction between the VWS and LMF, the magnitude of the

doi:10.6342/NTU202403267

VWS vertical distribution is also one of the critical factors in determining whether a TC intensifies. The effect of a unidirectional VWS with the same magnitude (10 m s^{-1}) but different profiles on TC intensity change was discussed in Fu et al. (2019). They defined the lower-layer shear as the vector difference of the mean flow between heights of 1.3 and 5.8 km and the upper-layer shear between heights of 5.8 and 12.6 km. Two shear profiles were imposed on a TC with an intensity of ~60 m s^{-1}. The experiment imposing the upper-layer shear led to upper-level warm core weakening and vortex tilt, which consequently caused top-down weakening of the vortex. The GBVTD-derived VWS shows that the speed of the upper-layer VWS was less than 1.5 m s^{-1} during stage II, which was much smaller than that of the lower-level VWS (Figure 30a). This VWS profile pattern was less detrimental for TC intensification because the upper-level warm core of the vortex was under a weaker radial ventilation. The findings in this subsection indicate that the VWS profile pattern provides a relatively favorable environment for the intensification of Chanthu.

The results of this study are opposite to the arguments proposed by Finocchio et al. (2016). They argued that a shallower and lower VWS that tilts the simulated vortex to the downshear side is more destructive to the simulated vortexes. They also found that those tilted vortexes are unable to vertically realign and have a negative impact on intensification. Thermodynamic environments between low-level and upper-level VWSs

doi:10.6342/NTU202403267

have been compared. It is suggested that the middle-level dry air entrainment is a possible factor that induces a low equivalent potential temperature flux into the boundary layer for low-level VWS experiments. In contrast, the low equivalent potential temperature downdraft flux in the upper-level VWS experiments is less active. Nevertheless, the author suggests that the impact of VWS on the intensity change of TCs varies depending on their intensity or size levels (Finocchio and Rios-Berrios 2021). The intensity of Typhoon Chanthu over the analyzed period in this study ranges from ~50 to ~65 m s^{-1}. The initial vortex used for the simulation in Finocchio et al. (2016) is relatively weak (30 m s^{-1}) compared to that of Chanthu. The relationship between the depth of the steering layer and vortex intensity, as shown in Velden and Leslie (1991), implies that the vortex depth of intense TCs is higher than that of weak TCs. As a result, the shear layers focused on the upper level have less impact on weak TCs due to their shallow vortex depth. In contrast, the shear layers focused on the lower level can cause the tilt of weak TCs and be more destructive to their intensity (Finocchio et al. 2016). For intense TCs, such as the model setting in Fu et al. (2019) with an initial vortex of 60 m s^{-1}, the resistance from low-level shear is higher due to their high inertial stability at the lower level. However, shear at the upper level can be harmful to the warm core of intense TCs and lead to significant weakening.

doi:10.6342/NTU202403267

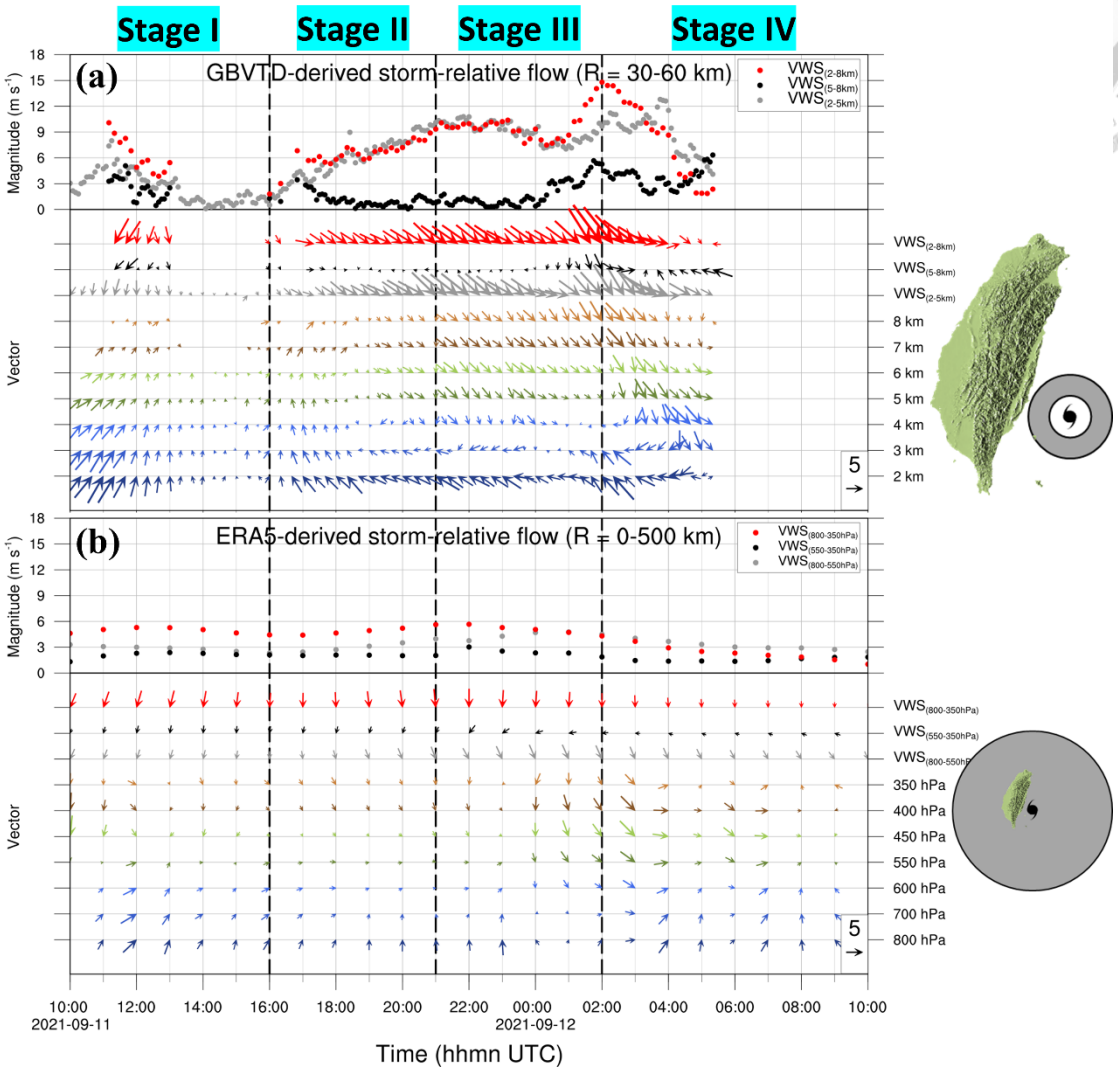

Figure 30. Same as Figure 24 but for the storm-relative mean flows. Arrows and dots represent the direction and magnitude of VWS at different altitude ranges. Ranges from 2 to 8 km (800 to 350 hPa), 5 to 8 km (550 to 350 hPa), and 2 to 5 km (800 to 550 hPa) are presented in red, black and gray colors.

As mentioned above, the VWS profile pattern appears to have provided a favorable environment for Typhoon Chanthu to quickly intensify with less harm to its mid- to upper-layer warm core. Moreover, the terrain-induced boundary inflow led to convergence enhancement in the DL quadrant of the eyewall and could have also prompted convection development and further intensification. Although the main goal of

doi:10.6342/NTU202403267

this study was to discuss the mechanisms of RI, Chanthu also notably underwent RW during the last 8 hours of the analysis period. Such a rapid change in intensity is also an important issue for research on TC intensity and forecasting. Previous studies indicate that the main factors resulting in RW include a sharp SST gradient, low OHC, increasing VWS, dry air intrusion and interaction with the monsoon gyre (DeMaria et al. 2012; Wood and Ritchie 2015; Liang et al. 2016; Liang et al. 2018; Wada 2021). During the period of RW in Typhoon Chanthu, the SST encountered by the storm remained above 29 ℃. However, a notable decline in the OHC was observed along Chanthu's track in the northeastern offshore region of Taiwan, decreasing from 80 to 40 kJ cm^{-1} (Figure 1). This suggests that the reduced OHC in the vicinity may have contributed to the occurrence of RW in Chanthu. Additionally, subsidence warming associated with the adiabatic warming of downslope flow was induced by the eastward wind component originating from the southern quadrant of the typhoon circulation across the CMR (Chen et al. 2010; Hsu et al. 2018) (Figure 18d). The dry air from this subsidence warming may have intruded into Chanthu's inner core, potentially causing the weakening of the TC. Nonetheless, importantly, the intricacy of the mechanisms responsible for the RW of Chanthu exceeds the limitations of the data utilized in this study. Therefore, future research aimed at delving into the underlying mechanisms of RW in TCs is important to enhance our understanding of this phenomenon.

doi:10.6342/NTU202403267

3.5.3 Banded reflectivity feathers outside the eyewall

Examples of thin bands of enhanced reflectivity are shown in Figure 31. The banded reflectivity structure, triggered in the eastern quadrant from the inner eyewall with a radial wavelength of approximately 10 km was observed by RCKT on Sep 11 at 1100 UTC (Figure 31a). These banded features of Chanthu were very active during both the intensifying stage (eastern quadrant in Figures 31a, b) and weakening stage (northern quadrant in Figure 31c). The radially-propagating banded reflectivity could also be observed through the azimuthally averaged reflectivity (Figure 29). The banded reflectivity adjacent to the eyewall exhibited significant outward propagation, with a speed of ~5 m s^{-1} throughout the entire analysis period across all quadrants. Furthermore, the rainbands in the UR quadrant were continuously triggered at a radius of 30 km from the TC center, propagated radially outward, and dissipated at a radius of ~50 km. The quasi-stationary rainbands, similar to the secondary eyewall in the UR quadrant, may have been caused by the interaction between the TC primary circulation and the terrain on the western side of the TC and were observed only during stages II and III.

Previous studies have indicated that vortex Rossby waves (VRWs) can propagate azimuthally and radially outward, contributing to TC intensification or secondary eyewall formation (Guimond et al. 2020; Montgomery and Kallenbach 1997). To investigate whether these banded reflectivities were triggered by VRWs, azimuthal

doi:10.6342/NTU202403267

Fourier decomposition of the eyewall reflectivity and tangential wind speed was applied. Based on the RMW of approximately 15 km and a V_{max} exceeding 50 m s^{-1} at an altitude of 3 km, the theoretical azimuthal propagation speed of the wavenumber-2 VRWs (e.g., Guinn and Schubert 1993; Kuo et al. 1999) should complete one rotation around the eyewall within approximately 60 minutes. However, it was found that the azimuthal propagation of wavenumber-2 VRWs was not evident in either the eyewall reflectivity or the tangential wind. Consequently, this study did not find sufficient evidence of VRW activity in Chanthu, except for the presence of banded feathers in the reflectivity field. Considering that these banded reflectivities episodically emanated throughout the entire analysis period as Chanthu moved along the eastern coast of Taiwan, further research is recommended to ascertain their contribution to Chanthu's intensification.

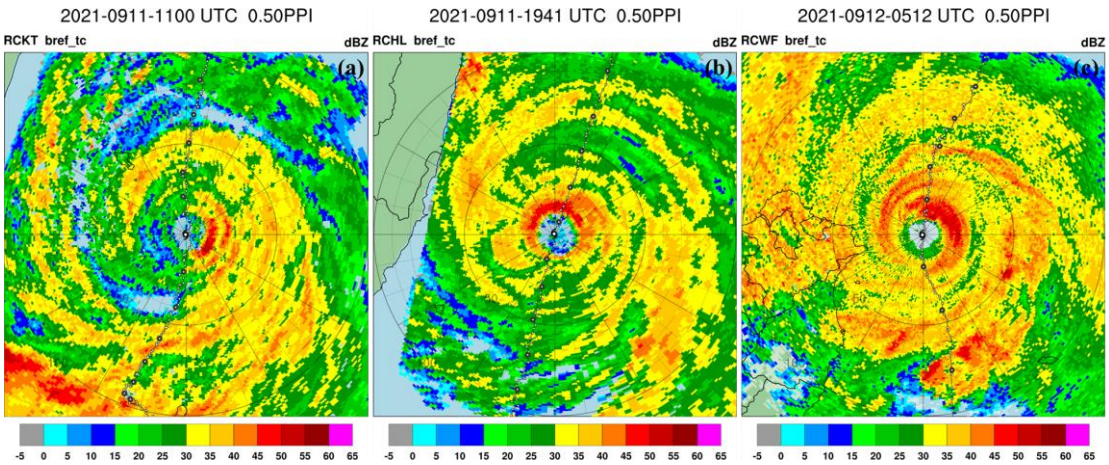

Figure 31. Examples of reflectivity fields at a 0.5° elevation angle from (a) RCKT at 1100 UTC Sep 11, (b) RCHL at 1941 UTC Sep 11, and (c) RCWF at 0512 UTC Sep 12. The coordinates are centered at the typhoon center, which was determined using the TCET algorithm. The thick (thin) black circles denote radial distances from 0 km to 200 km with a 50 (10) km interval. The TECT tracks determined by individual radars are imposed. Small (large) hollow dots indicate the TCET centers every 6~8 (~60) minutes.

doi:10.6342/NTU202403267

4. Vortex initialization strategies for a compact TC

Based on the analysis of radar data, it is evident that Chanthu is an extremely compact TC. The primary objective of this chapter is to investigate effective methods for initializing such a compact TC in numerical models. Initially, two data assimilation strategies are conducted and examined through idealized experiments. Subsequently, simulations from the two experiments on Chanthu are compared with observations to identify the most accurate approach. Finally, suggestions for future research aimed at improving the performance of simulations are provided.

4.1. Numerical model Configuration

This study utilizes version 3.9.1 of the Weather Research and Forecasting (WRF) model in conjunction with the WRF 3DVAR data assimilation system (Barker et al. 2012). The model configuration follows the setup described by 蔡等 (2019; Radar WRF), which focused on radar data assimilation. The vertical structure includes 52 layers, with the model's atmospheric top set at 20 hPa. The physical parameterizations used are the NOAH land surface model (Tewari et al. 2004), the WRF single-moment 6-class microphysics scheme (Hong and Lim 2006), the YSU boundary layer scheme (Hong et al. 2006), and the RRTMG longwave and shortwave radiation schemes (Iacono et al. 2008).

To avoid directly downscaling from the tens-of-kilometers grid size of the EC

doi:10.6342/NTU202403267

global model to a few kilometers, the model grid design employs the Typhoon WRF (TWRF; Hsiao et al. 2010) with an outer domain at 15 km and an inner domain at 3 km grid size. The simulation starts from 1800 UTC on Sep 10, with partial cycling assimilation (Hsiao et al. 2012) employed at 0000 UTC on Sep 11 with 36 hours free forecast. Subsequently, at 0000 UTC on Sep 11, the inner 3 km grid data from TWRF are downscaled to provide initial and boundary conditions for the RWRF's 1 km grid. Data assimilation using reflectivity and Doppler velocity from 10 radars listed in Table 2 (except for the ISHI radar) was conducted for 9 hours (0000 to 0900 UTC) with a 30-minute assimilation interval. The simulation then started at 0900 UTC on Sep 11 with a length of 30 hours. The extents of the grid layers are depicted in Figure 32.

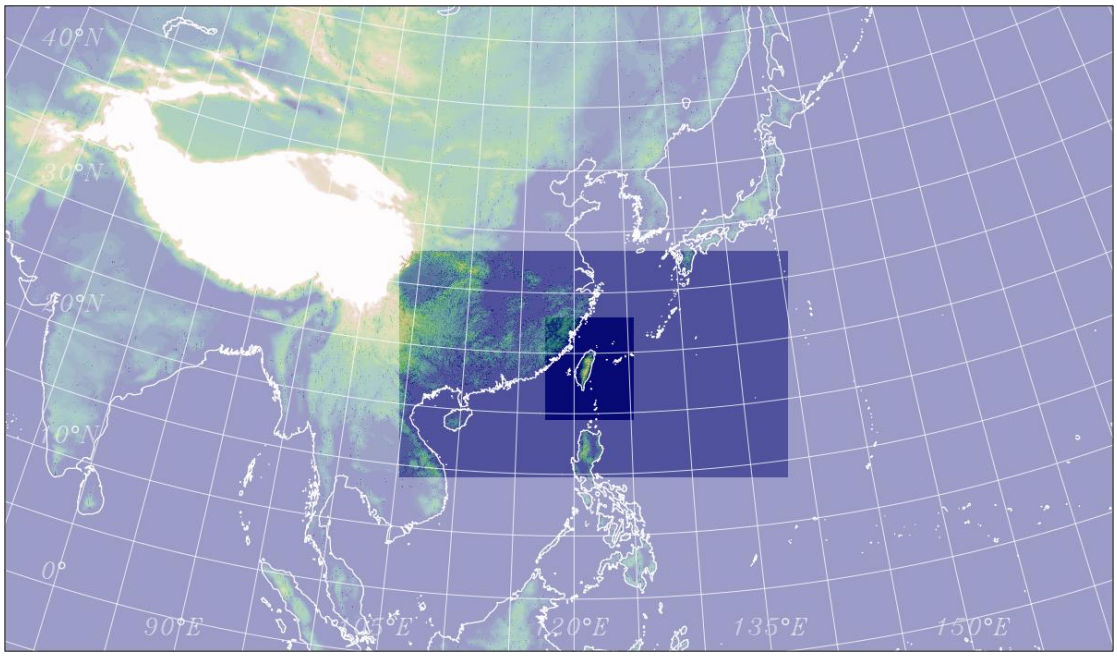

Figure 32. The model domain configuration with 3 nested domains. The grid sizes of the two outermost domains are 15 km and 3 km, which are the domain settings for TWRF. The grid size of the inner domain is 1 km, used for radar data assimilation.

doi:10.6342/NTU202403267

4.2. Idealized experiments

Since Doppler velocity is only a projection of the real wind field, specific areas covered by two radars are required to accurately retrieve the actual wind field, presenting limitations for assimilation. This section discusses the differences between assimilating data from a single radar and from two radars through idealized experiments to understand these limitations. Additionally, the results of two preprocessing methods for Doppler velocity assimilation are also compared through idealized experiments. Assimilating Doppler velocity in its original polar coordinates with thinning is a common method for data assimilation. However, the data density decreases with distance from the radar, reducing the effectiveness of assimilation. Accordingly, this study employs a preprocessing step that involves interpolating the data onto model grid points using constant altitude coordinates before assimilation.

To improve the quality of the model's initial conditions, the data assimilation system must consider the errors in both observational data and the background field to create a well-balanced combination that yields optimized initial fields for the model. In the model framework, certain physical processes are either simplified to reduce computational load or not fully understood, leading to discrepancies between model outputs and real-world conditions. The differences between observed values and those derived from the model's physical framework are referred to as observation errors,

doi:10.6342/NTU202403267

which comprise representation errors and measurement errors. One significant source of representation errors is preprocessing errors (Janjić et al. 2018). The first step of this section is to explore methods to minimize these errors through appropriate preprocessing techniques.

Radar data are originally in polar coordinates, resulting in very high data density near the radar. To prevent unnecessary computation and the introduction of high-frequency signals that the model cannot resolve due to the higher density of observational data compared to model grid density, super-observation processing is typically applied to denser observational data. For preprocessing Doppler velocity fields, previous studies have generally employed two approaches: thinning the data in the original polar coordinates (Sun and Crook 2001; Rihan et al. 2008; Simonin et al. 2014; Rennie et al. 2020) or interpolating radar observations onto the model grid points (Xiao et al. 2005; Pan et al. 2012; Mazzarella et al. 2020). The former method avoids errors associated with data interpolation, while the latter reduces errors when converting model space data into observation space via the observation operator. However, the impact of these two preprocessing methods on the analysis field remains unclear. Additionally, since Doppler velocity fields only reflect velocity components along the radar's line of sight, the limitations imposed by radar coverage on data assimilation have not been fully addressed.

doi:10.6342/NTU202403267

For the wind field, this study preprocesses the Doppler velocity field by thinning the data in the original polar coordinates (referred to as VRP) and by interpolating the data onto model grid points using constant altitude coordinates (referred to as VRC). VRP involves direct thinning in the radar's original coordinates, where data density is higher closer to the radar. This method ensures that the spatial distribution of the thinned data matches the distance between model grid points. According to 蔡等 (2019), data are thinned at distances of 6-15 km, 15-30 km, 30-60 km, and 60-120 km from the radar by retaining only 1 out of every 6, 5, 3, and 2 data points, respectively. Data beyond 120 km from the radar are not thinned.

The VRC method utilizes the Adaptive Barnes interpolation technique (Askelson et al. 2000) to interpolate radar data onto model grid points using constant altitude coordinates (CAPPI, Constant Altitude Plan Position Indicator). The formula is as follows:

$$f_a(i) = \frac{\sum w(k) \cdot f_o(k)}{\sum w(k)} \qquad (10)$$

$$w = exp\left(-\frac{r_{ik}^2}{\kappa_r} - \frac{\phi_{ik}^2}{\kappa_\phi} - \frac{\theta_{ik}^2}{\kappa_\theta}\right) \qquad (11)$$

where f_a represents the value at the analysis grid point, w is the weighting function, and f_o is the observed value in the original coordinates. The weighting function w is a function of the differences in radial distance (r_{ik}), azimuth (ϕ_{ik}), and elevation angle (θ_{ik}), which can be calculated using Equation (2). The parameters κ_r,

doi:10.6342/NTU202403267

κ_ϕ, and κ_θ determine the influence range of the observational data in the radial, azimuthal, and elevational directions, respectively, and are all set to 0.336.

To simplify the complexity of the problem, idealized experiments is initially conducted. This section evaluates uniform and rotational flow fields and tests the characteristics of the analyzed wind field after assimilating Doppler velocity data under single-radar and dual-radar scenarios. The two radars are simulated at the locations of RCWF and RCHL, with a maximum observational range set to 300 km.

The advantages of using idealized cases include: (1) Known wind field information in ideal experiments, making it easier to evaluate the accuracy of the results; (2) The ability to test various combinations of background wind fields and Doppler velocity fields to understand the method's limitations; (3) High data integrity, reducing uncertainties caused by insufficient data coverage. These advantages simplify the problem by ensuring that the background field (B), observational field (O), and analysis field (A) are known, facilitating the calculation of variables such as innovation (O-B), increment (A-B), and analysis departure (O-A), thereby elucidating the characteristics of the method.

4.2.1 Uniform flow experiment

This ideal experiment assumes that both the background wind field and the observed wind field are uniform flow fields. The background field consists of a westerly

doi:10.6342/NTU202403267

wind at 15 m s^{-1}, while the observed field, with the same wind speed but a northwesterly direction differing by 45 degrees from the background, is simulated as the Doppler velocity field observed by the Wufenshan radar. The wind fields at all heights are identical. Since the Doppler velocity field only contains the projection of the wind field in the radar's line of sight, it is not possible to directly calculate the differences in the zonal (U) and meridional (V) wind components between the background and observed fields during assimilation. Therefore, the background field needs to be interpolated to the observation data locations and converted to the Doppler velocity field (Figure 33a). By subtracting the observed Doppler velocity field (Figure 33b), the observation increment (innovation) can be obtained (Figure 33c).

As the background and observed fields are uniform horizontal flow fields, the theoretical observation increment should also be uniform horizontally. However, Figure 33c shows that due to the uncertainties introduced by the characteristics of the Doppler velocity field, the observation increment is a function of the radar's azimuth. The minimum observation increment occurs at azimuth angles of 112.5 degrees and 292.5 degrees, while the maximum positive and negative increments are at 202.5 degrees and 22.5 degrees, respectively. This observation increment also affects the distribution of the analysis increment. In the VRP experiment, the analysis increment exhibits similar characteristics to the observation increment, with the region where the analysis

doi:10.6342/NTU202403267

increment exceeds 10 m s^{-1} extending up to 150 km from the radar (Figure 34a). When the Doppler velocity field is interpolated onto the model grid's constant altitude coordinates before assimilation (VRC), the region where the analysis increment exceeds 10 m s^{-1} extends to nearly 300 km from the radar (Figure 34b), matching the radar's maximum observational range (Figure 34b, black dashed line).

The absolute value of the analysis increment exhibits a wavenumber-2 pattern in the radar's azimuthal direction, leading to a similar wavenumber-2 distribution in the wind speed of the analysis wind field (Figure 35). In this pattern, the wind speed is lower (less than 15 m s^{-1}) in the first and third quadrants and higher (greater than 15 m s^{-1}) in the second and fourth quadrants, with the wind speed and direction at azimuth angles of 202.5 degrees and 22.5 degrees closely matching the assumed observed wind field (northwesterly wind at 15 m s^{-1}). This indicates that assimilating a single radar's Doppler velocity field can introduce artificial local convergence or divergence when there are discrepancies between the background and observed fields, even if the observation error is smaller than the background error, making it difficult for the analysis wind field to effectively adjust towards the observed wind field. Comparing VRP and VRC, the VRC preprocessing method allows the observational data to influence closer to the maximum observational range, resulting in a larger area of local convergence or divergence compared to the VRP experiment.

doi:10.6342/NTU202403267

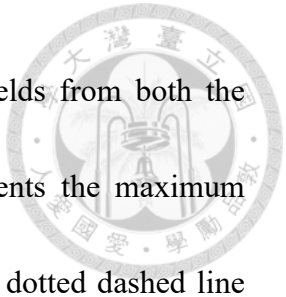

Figure 36 shows the analysis departure for the assimilated fields from both the simulated Wufenshan and Hualien radars. The dashed line represents the maximum coverage of the Doppler velocity fields from both radars, while the dotted dashed line indicates the maximum coverage of dual-Doppler wind fields at an altitude of approximately 6 km. The results show that in the VRP experiment, at 3 km altitude, the area with an analysis departure less than 2 m s^{-1} corresponds to the dual-Doppler coverage at this height. In contrast, in the VRC experiment, the area with an analysis departure less than 2 m s^{-1} matches the maximum dual-Doppler coverage and includes regions where the analysis departure approaches 0 m s^{-1}. This indicates that the VRP preprocessing method can yield an analysis wind field similar to the observed wind field within the dual-Doppler coverage area, but with a discrepancy of about 2 m s^{-1}, and the influence of upper-layer data does not extend downward. The VRC preprocessing method, on the other hand, can produce an analysis wind field almost identical to the observed wind field within the dual-Doppler coverage area, with the influence of upper-layer data extending downward, resulting in a broader area resembling the observed wind field compared to the maximum dual-Doppler coverage at this height.

The analysis wind field from assimilating both radars' Doppler velocity fields (Figure 37) shows that the analysis wind field not only closely matches the assumed observed wind field at azimuth angles of 202.5 degrees and 22.5 degrees but also in

doi:10.6342/NTU202403267

regions covered by both radars. However, the VRC's coverage extension is larger than that of the VRP. In regions covered by only one radar, local convergence and divergence are still introduced.

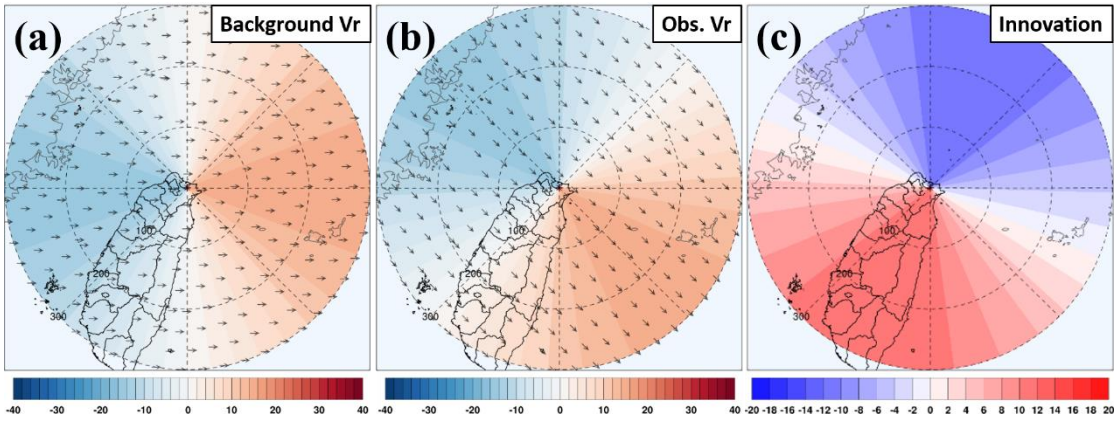

Figure 33. (a) Doppler velocity derived from the background horizontal wind field, (b) observed Doppler velocity, and (c) innovation. The color shadding represents Doppler velocity, and the black arrows indicate wind vectors.

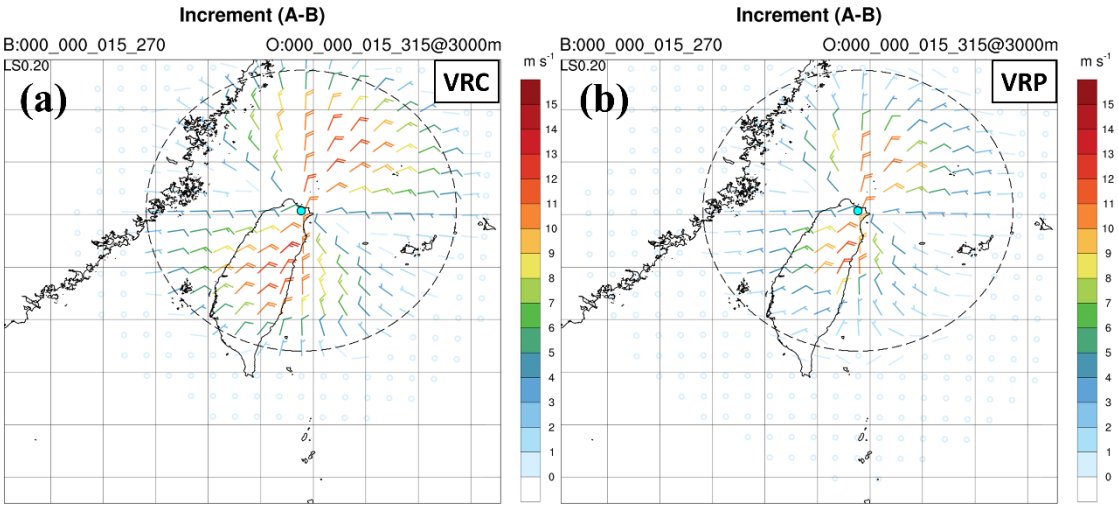

Figure 34. Analysis increment from data assimilation of the simulated RCWF observed Doppler velocity in the uniform flow ideal experiment after (a) interpolating to the model grid's constant altitude coordinates (VRC) and (b) thinning in the radar's original coordinates (VRP). The black dashed line indicates the maximum coverage range of the radar data.

doi:10.6342/NTU202403267

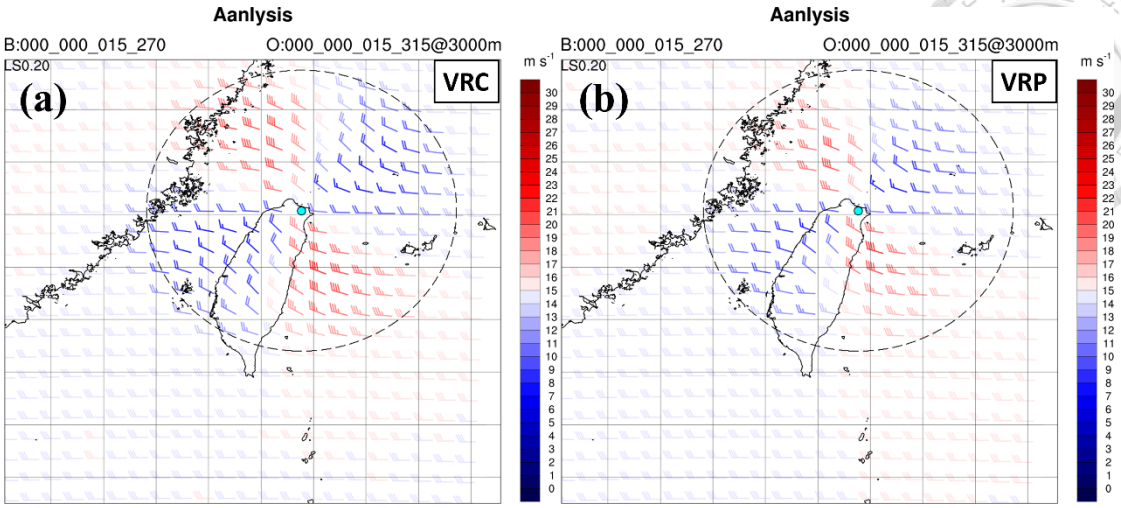

Figure 35. Same as Figure 34, but for the analysis after data assimilation.

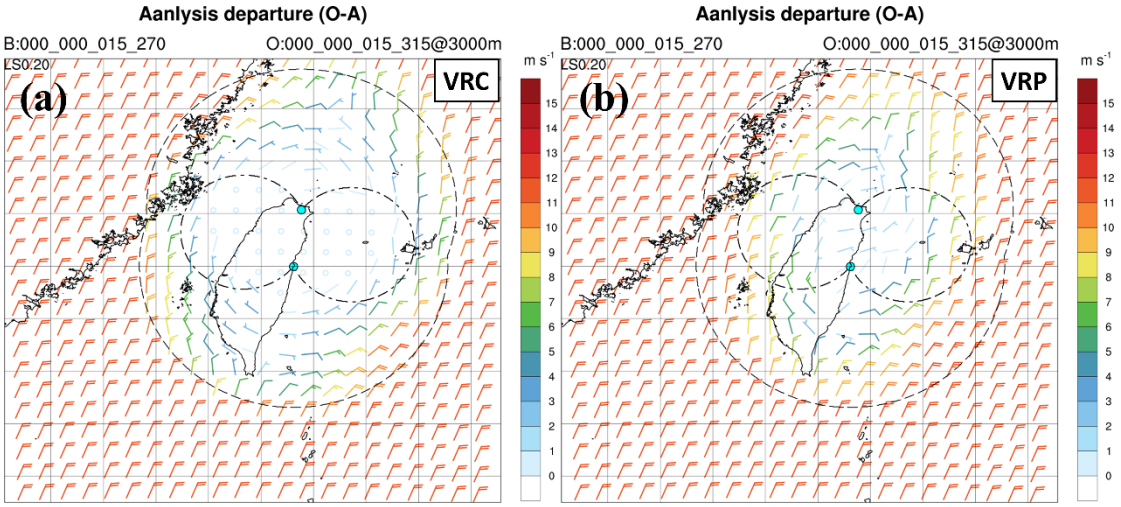

Figure 36. Same as Figure 34, but for the analysis departure for simultaneous assimilation of Doppler velocity from simulated RCWF and RCHL radars. The black dashed line indicates the maximum coverage range of the radar data, and the black dotted-dashed line represents the maximum range covered by both radars simultaneously.

doi:10.6342/NTU202403267

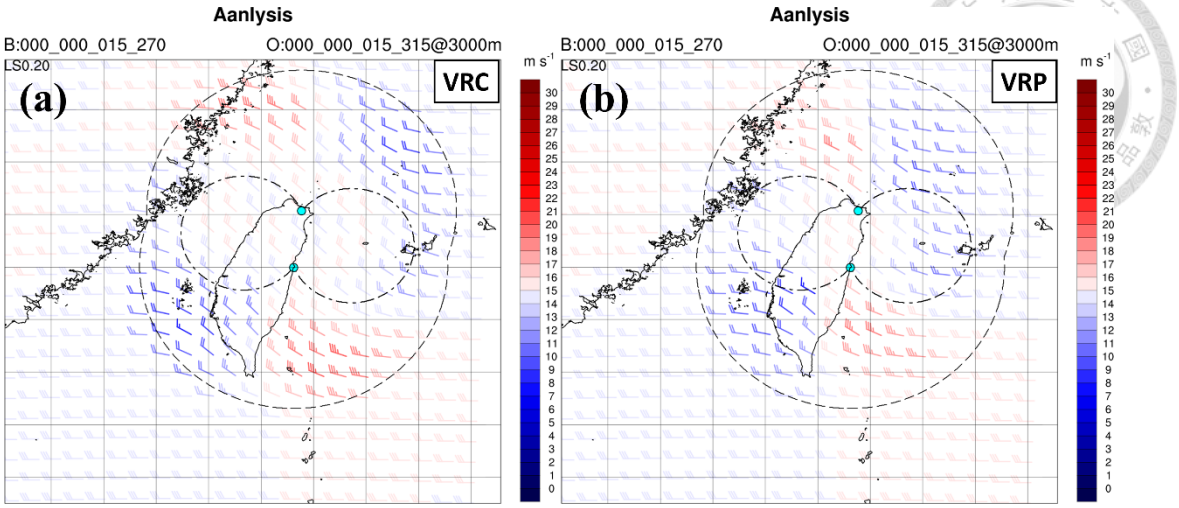

Figure 37. Same as Figure 36, but for the analysis after data assimilation.

4.2.2 Rotational flow experiment

To understand the characteristics of assimilating Doppler velocity fields in typhoon cases, this study also conducts ideal experiments on rotational flow fields. These experiments aim to assess the effectiveness of Doppler velocity field assimilation in correcting the vortex center position or structure when there are discrepancies between the background and observed vortex positions or wind field structures. In this section, the experiment assumes that both the background and observed vortices are located 150 km southeast of the RCWF, with a maximum wind speed of 30 m s^{-1} and a maximum wind speed radius of 30 km. The ideal vortex wind field distribution is calculated using Equation (3) and (4), with the same wind field at all heights.

The analysis deviation results indicate that, although the background and observed vortices have identical structures and positions in the experiment design, the VRP

doi:10.6342/NTU202403267

preprocessing method still results in slight analysis increments near the vortex center, with a maximum value reaching 2 m s^{-1} (Figure 38a). In contrast, the VRC experiment yields a reasonable distribution of analysis increments, with the maximum value appearing near the vortex center but not exceeding 1 m s^{-1} (Figure 38b). To simulate discrepancies in the vortex position or structure between the background and observed fields, this study places the observed vortex 150 km southeast of the RCWF, with a maximum wind speed radius of 30 km and maximum wind speeds of 20, 30, and 40 m s^{-1}. The background vortex is positioned 50 km northeast of the observed vortex, with the same maximum wind speed and radius (30 m s^{-1} and 30 km), simulating scenarios where the observed and background vortex intensities differ. The analysis wind field deviations after preprocessing using VRP and VRC methods are shown in Figure 39. The results indicate that, regardless of the intensity differences between the background and observed vortices, the VRC method produces minimal deviations (less than 1 m s^{-1}) within the dual-radar coverage area (Figure 39a, c, e), suggesting that the VRC method effectively adjusts the vortex center to the correct position and closely matches the observed vortex wind field structure (Figure 40a, c, e). In contrast, the VRP experiment shows significant analysis deviations southeast of the observed vortex center (Figure 39b, d, f), where the wind directions of the background and observed vortices are opposite, leading to significantly lower wind speeds at the eyewall in the analysis wind

doi:10.6342/NTU202403267

field (Figure 40b, d, f). Therefore, while the VRP experiment can correct the vortex position in the analysis field, it introduces asymmetry in the vortex.

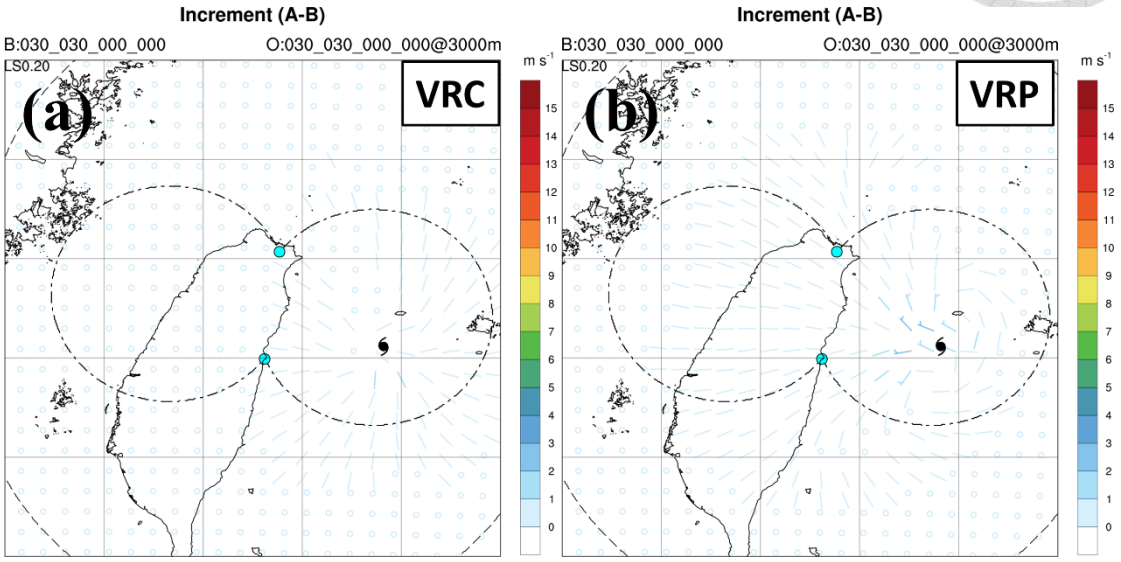

Figure 38. Increment from data assimilation of Doppler velocity from simulated RCWF and RCHL radars in the rotational flow ideal experiment, processed using (a) VRC and (b) VRP methods. The black dashed and dotted-dashed lines are the same as in Figure 36.

doi:10.6342/NTU202403267

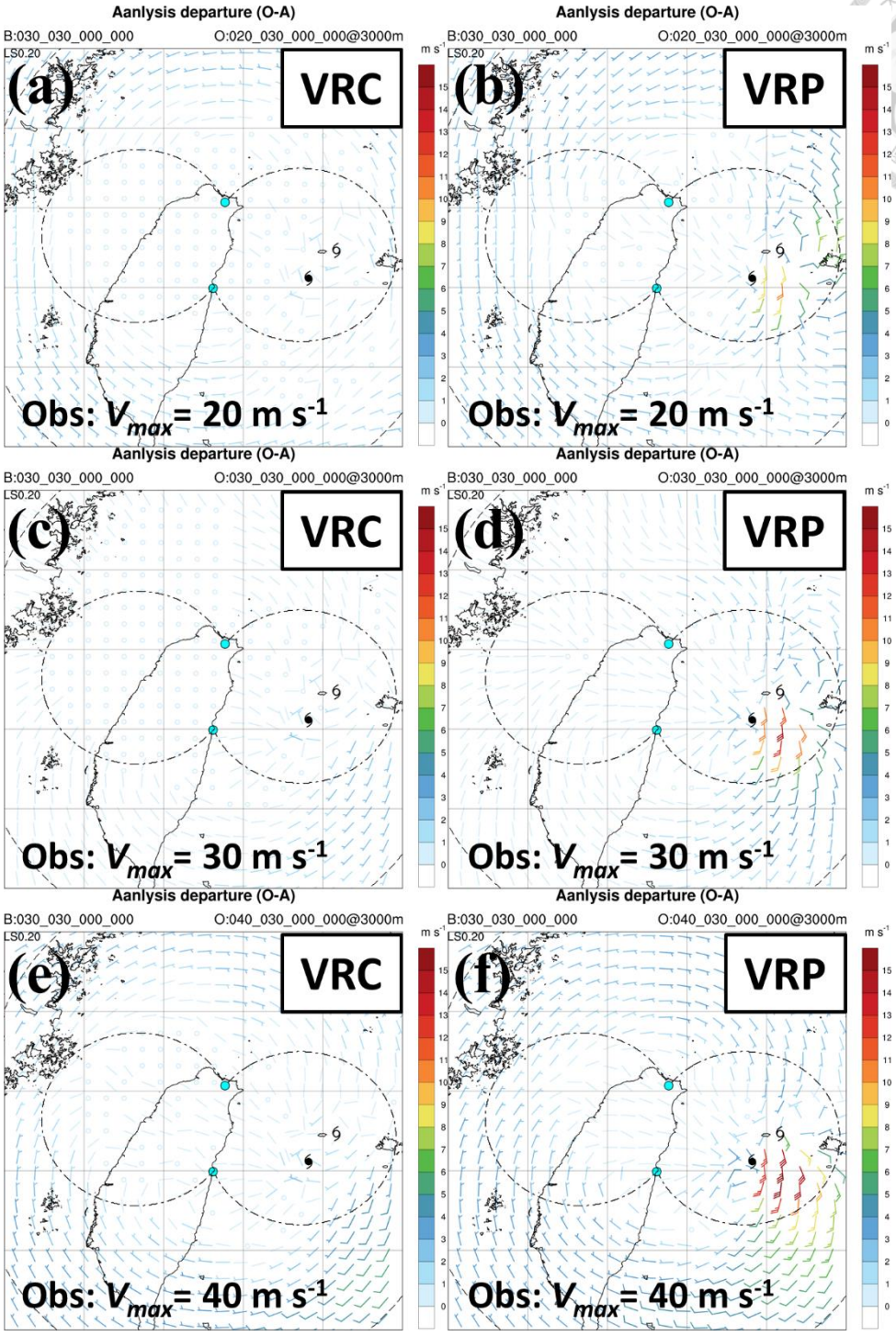

Figure 39. Analysis departure for Doppler velocity fields with observed vortex maximum wind speed of 20 m s^{-1}, processed using (a) VRC and (b) VRP methods. Panels (c)-(d) and (e)-(f) show the analysis departure for observed maximum wind speeds of 30 m s^{-1} and 40 m s^{-1}, respectively. The black dashed and dotted-dashed lines are the same as in Figure 36.

doi:10.6342/NTU202403267

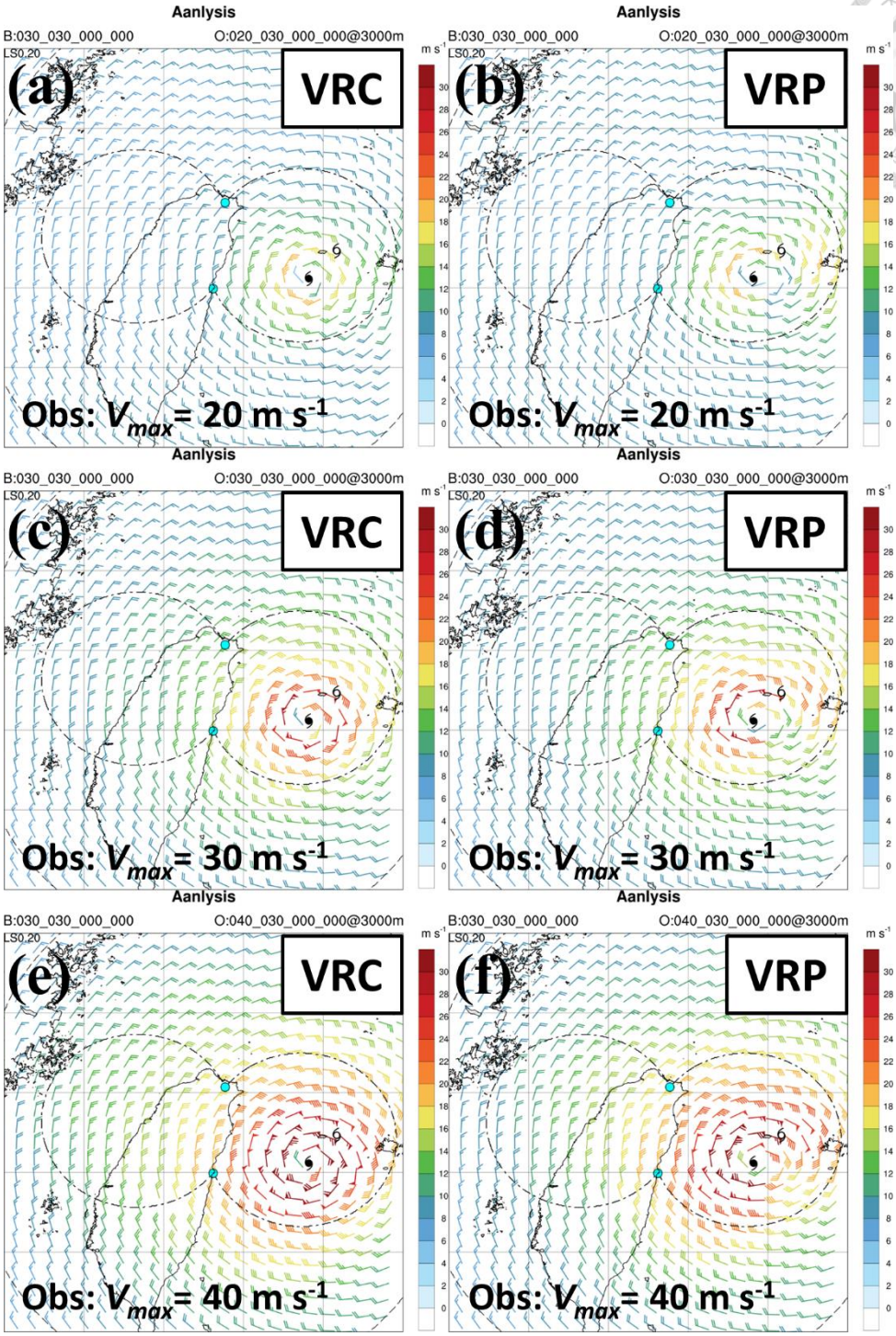

Figure 40. Same as Figure 39, but for the analysis after data assimilation.

doi:10.6342/NTU202403267

4.3. Simulation validation

The results of the idealized case tests indicate that interpolating radar wind field data onto model grid points (VRC) exerts a stronger influence beyond 120 km from the radar. In areas covered by dual radars, this method more effectively adjusts the typhoon center and structure compared to the data thinning method (VRP). This section compares the simulation results of VRC, VRP, and the absence of radar radial wind field assimilation (NOVR) to understand the impact of data preprocessing methods on the numerical model's simulation of typhoon intensity evolution.

The track validation, as shown in Figure 41, indicates that the initial vortex center in the VRC experiment is the closest to the TCET center, with an error of only 11 km, followed by VRP with an error of 22 km. The NOVR experiment exhibits the largest deviation, with a difference of 59 km. In the subsequent simulations, VRC and VRP show minimal path differences before 0000 UTC on Sep 12, with an error of approximately 28 km. Observational data then show the typhoon moving closer to the terrain, a characteristic captured by both simulations; however, the VRC vortex exhibits a larger shift towards the terrain. The vortex in the NOVR experiment, due to its initial position being farther southwest, moves predominantly north–northeast, deviating significantly from the observed northward path until after 0300 UTC on Sep 12, when the movement trend aligns more closely with observational data. The overall track

doi:10.6342/NTU202403267

errors during the analysis period for the VRC, VRP, and NOVR experiments are 32 km, 29 km, and 74 km, respectively.

Figure 42 shows the intensity changes at 1-3 km altitude from the three simulations and their comparison with the radar-retrieved maximum tangential wind (GBVTD). The results indicate that the intensities from all three experiments are lower than the radar-retrieved maximum tangential wind field after 1600 UTC, particularly at 2-3 km altitude, where the maximum difference exceeds 10 m s^{-1}. This suggests that the model exhibits a higher vertical decay gradient in eyewall wind speed compared to observational data. At 1 km altitude, the VRC experiment's simulated typhoon intensity change trend is most consistent with the observed intensity at 3 km altitude, showing an increase of about 15 m s^{-1} within 12 hours, with the maximum intensity occurring at 0000 UTC on Sep 12 (Figure 42a). The VRP experiment follows, with an increase of approximately 10 m s^{-1}, with the maximum intensity occurring at 1800 UTC on Sep 11 (Figure 42b). The NOVR experiment shows no significant intensifiying or weakening trend, fluctuating only between 55 and 60 m s^{-1} (Figure 42c).

Regarding the RMW, the initial state for VRC is approximately 18 km, with major contraction occurring between 1600 UTC on Sep 11 and 0000 UTC on Sep 12, reaching a minimum of about 14 km (Figure 42a). For VRP, the initial state is around 20 km, with major contraction from 1000 to 1600 UTC on Sep 11, thereafter maintaining

doi:10.6342/NTU202403267

around 14 km (Figure 42b). The NOVR experiment shows the largest RMW values, initially around 36 km, continually contracting during the analyzed period to a minimum of about 22 km (Figure 42c). Among the three methods, the VRC experiment's intensity changes and RMW variations are the most consistent with radar observations.

The comparison of the average tangential wind field structure within a 60 km radius reveals that both the VRC and VRP experiments successfully capture the robust wind field structure of Typhoon Chanthu. The highest radial decay rate of the tangential wind from RMW to 3×RMW reaches approximately 0.8-0.9 m s^{-1} km^{-1} (Figures 43a, b). In contrast, the NOVR experiment exhibits a decay rate of about 0.6 m s^{-1} km^{-1} (Figure 43c), indicating that radar data assimilation not only improves the simulated intensity but also enhances the representation of the typhoon's radial wind field variation.

This study uses the GBVTD-retrieved tangential wind field as the validation truth, calculating the root mean square error (RMSE) as a quantitative measure of validation results using Equation (12):

$$RMSE = \sqrt{\frac{\sum(vt_{model} - vt_{obs})^2}{N}} \qquad (12)$$

where vt_{model} and vt_{obs} represent the tangential wind fields from the model and observations, respectively. At a 1 km altitude, although the VRC experiment's simulated vortex intensity change trend aligns more closely with the observations, its slightly

doi:10.6342/NTU202403267

larger RMW compared to the observations results in an overall RMSE that is about 1-3 m s^{-1} higher than that of the VRP experiment as the simulation time progresses. The NOVR experiment shows significantly larger structural differences in the simulated vortex, with overall RMSE values exceeding 12 m s^{-1} and peaking above 20 m s^{-1}, approximately double those of the VRC and VRP experiments.

In addition to the wind field structure, the evolution of eyewall convection is a primary focus of this study. Considering the model resolution of 1 km, the analysis includes the RMW ± 5 km range to calculate the average reflectivity. The results indicate that the eyewall convection in the VRC, VRP, and NOVR experiments displays a wavenumber-1 asymmetry, consistent with observations. This asymmetry is characterized by stronger convection predominantly on the eastern side of the vortex before 1900 UTC on Sep 11. After 1900 UTC, the asymmetry shifts primarily to the north-northeast quadrant. Among the three experiments, the evolution of eyewall asymmetry in the NOVR experiment most closely matches the observations (Figure 44).

The direction of eyewall asymmetry is highly correlated with the VWS direction experienced by the typhoon. Therefore, this study also calculates the average wind speed at various heights within a 30 to 60 km annular region around the simulated vortex center to represent the meso-beta scale mean flow. The results show that in the VRC experiment, the 2-8 km VWS trend closely resembles the observations, with

doi:10.6342/NTU202403267

values gradually decreasing from about 6 m s^{-1} and remaining below 1 m s^{-1} between 1600 and 1930 UTC on Sep 11, then increasing to over 9 m s^{-1} by 0130 UTC on Sep 12. When separating the shear into lower-level (2-5 km) and upper-level (5-8 km) components, the results indicate that the VWS is primarily contributed by the lower-level shear (Figure 45a). In the VRP experiment, the VWS remains relatively constant at about 3-6 m s^{-1} until 2200 UTC on Sep 11, after which it gradually increases, reaching 9 m s^{-1} by 0200 UTC on Sep 12 (Figure 45b). In contrast, the NOVR experiment shows VWS predominantly above 9 m s^{-1}, with a brief decrease to around 5 m s^{-1} between 1800 and 2100 UTC on Sep 11 (Figure 45c).

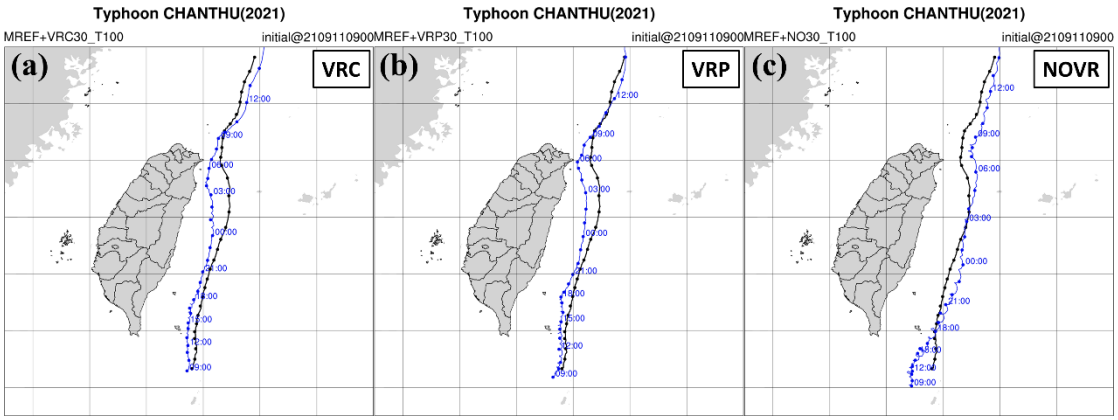

Figure 41. Simulated tracks (blue solid line) of Typhoon Chanthu from the initial time of 0900 UTC on Sep 11 for 30 hours of (a) VRC, (b) VRP, and (c) NOVR experiments. The black solid line represents the TCET observed typhoon track. Blue (black) solid dots indicate the hourly simulated (observed) typhoon center positions, with corresponding UTC times labeled.

doi:10.6342/NTU202403267

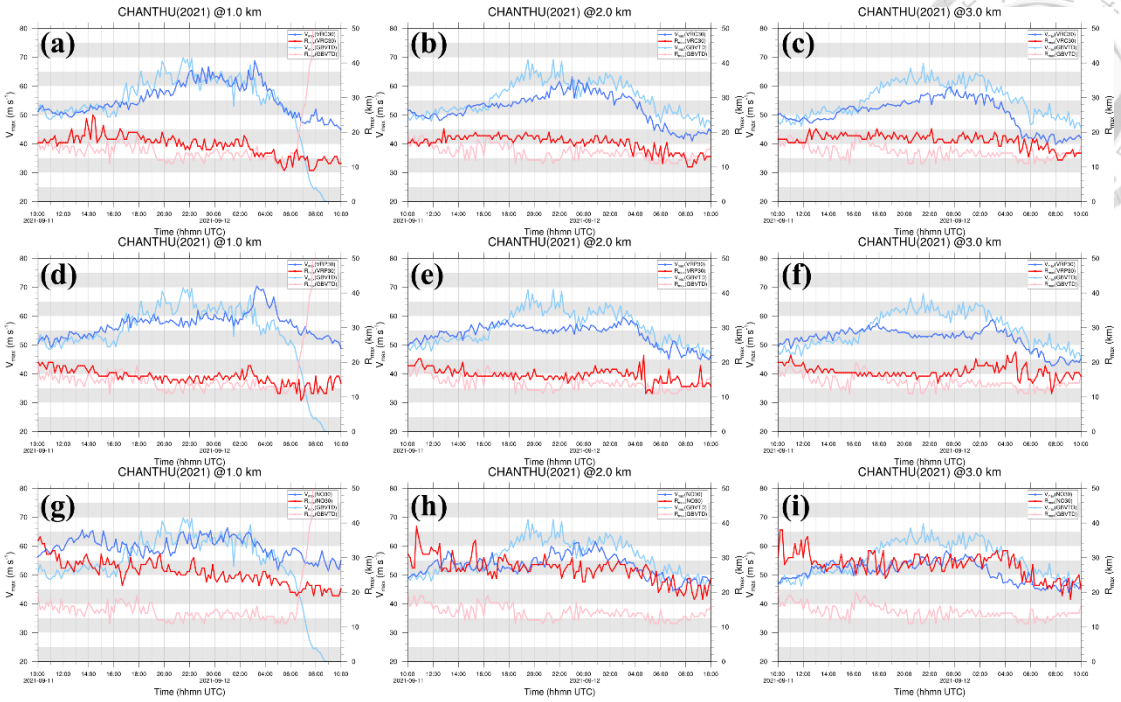

Figure 42. Maximum wind speed (blue solid line) and RMW (red solid line) at (a) 1 km, (b) 2 km, and (c) 3 km heights in the VRC experiment. The maximum wind speed and RMW from GBVTD are shown as light blue and pink solid lines, respectively. Panels (d) to (f) and (g) to (i) show the results of VRP and NOVR experiments, respectively. The left ordinate represents wind speed, the right ordinate represents the radius from the typhoon center, and the abscissa represents time, covering the period from 1000 UTC on Sep 11 to 1000 UTC on Sep 12.

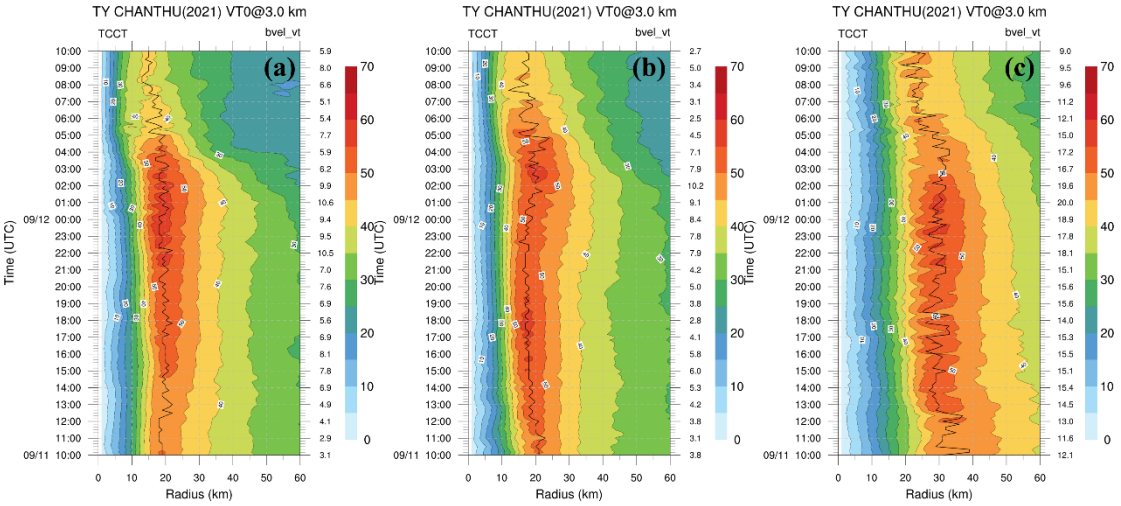

Figure 43. Same as Figure 21a, but for the simulation results of the (a) VRC, (b) VRP, and (c) NOVR experiments.

doi:10.6342/NTU202403267

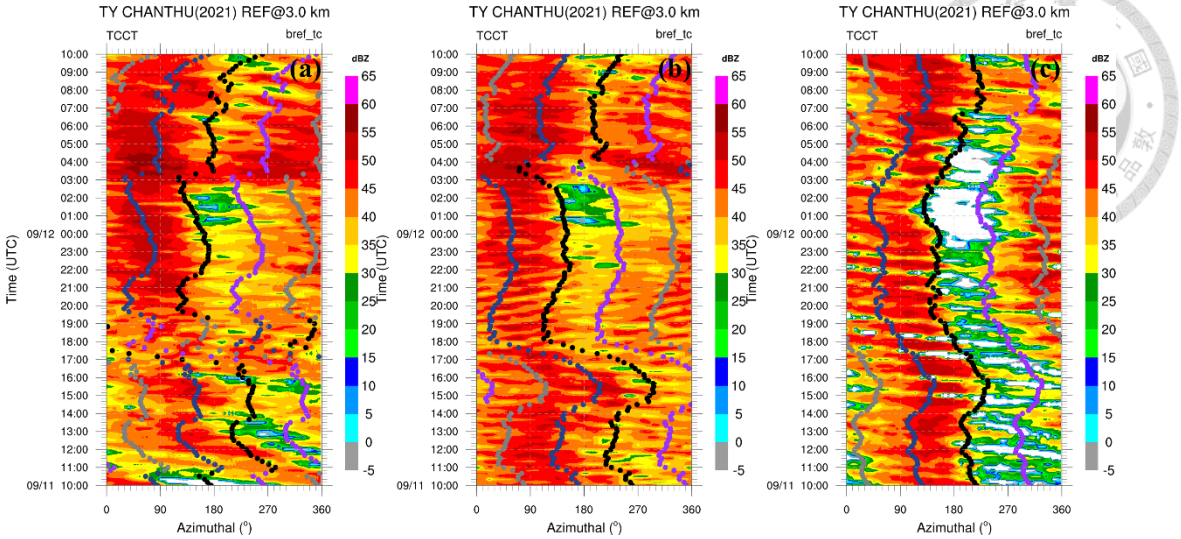

Figure 44. Same as Figure 25a, but for the simulation results of the (a) VRC, (b) VRP, and (c) NOVR experiments.

doi:10.6342/NTU202403267

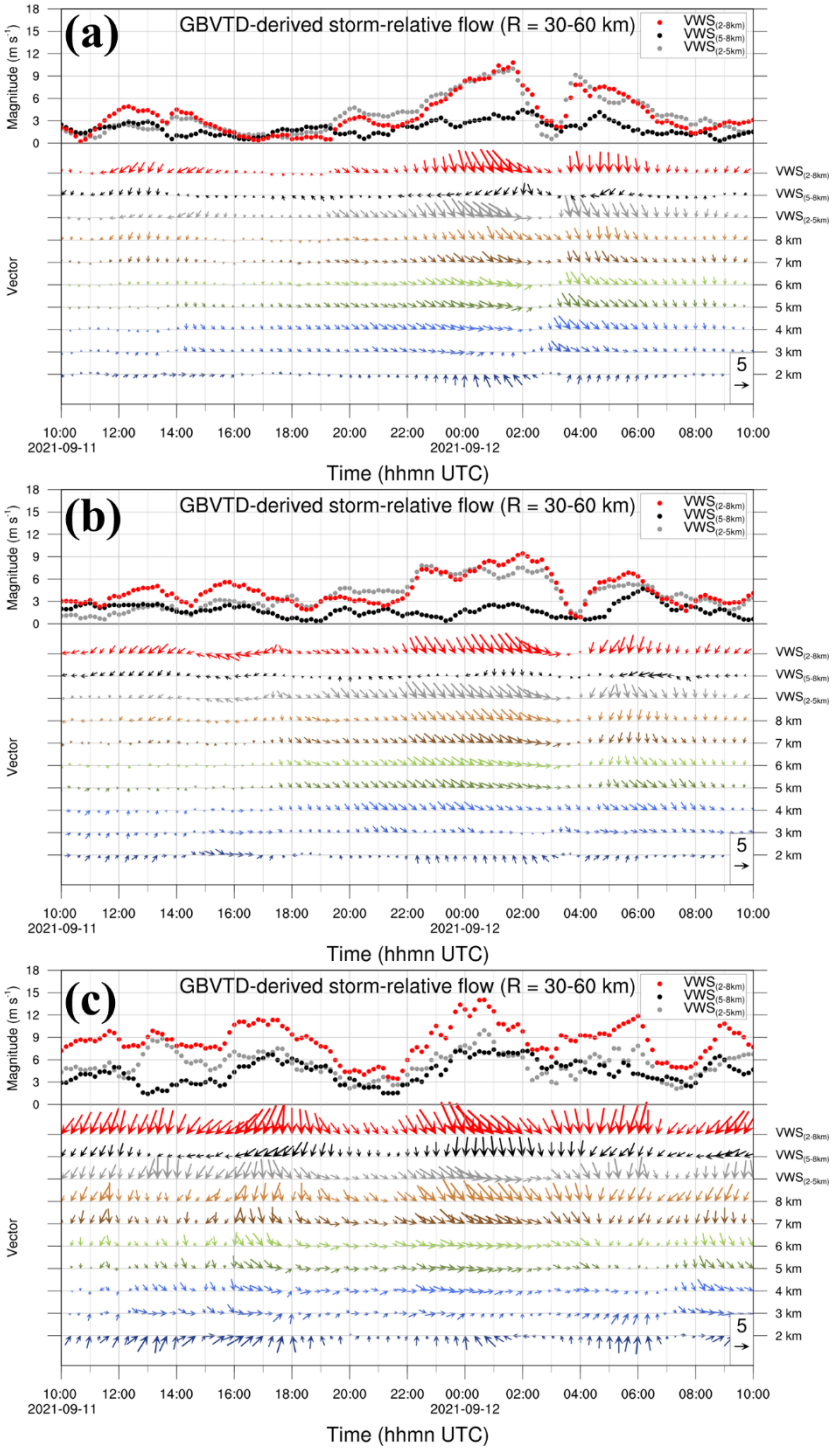

Figure 45. Same as Figure 30a, but for the simulation results of the (a) VRC, (b) VRP, and (c) NOVR experiments.

doi:10.6342/NTU202403267

4.4. Discussion

Based on the observational data analysis in Chapter 3, it is concluded that the intensification of Typhoon Chanthu is related to TDF and the vertical distribution of VWS. The comparison in the previous section shows that the simulated track of the vortex and wind field structure in the VRC and VRP experiments are similar, with VRC showing greater intensification than VRP. However, the VWS simulated in both experiments is less consistent with observations. Therefore, this section will compare the differences between VRC and VRP to explore the potential impact of terrain-induced flow on inner-core convection.

In the VRC experiment simulation, an east–west oriented updraft at 1 km height began to appear in the vicinity of the vortex's eyewall on the southern side at 1400 UTC on Sep 11, forming an inner rainband (Figure 46). This inner rainband was subsequently advected by the vortex's primary circulation, gradually merging with the eyewall. This phenomenon persisted until 0000 UTC on Sep 12, indicating that the TDF can cause convergence with the primary circulation of the vortex on the southern or southeastern side. This convergence formed the inner rainband, which was eventually advected into the eyewall region by the vortex's primary circulation (Figure 46).

In contrast, the VRP simulation exhibited a different phenomenon. The region of upward motion induced by TDF in the southeastern quadrant of the vortex occurred at a

doi:10.6342/NTU202403267

radius approximately 10 km outside the eyewall at 1 km height. This phenomenon lasted for about three hours (1200-1500 UTC on Sep 11; Figure 47). Subsequently, the location of this updraft remained about 10 km outside the eyewall, but similar to the VRC experiment, it gradually merged into the eyewall through advection by the primary circulation. Although the patterns of updraft caused by TDF and primary circulation convergence differed between the two experiments, both simulations showed a steady intensification of the vortex before 1800 UTC on Sep 11, with the vortex in the VRP experiment intensifying at a faster rate (Figure 42).

The idealized experiments by Wang and Tan (2020) with initially smaller outer-core wind speeds show that when inflow is generated in the boundary layer, the updrafts are triggered at radii closer to the inner-core region. These updrafts are then advected by the typhoon's primary circulation, gradually merging into the eyewall. The locations of boundary layer updrafts in this process are similar to the results of the VRC simulation in the southeastern quadrant. In contrast, the VRP simulation results resemble those of Wang and Tan (2020) with initially larger outer-core wind speeds, where the updraft region occurs at a certain distance outside the eyewall. Wang and Tan (2020) indicate that the maximum wind speed of the eyewall increases in both scenarios. When the updraft region occurs at a radius further from the primary eyewall, it is more conducive to the formation of a secondary eyewall. Conversely, if it occurs closer to the

doi:10.6342/NTU202403267

primary eyewall, the convection gradually merges into the primary eyewall, resulting in a thicker primary eyewall.

The comparison of surface heat flux differences between VRC and VRP shows that both sensible heat flux and latent heat flux are higher in the VRC experiment (Figure 48). This indicates that downdrafts induced by VWS on the upshear side can gain more energy from the higher surface heat flux when the air parcels reach the boundary layer. These air parcels are then advected by the primary circulation into the inner-core region over the UL quadrant, mitigating the downdraft pathway of the ventilation effect that causes vortex weakening. However, the VWS in the VRC experiment is weaker than in the VRP experiment during the vortex intensification period (Figure 45a), suggesting that the intensification of the vortex in the VRC simulation may be more related to the low VWS environment. In contrast, the intensification process in the VRP experiment is more complex, influenced not only by environmental wind shear but also by the internal dynamics of the eyewall, such as polygonal eyewall structures, which were dominated by a wavenumber-3 structure between Sep 11, 1700 and 2300 UTC (Figure 49b).

This section compares the two different assimilation methods, VRC and VRP, to explore the impact of TDF on intensity changes. While the initial wind field structures of both methods are qualitatively similar, their simulated vortex development shows significant differences. The updraft region induced by TDF in the VRC experiment is

doi:10.6342/NTU202403267

located near the eyewall region, whereas in the VRP experiment, it occurs at a radius approximately 10 km outside the eyewall. Before 1800 UTC on Sep 11, the vortex in the VRP experiment intensifies more rapidly. However, after 1800 UTC, due to the highly asymmetric convection in the eyewall, primarily exhibiting a wavenumber-3 structure, the vortex intensity does not show significant changes (Figure 49b). By comparison, the VRC experiment features weaker environmental VWS (Figure 45a) and higher vortex axisymmetry (Figure 49a). Although the intensification before 1800 UTC is less than that in the VRP experiment, the vortex continues to intensify until 0000 UTC on Sep 12.

The impact of TDF and eyewall dynamics simulated in the VRC and VRP experiments reveals significant differences, indicating that the intensification process may be sensitive to initial conditions. Additionally, the simulated environmental VWS in both experiments does not align with observations, making it challenging to use these simulations to support the mechanisms inferred from observational data regarding the intensification of Typhoon Chanthu. To address these issues, increasing the horizontal resolution is recommended to capture more features forced by meso-β scale processes. Furthermore, as the terrain-induced forcing primarily affects the lower layer, increasing the number of vertical layers in the low level may also benefit the performance of the simulations. Both VRC and VRP assimilation experiments suggest that the

doi:10.6342/NTU202403267

intensification process may involve the interaction of multiple factors, making it difficult to comprehensively analyze with a single simulation. Future studies are recommended to employ ensemble simulations to categorize potential intensification pathways and clarify the specific pathway of Typhoon Chanthu's intensification process.

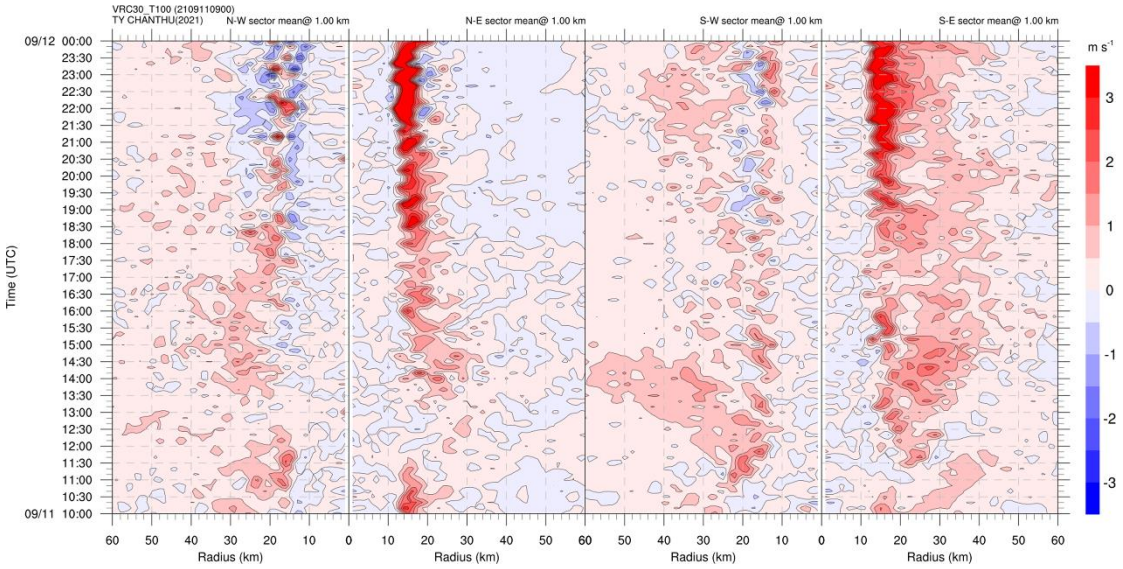

Figure 46. Simulated 1 km height vertical velocity in the VRC experiment, showing the quadrant-averaged regions from left to right: northwest, northeast, southwest, and southeast.

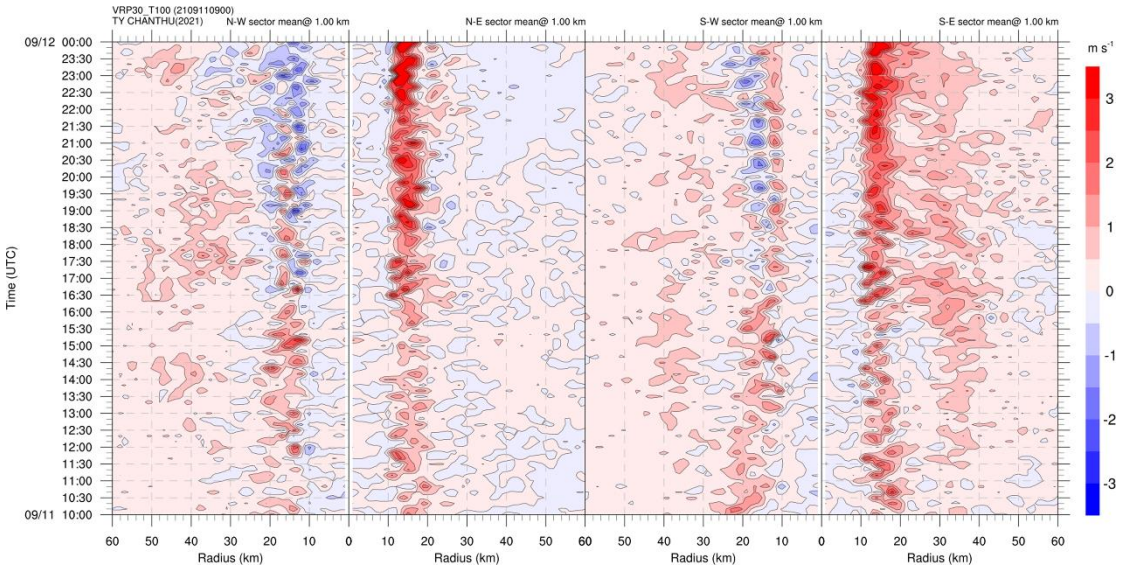

Figure 47. Same as Figure 46, but for the simulation results of the VRP experiment.

doi:10.6342/NTU202403267

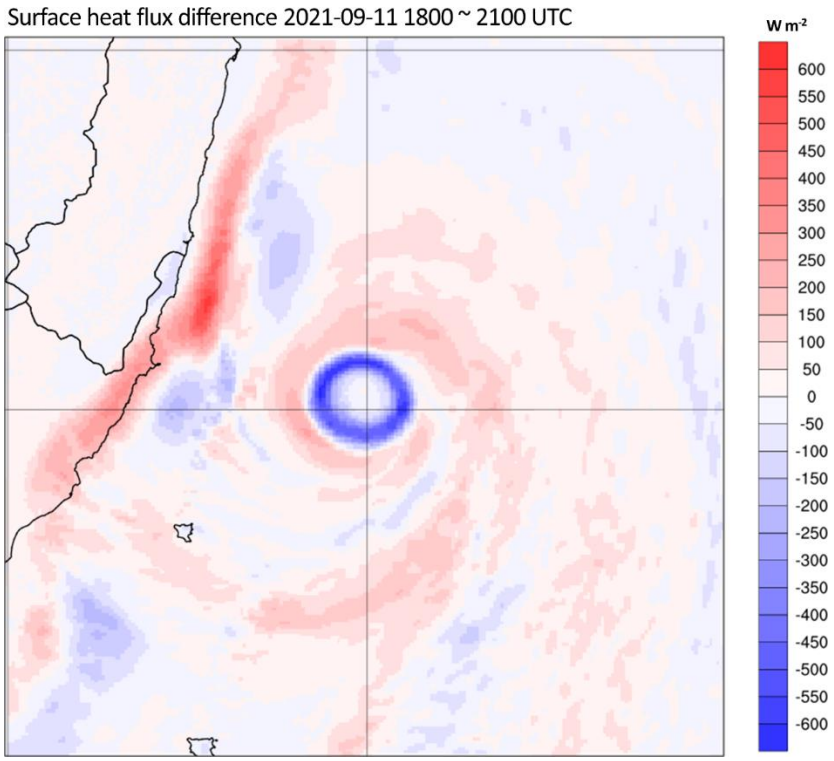

Figure 48. Difference in 3-hour averaged (1800 to 2100 UTC on Sep 11) surface heat flux (W m^{-2}) between the VRC and VRP experiments.

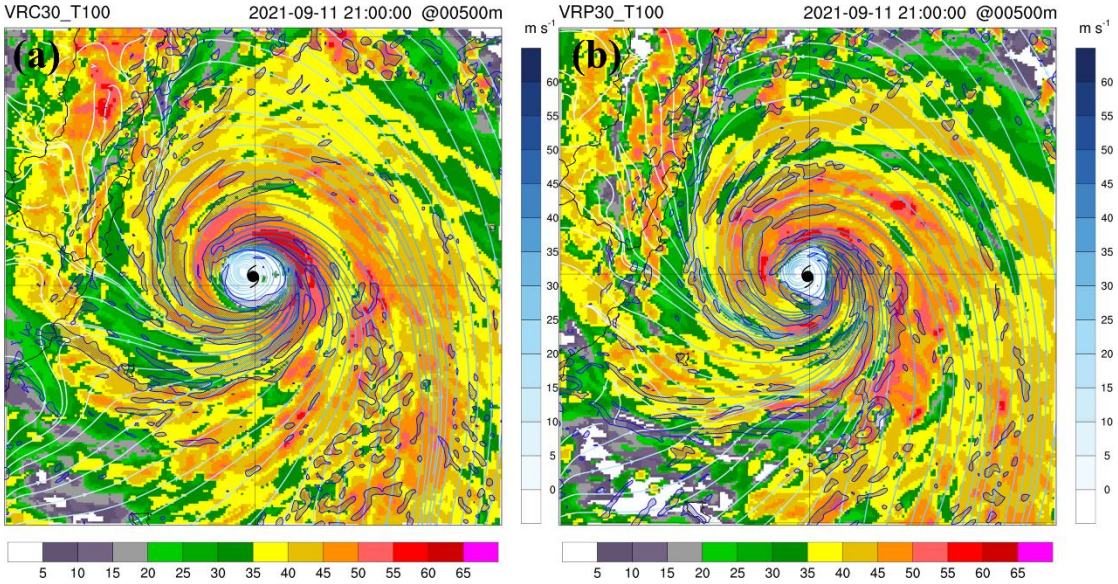

Figure 49. Simulated results at 2100 UTC on Sep 11 for the (a) VRC and (b) VRP experiments. Color shading represents the maximum reflectivity, overlaid with 10 m near-surface streamlines. The blue color scale represents wind speed. The mesh area with a blue boundary indicates regions at 500 m height with vertical velocities greater than 0.5 m s^{-1}.

doi:10.6342/NTU202403267

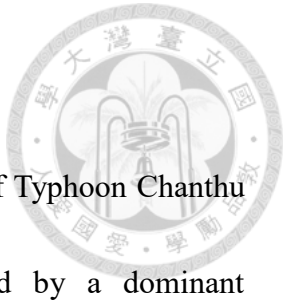

5. Conclusions and future work

The dense radar network observed the notable intensification of Typhoon Chanthu as it tracked along the eastern coast of Taiwan, characterized by a dominant wavenumber-1 asymmetry in the eyewall convection. This study aims to investigate the impacts of terrain-induced flows on the rapid intensification of Typhoon Chanthu. The first part of this study proposes a vortex-based dealiasing algorithm called VDVD with inner-outer iterative procedures to ensure the quality of Doppler velocity data for typhoon studies. The second part involves an observational analysis of Typhoon Chanthu, utilizing data from ground-based radar and weather stations. The third part of this study conducts numerical model simulations with radar data assimilation to investigate the impact of TDF.

To evaluate the performance of the VDVD algorithm, the Doppler velocity from Typhoon Fitow (2013) and Typhoon Nesat (2017) were used. The performance of the VDVD and ZW06 is summaried below:

1) The VDVD algorithm recovered most of the aliased velocity observations with 99.4% accuracy across all pixels, based on 472 elevation sweeps of Fitow.
2) The success rate of the VDVD algorithm for each sweep ranges from 93.6% to 100%, while the ZW06 algorithm's success rate ranges from 74.5% to 99.97%.
3) The unsuccessful pixels of the VDVD algorithm are primarily due to the influence

doi:10.6342/NTU202403267

of sea clutter, which is often embedded within weather echoes and reduces the success rate.

4) In the case study of Typhoon Nesat (2017), the VDVD algorithm was able to recover most aliased Doppler velocities, except for those in terrain-induced local circulation areas outside the inner core region of the TCs.

5) For this special condition, a radial-by-radial verification procedure was appended to the VDVD algorithm to recover inadequately dealiased Doppler velocities.

Overall, the VDVD algorithm significantly enhances the quality of Doppler velocity data for TCs, thereby improving the reliability of subsequent analyses. Consequently, it was utilized for the Doppler velocity of Typhoon Chanthu to ensure data quality and facilitate further analysis.

The main themes in this study are the roles of VWS and the interactions between the terrain-induced flow and the primary circulation of the TC, which are crucial for the inner-core evolution and intensification of TCs near Taiwan's terrain. By analyzing radar reflectivity and Doppler velocity data from multiple radars, along with weather station measurements, the study investigated the temporal evolution of the TC’s inner core structure and its connection to the mean flow characteristics. The GBVTD method was employed to derive the TC’s circulation and investigate its kinematic features with a high temporal resolution of 10 minutes. The application of the GBVTD algorithm was utilized

doi:10.6342/NTU202403267

to estimate the meso-β scale mean flow of the TC with a higher temporal resolution compared to that derived from the ERA5 data.

The horizontal wind speed of Chanthu at an altitude of 3 km increased rapidly by approximately 18 m s^{-1} within an 11-hour period, indicating RI. At the peak of intensifying stage, the maximum wind speed exceeded 65 m s^{-1}, with an RMW of only 12 km. Subsequently, the typhoon experienced RW, with the maximum wind speed at 3 km altitude decreasing by approximately 19 m s^{-1} within 8 hours. Remarkably, Typhoon Chanthu underwent both RI and RW within a short 24-hour period, presenting significant challenges for accurate intensity forecasting and timely warning issuance.

During the intensifying stages, a significant rotation of the eyewall convection maximum in Typhoon Chanthu occurred, transitioning cyclonically from the eastern to the northern semicircle at 1600 UTC on Sep 11, coinciding with the completion of an apparent ERC. Simultaneously, the terrain-induced west-southwestly boundary inflow from the south of the TC was initiated. Additionally, it was observed that the LMF rotated from southwesterly to southeasterly. Both modifications in the flows are suggested to be influenced by the terrain.

The analysis of mean flow reveals that the meso-β scale VWS derived from the GBVTD can effectively capture the abrupt changes induced by the terrain and is consistent with the observed eyewall convection asymmetry. In contrast, the meso-α scale

doi:10.6342/NTU202403267

VWS derived from the ERA5 shows only minor directional changes throughout the analyzed period, resulting in the maximum reflectivity being located on the upshear side. This discrepancy is inconsistent with the documented location of shear-induced convection asymmetry in TC eyewalls in previous studies. These findings suggest that radar-derived meso-β mean flow can provide accurate VWS information that reflects the actual conditions experienced by the TC when it is in close proximity to the Taiwan terrain, while the applicability of ERA5-derived meso-α scale VWS may be limited in such cases.

Based on the analyses conducted in this study, the factors that possibly contributed to the intensification of Typhoon Chanthu are summarized in Figure 50 and itemized as follows:

1) Terrain-induced boundary inflow south of the TC:

   The significant change in wind direction observed at the Lan-yu station suggests that the flow was influenced by terrain. The terrain-induced boundary inflow and the primary circulation of the TC may potentially converge in the southeastern quadrant of the TC's eyewall within the boundary layer, subsequently enhancing the convection on the downshear side of the TC.

2) UL-pointing low-level flow:

   The vertical profile of the meso-β scale mean flow indicates that the low-level flow

doi:10.6342/NTU202403267

was directed UL during stages II and III. Previous studies by Rappin and Nolan (2012) and Lee et al. (2021) suggested that when the directions of VWS and low-level flow were counteraligned, surface heat fluxes can be enhanced on the downshear side. These enhanced surface heat fluxes were hypothesized to play an important role in recovering the moist static energy of shear-enhanced downdrafts within the boundary layer over the inflow area, preventing the TC eyewall from entraining low-energy air parcels. The maintenance of the convection in the UL quadrant can consequently enhance the axisymmetric heating that benefits subsequent intensification.

3) Weak upper-level VWS:

The vertical profile of the mean flow also indicates that the magnitude of the upper-level VWS was close to zero during stages II and III. Fu et al. (2019) noted that stronger upper-level VWS hampers TC intensification by weakening the warm core through the radial ventilation pathway in the middle-upper troposphere. Therefore, the low magnitude of the upper-level VWS provided a favorable environment for the intensification of Typhoon Chanthu.

An intriguing point worth highlighting is that Chanthu underwent an ERC concurrently during the RI process between stages I and II. Following the completion of the ERC, more favorable internal and external conditions for subsequent intensification became evident. In the minor intensification stage (e.g., stage I), as Typhoon Chanthu

doi:10.6342/NTU202403267

underwent ERC, the meso-β scale VWS between 2 to 5 km decreased to values under 2 m s^{-1} (Figure 30). Simultaneously, eyewall asymmetry also reduced during this stage (Figure 25). It was found that the VWS magnitude approached zero (Figure 30), and axisymmetry significantly increased right after the ERC, establishing enhanced internal and external conditions for subsequent intensification. Furthermore, favorable external conditions, such as boundary-layer inflow triggered by the proposed TDF (Figure 27) and a VWS pattern promoting TC intensification, emerged after 1600 UTC. These combined internal and external factors provided an opportunity for Chanthu to intensify by approximately 12 m s^{-1} within only 5 hours during stage II (e.g., the major intensification stage).

The distinctive nature of the ERC event, as elaborated in section 3.3, is a collective characteristic observed in both Typhoon Chanthu (2021) and Hurricane Irma (2017) during their respective RI processes. Chanthu's ERC, characterized by the merging of the secondary eyewall with the primary eyewall rather than complete replacement, shares similarities with the second ERC event of Irma, as documented by Fischer et al. (2020). However, Torgerson et al. (2023a) termed this phenomenon a "short-term intensity fluctuation" rather than a complete ERC (see their Fig.14 for the proposed schematic diagram). The inner-core convection evolution of this intensity fluctuation exhibited a period of less than 6 hours, having a lesser impact on the primary eyewall and allowing

doi:10.6342/NTU202403267

for immediate subsequent intensification. Torgerson et al. (2023a, b) provided an alternative perspective to examine the significance of the ERC (or intensity fluctuation) toward the RI in Chanthu.

The primary objective of the final part of this study is to examine two radar data assimilation strategies and propose the most effective method for properly initializing an extremely compact TC vortex like Chanthu in numerical models. The VRC experiment employs data assimilation of Doppler velocity fields interpolated onto model Cartesian coordinate. The results indicate that the simulated updraft region induced by TDF in the VRC experiment is located near the eyewall region in the southeastern quadrant. Conversely, the VRP experiment, which assimilates thinned radar data in the radar's original coordinates, shows an updraft region occurring approximately 10 to 20 km outside the eyewall in the southeastern quadrant. The NOVR experiment, which does not assimilate Doppler velocity fields, produces significantly different results compared to the VRC and VRP experiments. Without the benefit of Doppler velocity assimilation, the NOVR experiment shows a less accurate simulation of Typhoon Chanthu's intensification and inner-core evolution.

The VRC experiment also features weaker environmental VWS and higher axisymmetry of the vortex, resulting in continuous intensification until 0000 UTC on Sep 12. Before 1800 UTC on Sep 11, the vortex in the VRP experiment intensifies more

doi:10.6342/NTU202403267

rapidly than in the VRC experiment. However, the presence of highly asymmetric convection, primarily with a wavenumber-3 structure, may mitigate the intensification of the vortex after 1800 UTC. It is found that the VRP experiment is influenced not only by environmental wind shear but also by the internal dynamics of the eyewall, leading to a more complex intensification process. The impact of TDF and eyewall dynamics simulated in the VRC and VRP experiments shows significant differences, indicating that the intensification process may be sensitive to initial conditions. Additionally, the simulated environmental VWS in both experiments does not align with observations, complicating the use of these simulations to support the mechanisms inferred from observational data regarding Typhoon Chanthu's intensification. These assimilation experiments suggest that the intensification process may involve the interaction of vortex structure, eyewall dynamics, terrain-influenced flow and VWS, making it difficult to comprehensively analyze with a single simulation.

The observational analyses of this study identify three possible factors that may have contributed to the intensification of Typhoon Chanthu. However, the traditional dual-Doppler wind synthesis method and GBVTD method employed in this study were still limited in providing a comprehensive three-dimensional circulation of Chanthu to offer direct evidence for the aforementioned possible factors. To achieve a more detailed understanding, variational-based multiple-Doppler-radar synthesis techniques (Gao et al.

doi:10.6342/NTU202403267

1999; Chong and Bousquet 2001; Liou and Chang 2009; Potvin et al. 2012) could be employed for retrieving a more comprehensive three-dimensional circulation in the future research. Additionally, a quantitative assessment of the major physical mechanism of Chanthu's intensification lies beyond the scope of this study. The quantitative assessment of the physical processes through which terrain influences the surrounding flow of the typhoon was not fully achieved due to the limitations in the resolution and coverage of the observational analyses and the resolution of the model simulations used in this study. Future enhancements, such as increasing horizontal resolution and the number of vertical layers, are recommended to better capture meso-β scale features.

Chi et al. (2024) demonstrated that the TDF could cause a rightward track deflection as Chanthu approached southeast Taiwan, suggesting the modification of the surrounding flow adjacent to the TC by the Taiwan terrain. Future investigations could involve sensitivity tests using model simulations that vary the height of the Taiwan terrain to verify the effects on TDF (Figure 27) and the pattern of VWS (Figure 24) and their subsequent influence on TC intensity change. Additionally, the timing and intensity of TDF initiation may also play a crucial role in influencing TC intensification. Therefore, it is recommended to employ ensemble simulations to categorize potential intensification pathways and clarify the specific mechanisms of Typhoon Chanthu's intensification process in the future. Those researches can further investigate and clarify the following

doi:10.6342/NTU202403267

aspects:

1) The impacts of terrain effects on changes in storm-scale VWS and eyewall asymmetry.
2) How the ERC (or intensity fluctuations) influenced meso-β scale VWS and the axisymmetry of eyewall convection, contributing to the RI of Typhoon Chanthu as discussed in this study.
3) The behavior of TCs with similar tracks and how these factors influence their intensity and structure.

doi:10.6342/NTU202403267

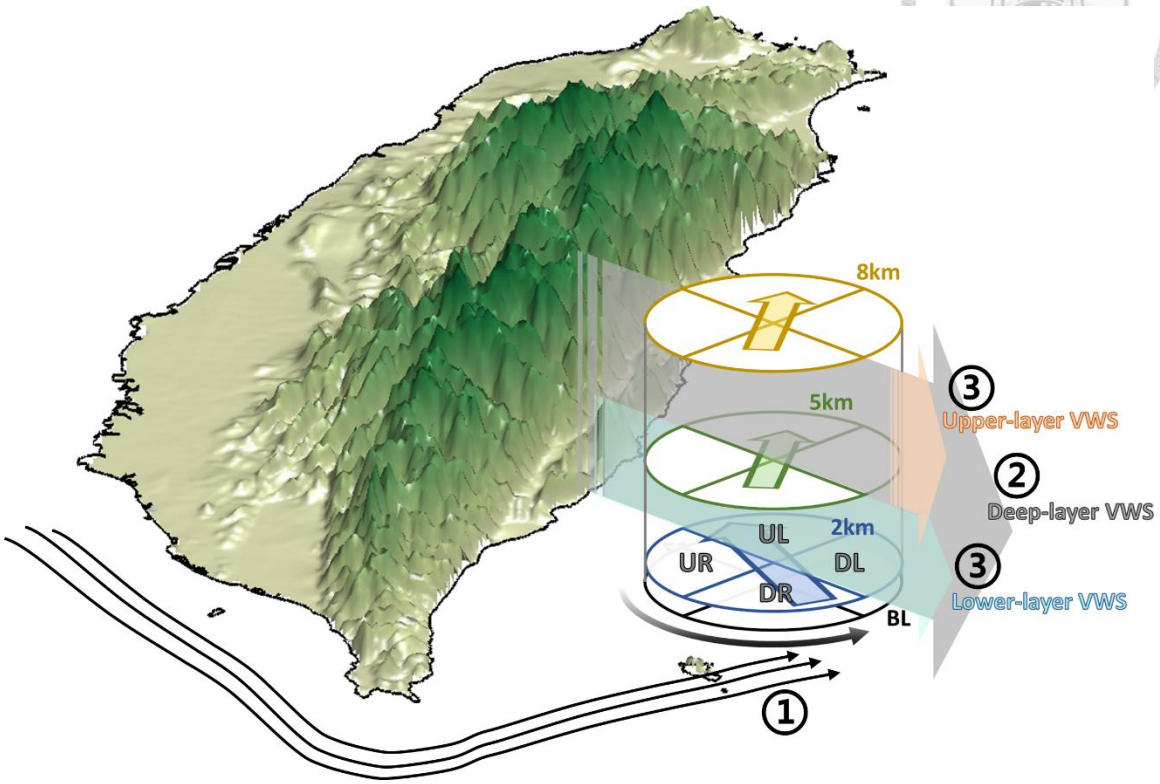

Figure 50. Schematic illustration of the speculated factors prompting the RI of Typhoon Chanthu under the moderate shear environment. The black curved arrow indicates the main flow of the TC. The black thin arrows passing through the southern tip of Taiwan indicate the TDF in the boundary layer. The blue, green and gold horizontal arrows indicate the mean flow at 3, 5 and 8 km, respectively. The gray, cyan and orange arrows vertically intersect the horizontal layers and point towards the southeast, indicate the deep-, lower-, and upper-layer meso-β VWS, respectively. The horizontal length of the arrows represents the magnitude of the VWS. The circle indicates the TC inner-core region, which is separated into DL, UL, UR and DR quadrants under the shear-relative framework.

doi:10.6342/NTU202403267

Appendix

A1. Iterative Surface fitting dealising algorithm

The Iterative Surface Fitting Dealiasing Algorithm (ISFD) developed in this study extends the two-step curve fitting method proposed by Chang et al. (2020) for filtering anomalous Doppler velocity fields. Initially, this two-step method was further developed into the Iterative Curve Fitting Dealiasing Algorithm (ICFD). The concept involves performing a one-dimensional Fast Fourier Transform (FFT) on radar data at a specific radius, followed by applying a low-pass filter with a lower maximum allowable wavenumber to generate a smoother fitted curve. This fitted value serves as a reference wind speed, and data points that deviate excessively from the fitted curve are corrected or filtered out. The adjusted data are then used for the next iteration of curve fitting, gradually increasing the maximum allowable wavenumber of the low-pass filter. This process iteratively adjusts and filters the data until convergence is achieved, completing the quality control for the data at that radius. The same procedure is sequentially applied to the data at each radius until all data are processed.

The following provides a conceptual explanation using a simplified iterative one-dimensional curve fitting method with an idealized case as an example. Figure A1a shows the Doppler velocity field observed by radar, simulated using an ideal Rankine vortex. The vortex is located 150 km southeast of the radar, with a maximum wind

doi:10.6342/NTU202403267

speed of 38 m s^{-1} and a radius of maximum wind of 40 km. The discontinuous region in the eyewall is caused by aliasing issue.

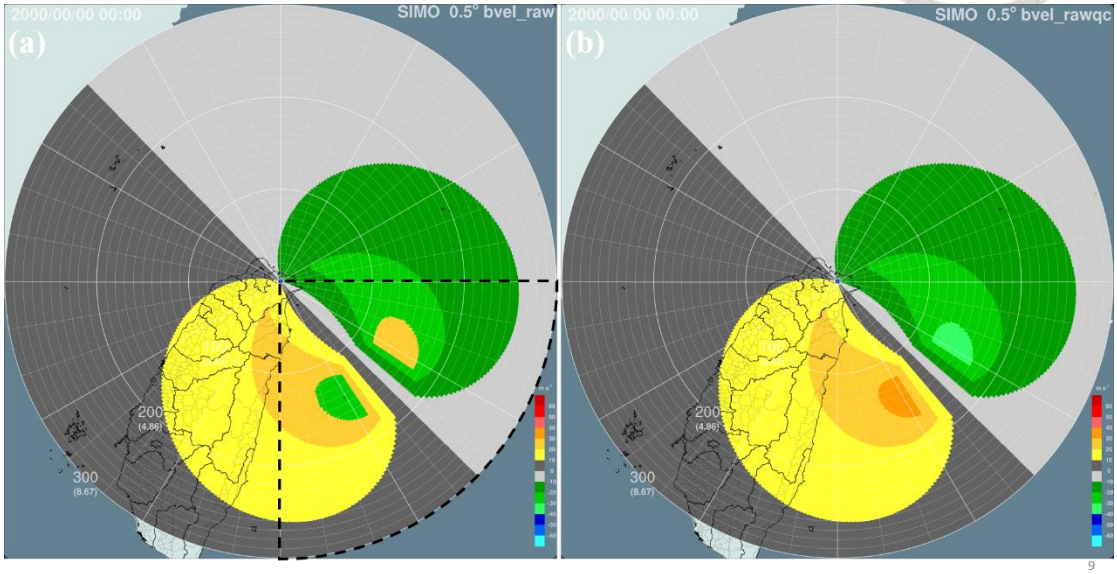

Figure A1: (a) Doppler velocity field observed by radar, simulated using an ideal Rankine vortex, and (b) the result after correction with ICFDA. The vortex is located 150 km southeast of the radar, with a maximum wind speed of 38 m s^{-1} and a radius of maximum wind of 40 km. The black dashed lines indicate the azimuth range (90-180 degrees) shown in Figure A2.

Figure A2 is the processing status of velocity field data at a radius of 150 km from the radar during each iterative step. The steps are as follows:

First iteration (Figure A2a and A2b):

Figure A2a shows the distribution of the original data. Discontinuous data in the azimuth angles of 110-125 degrees and 145-160 degrees indicate aliased data in the eyewall region. The black solid line represents the fitted curve obtained by performing FFT on this data and applying a low-pass filter with a maximum allowable wavenumber

doi:10.6342/NTU202403267

of 3. Data points deviating by more than 2 standard deviations from this reference wind speed are filtered out (red × in red in Figure A2b), completing the first iteration.

Second iteration (Figure A2c and A2d):

The remaining data from the first iteration, with missing data linearly interpolated, undergo FFT again. The reference wind speed for this iteration is the fitted curve obtained by applying a low-pass filter with a maximum allowable wavenumber of 5 (Figure A2c). Stricter criteria (detailed in the text of Figure A4) are applied to filter the data in the second iteration. Figure A2d shows that the corrected data have been recovered to correct values, although some data points are filtered out due to significant differences from the reference wind speed (red × and ⊗, with ⊗ indicating data points that have undergone dealiasing).

Third iteration (Figure A2e and A2f):

The maximum allowable wavenumber is increased to 7, and the steps of the second iteration are repeated. The results show that with the increased maximum allowable wavenumber, the fitted curve aligns more closely with the input data, helping to retain more correct data that might have been incorrectly filtered out in previous steps. (Figure A2e and A2f).

doi:10.6342/NTU202403267

Fourth and fifth iterations (Figure A2g to A2j):

The maximum allowable wavenumber is increased to 10 and 20, respectively, and the steps of the second iteration are repeated. The correct data points are reinstated in both steps (Figure A2g to A2j), and the fifth iteration results are the same as those of the fourth iteration, indicating that the iterative process has converged. The process is completed after the fifth iteration.

Figure. A1b shows the results after applying ICFD to the velocity field data at each radius, demonstrating that this method can recover the local aliased data shown in Figure A1a.

doi:10.6342/NTU202403267

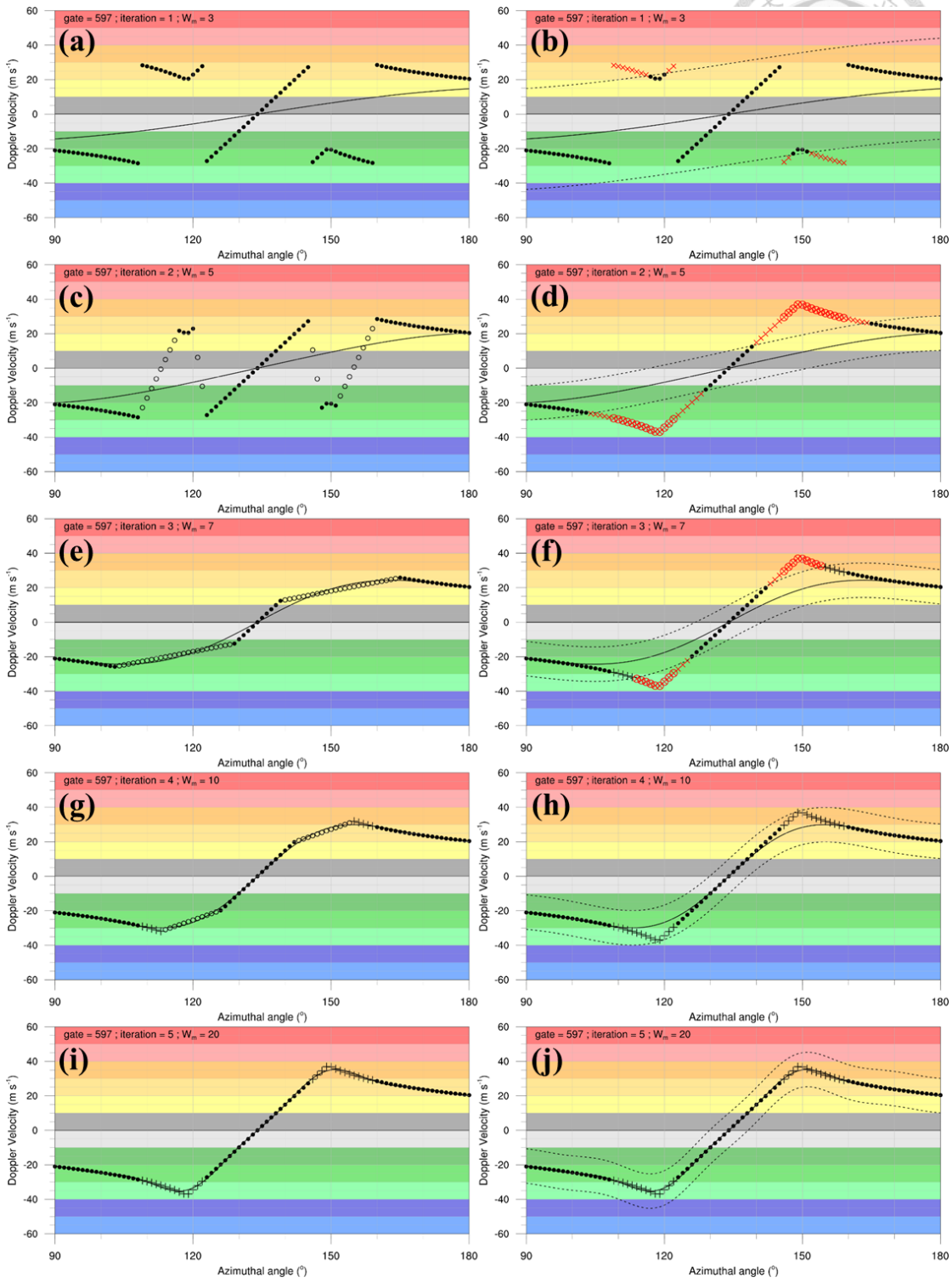

Figure A2: Data as in Figure A1, but for the radius of 150 km from the radar and azimuth angles between 90 and 180 degrees. The ICFDA processing status during the first iteration includes (a) data interpolation, curve fitting, and low-pass filtering, and (b) data filtering. Panels (c) and (d) show the second iteration, (e) and (f) the third iteration, (g) and (h) the fourth iteration, and (i) and (j) the fifth iteration. The color scale corresponds to the wind speed color scale in Figure A3. The black solid line represents the fitted

doi:10.6342/NTU202403267

reference velocity, and the black dashed line indicates the filtering threshold. Black dots and black crosses represent retained data points in each step, with crosses indicating data points that have undergone dealiasing. Black open circles represent interpolated data points. Red crosses and red symbols indicate filtered data points in each step, with symbols indicating data points that have undergone dealiasing.

The principles and concepts of ISFD are the same as those of ICFD, with the main difference being the use of a two-dimensional FFT for surface fitting instead of the original curve fitting to generate reference values for dealiasing. This approach has the advantage of considering variations in both the azimuthal and radial directions simultaneously, thereby simplifying the overall program complexity. When applying one-dimensional or two-dimensional FFT, the data must exhibit periodic characteristics. The spatial distribution of the original radar data shows periodicity in the azimuthal direction (Figure A3a), making it suitable for one-dimensional FFT without additional processing. However, the radial data do not inherently possess periodicity, necessitating additional processing to meet the requirement of periodicity in both dimensions for the application of two-dimensional FFT. To address this, the radar's location can be considered the North Pole, with the direction away from the radar extending towards the Equator. The maximum observational range of the radar is treated as lying exactly on the Equator (Figure A3b). By mirroring the data along the Equator, the radar data can be made to exhibit periodicity in the radial direction as well (Figure A3c).

doi:10.6342/NTU202403267

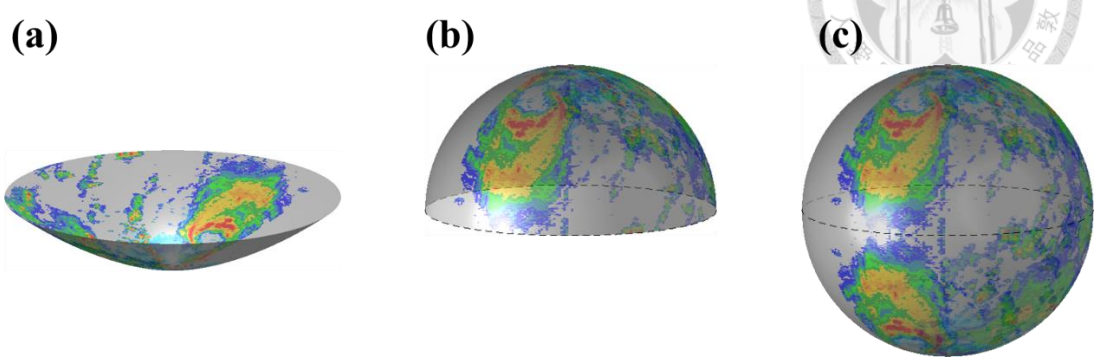

Figure A3: Distribution of radar data in (a) original radar coordinates, (b) hemispherical coordinates, and (c) full spherical coordinates.

The flowchart of the ISFD method is shown in Figure A4. The steps are briefly described as follows:

1) Mirror the original radar data radially with the maximum observational radius as the origin to achieve periodicity in the radial direction.

2) Apply linear interpolation independently in the azimuthal and radial directions to create two sets of interpolated data, which are then averaged to obtain a combined dataset. This averaged dataset is used to replace the invalid data in the original dataset, while the valid data remains unchanged. For efficiency reasons, more advanced interpolation methods were not used.

3) Perform two-dimensional FFT surface fitting and low-pass filtering on the input data (with maximum allowable wavenumbers w_{r_m} in the radial direction and

doi:10.6342/NTU202403267

w_{a_m} in the azimuthal direction). The fitting result serves as the reference value. (Test results show that setting w_{r_m} to a constant 40 and w_{a_m} to one-quarter of the azimuthal wavenumber yields the best accuracy).

4) Use the reference value from step 3 to perform the correction/filtering procedure (dealias the original data and filter out data points with differences exceeding β). In this study, the β value used is 25% of the reference value (hereafter referred to as the proportional value), but not less than 15 m s^{-1} (hereafter referred to as the minimum threshold).

5) Use the corrected data from step 4 as new input data, increase the value of *m* by 1, and return to step 3 until the output data no longer changes or the maximum value of *m* (set to 50 in this study) is reached.

6) Check if the proportion of neighboring grid point differences exceeding 1.5 times the Nyquist velocity is below the threshold ϵ. If not, return to step 1 and reduce the ratio for defining β by 5% and the minimum threshold by 5 m s^{-1}. The ϵ used in this study is 10^{-5}.

Since the mirrored data volume is double that of the original data, the potential impact on execution efficiency is first addressed. Performance testing shows that for the RCWF radar, which has the largest data dimension (1192×2×720, where ×2 indicates

doi:10.6342/NTU202403267

radial mirroring), the execution time for a single iteration is 0.4956 seconds, with data filling taking 0.2169 seconds and the two-dimensional FFT taking 0.2421 seconds. For the RCGI radar, which has the smallest data dimension (800×2×360), the execution time for a single iteration is 0.1201 seconds, with data filling taking 0.0743 seconds and the two-dimensional FFT taking 0.0342 seconds. The average number of iterations required for convergence is typically under 20, and the program is set to a maximum of 50 iterations. Thus, quality control for a single volume scan can usually be completed within a few seconds. Despite the data volume being twice that of ICFD, the simplified processing procedure allows ISFD to achieve comparable overall execution times, and in some cases, even shorter times than ICFD.

In cases where the eyewall data are asymmetric, with valid data only on one side of the eyewall, both VDVD and ICFD fail to effectively correct the aliased Doppler velocities in the eyewall region (Figure A5a, b). However, ISFD can effectively use radial information to recover those aliased data, even when data from the opposite side of the eyewall are missing (Figure A5c).

Overall, ISFD is more effective than ICFD in utilizing radial information to correct erroneous data. This results in 1) more effective noise reduction, 2) fewer errors from radial continuity checks inherent in ICFD, and 3) reduced misinterpretation in areas with large velocity gradients.

doi:10.6342/NTU202403267

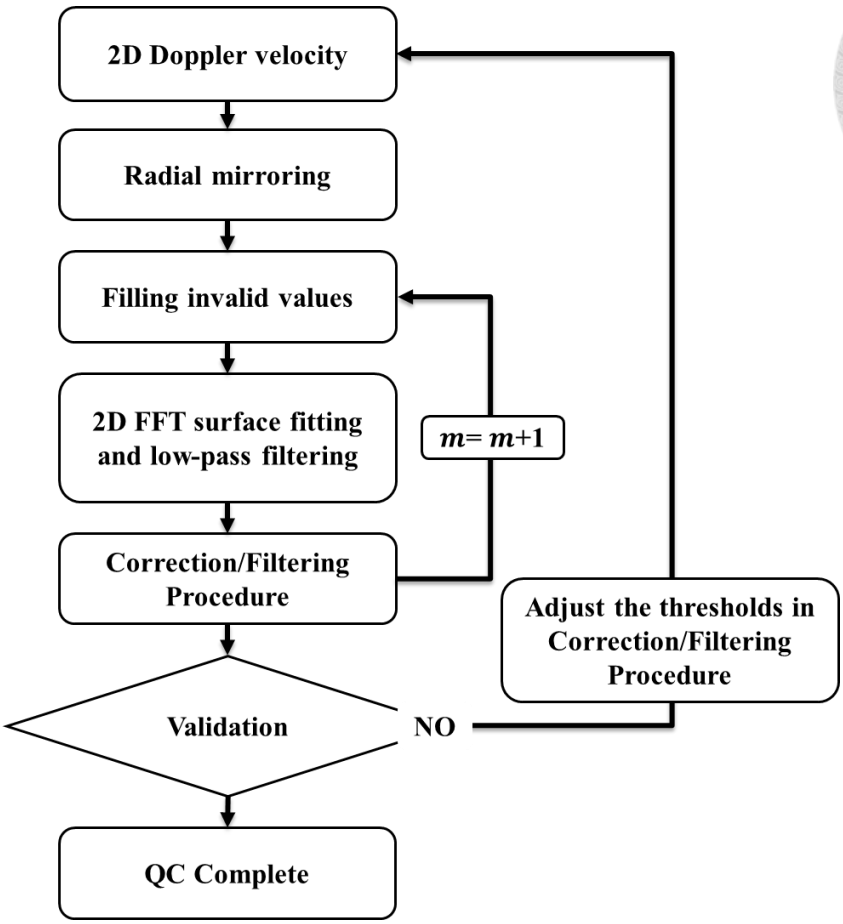

Figure A4: Flowchart of the ISFDA dealiasing and noise filtering algorithm.

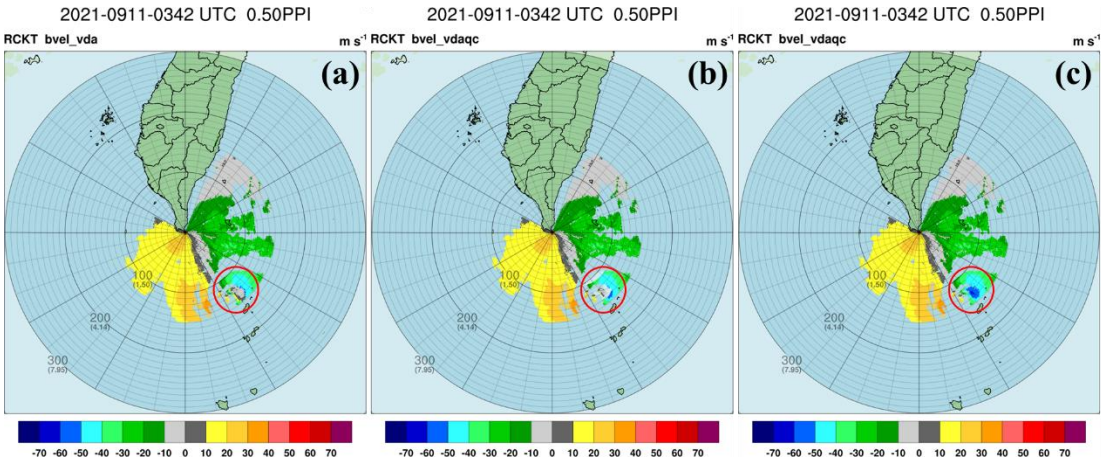

Figure A5: Doppler velocity field observed by the RCKT radar at a 0.5-degree elevation angle on Sep 11, 2021, at 0342 UTC, after processing with (a) VDVD, (b) ICFDA, and (c) ISFDA. Red circles indicate areas with erroneous data that can be corrected by ISFDA.

doi:10.6342/NTU202403267

A2. Table of abbreviations

Abbreviation	Fullname / Definition
DL	Downshear-left
DR	Downshear-right
GBVTD	Ground-based velocity track display
ICFD	Iterative curve fitting dealiasing
ISFD	Iterative surface fitting dealiasing
LMF	Low-level mean flow
NOVR	Data assimilation experiment without assimilating Doppler velocity
RI	Rapid intensification
RMW	Radius of maximu wind
RW	Rapid weakening
TCET	Tropical cyclone eye tracking
UL	Upshear-left
UR	Upshear-left
VDVD	Vortex-based Doppler velocity dealiasing
VRC	Data assimilation experiment with Doppler velocity interpolated to the model grid's constant altitude coordinates
VRP	Data assimilation experiment with Doppler velocity thinned in the radar's original coordinates
VRW	Vortex Rossby wave
VWS	Vertical wind shear

doi:10.6342/NTU202403267

A3. Table of variables

Variable	Definition
$\boldsymbol{R_{max}}$	Radius of the maximum wind
$\boldsymbol{T_s}$	Pulse repetition time
$\boldsymbol{V_d}$	Bbserved Doppler velocity
$\boldsymbol{V_{max}}$	Maximum tangential wind
$\boldsymbol{V_n}$	Nyquist velocity
$\boldsymbol{V_u}$	Unfolded Doppler velocity
$\boldsymbol{V_M}$	Magnitude of mean flow
$\boldsymbol{V_R}$	Axisymmetric radial flow
$\boldsymbol{V_T}$	Axisymmetric tangential flow
$\boldsymbol{V_{T1}}$	Wavenumber-1 component of tangential flow
$\boldsymbol{\theta_M}$	Direction of mean flow
$\boldsymbol{f}$	Doppler frequency
$\boldsymbol{\lambda}$	Wavelength

doi:10.6342/NTU202403267

Reference

蔡雅婷、洪景山、陳依涵、方偉庭、邵彥銘、江琇瑛和馮欽賜，2019: WRF三維變分雷達資料同化個案研究。大氣科學，**47**，94-117。

Alland, J. J., and C. A. Davis, 2022: Effects of surface fluxes on ventilation pathways and the intensification of Hurricane Michael (2018). *J. Atmos. Sci.*, **79**, 1211–1229.

Alland, J. J., B. H. Tang, K. L. Corbosiero, and G. H. Bryan, 2021a: Combined effects of midlevel dry air and vertical wind shear on tropical cyclone development. Part I: Downdraft ventilation. *J. Atmos. Sci.*, **78**, 763–782.

Alland, J. J., B. H. Tang, K. L. Corbosiero, and G. H. Bryan, 2021b: Combined effects of midlevel dry air and vertical wind shear on tropical cyclone development. Part II: Radial ventilation. *J. Atmos. Sci.*, **78**, 783–796.

Altube, P., J. Bech, O. Argemí, T. Rigo, N. Pineda, S. Collis, and J. Helmus, 2017: Correction of dual-PRF doppler velocity outliers in the presence of aliasing. *J. Atmos. Ocean. Technol.*, **34**, 1529–1543.

Askelson, M. A., J.-P. Aubagnac, and J. M. Straka, 2000: An adaptation of the Barnes filter applied to the objective analysis of radar data. *Mon. Wea. Rev.*, **128**, 3050–3082.

Barker, D. M., W. Huang, Y.-R. Guo, A. Bourgeois, and X. N. Xio, 2004: A three-dimensional variational data assimilation system for MM5: Implementation and initial results. *Mon. Wea. Rev.,* **132,** 897–914.

doi:10.6342/NTU202403267

Bell, M. M., and W.-C. Lee, 2002: An objective method to select a consistent set of tropical cyclone circulation centers derived from the GBVTD-simplex algorithm. Preprints, *25th Conf. on Hurricanes and Tropical Meteorology*, San Diego, CA, *Amer. Meteor. Soc.,* 642–643.

Bell, M. M., and W.-C. Lee, 2012: Objective tropical cyclone center tracking using single-Doppler radar. *J. Appl. Meteor. Climatol.,* **51**, 878–896.

Berenguer, M., D. Sempere-Torres, C. Corral, and R. Sánchez-Diezma, 2006: A fuzzy logic technique for identifying nonprecipitating echoes in radar scans. *J. Atmos. Oceanic Technol.*, **23,** 1157–1180.

Black, M. L., J. F. Gamache, F. D. Marks, C. E. Samsury, and H. E. Willoughby, 2002: Eastern Pacific Hurricanes Jimena of 1991 and Olivia of 1994: The effect of vertical shear on structure and intensity. *Mon. Wea. Rev.*, **130,** 2291–2312.

Boehm, A. M., and M. M. Bell, 2021: Retrieved thermodynamic structure of Hurricane Rita (2005) from airborne multi-Doppler radar data. *J. Atmos. Sci.*, **78**, 1583–1605.

Brown, R. A., and V. T. Wood, 1991: On the interpretation of single-Doppler velocity patterns within severe thunderstorms. *Wea. Forecasting*, **6**, 32–48.

Brown, R. A., and V. T. Wood, 2007: A guide for interpreting Doppler velocity patterns: Northern Hemisphere edition. 2nd ed. NOAA/NSSL, 55 pp.

doi:10.6342/NTU202403267

Cha, T.-Y., and M. M. Bell, 2021: Comparison of single-Doppler and multiple-Doppler wind retrievals in Hurricane Matthew (2016). *Atmos. Meas. Tech.*, **14,** 3523–3539.

Cha, T.-Y., M. M. Bell, and A. J. DesRosiers, 2021: Doppler radar analysis of the eyewall replacement cycle of Hurricane Matthew (2016) in vertical wind shear. *Mon. Wea. Rev.*, **149,** 2927–2943.

Chang, P.-L., and P. F. Lin, 2011: Radar anomalous propagation associated with foehn winds induced by Typhoon Krosa (2007). *J. Appl. Meteor. Climatol.*, **50**, 1527–1542.

Chang, P.-L., B. J.-D. Jou, and J. Zhang, 2009a: An algorithm for tracking eyes of tropical cyclones. *Wea. Forecasting,* **24,** 245–261.

Chang, P.-L., P. F. Lin, B. J.-D. Jou, and J. Zhang, 2009b: An application of reflectivity climatology in constructing radar hybrid scans over complex terrains. *J. Atmos. Oceanic Technol.,* **26,** 1315–1327.

Chang, P.-L., W.-T. Fang, P.-F. Lin, and M.-J. Yang, 2019: A vortex-based Doppler velocity dealiasing algorithm for tropical cyclones. *J. Atmos. Oceanic Technol.*, **36**, 1521–1545.

Chang, P.-L., W.-T. Fang, P.-F. Lin, and Y.-S. Tang, 2020: Influence of wind-induced antenna oscillations on radar observations and its mitigation. *Wea. Forecasting*, **35,** 2235-2254.

doi:10.6342/NTU202403267

Chen, B.-F., C. A. Davis, and Y.-H. Kuo, 2019: An idealized numerical study of shear-relative low-level mean flow on tropical cyclone intensity and size. *J. Atmos. Sci.*, **76,** 2309–2334.

Chen, B.-F., C. A. Davis, and Y.-H. Kuo, 2021: Examination of the combined effect of deep-layer vertical shear direction and lower-tropospheric mean flow on tropical cyclone intensity and size based on the ERA5 reanalysis. *Mon. Wea. Rev.*, **149,** 4057–4076.

Chen, H., and S. G. Gopalakrishnan, 2015: A study on the asymmetric rapid intensification of Hurricane Earl (2010) using the HWRF system. *J. Atmos. Sci.*, **72**, 531–550.

Chen, S. S., J. A. Knaff, and F. D. Marks, 2006: Effects of vertical wind shear and storm motion on tropical cyclone rainfall asymmetries deduced from TRMM. *Mon. Wea. Rev.*, **134,** 3190-3208.

Chen, T.-C., S.-Y. Wang, M.-C. Yen, A. J. Clark, and J.-D. Tsay, 2010: Sudden surface warming–drying events caused by typhoon passages across Taiwan. *J. Appl. Meteor. Climatol.*, **49**, 234–252.

Chi, Y.-S., C.-Y. Huang, and W. C. Skamarock, 2024: Track deflection of Typhoon Chanthu (2021) near Taiwan as investigated using a high-Resolution global model. *Mon. Wea. Rev.*, in press.

doi:10.6342/NTU202403267

Chong, M., and O. Bousquet, 2001: On the application of MUSCAT to a ground-based dual-Doppler radar system, *Meteorol. Atmos. Phys.*, **78,** 133–139.

Corbosiero, K. L., and J. Molinari, 2003: The relationship between storm motion, vertical wind shear, and convective asymmetries in tropical cyclones. *J. Atmos. Sci.*, **60**, 366–376.

Dazhang, T., S. G. Geotis, R. E. Passarelli Jr., A. L. Hansen, and C. L. Frush, 1984: Evaluation of an alternating-PRF method for extending the range of unambiguous Doppler velocity. *Preprints, 22d Conf. on Radar Meteorology*, Zurich, Switzerland, *Amer. Meteor. Soc.,* 523–527.

DeMaria, M., 1996: The effect of vertical shear on tropical cyclone intensity change. *J. Atmos. Sci.*, **53**, 2076–2087.

DeMaria, M., and J. Kaplan, 1994: A Statistical Hurricane Intensity Prediction Scheme (SHIPS) for the Atlantic basin. *Wea. Forecasting*, **9,** 209–220.

DeMaria, M., M. Mainelli, L. K. Shay, J. A. Knaff, and J. Kaplan, 2005: Further improvements to the Statistical Hurricane Intensity Prediction Scheme (SHIPS). *Wea. Forecasting*, **20,** 531–543.

DeMaria, M., R. T. DeMaria, J. A. Knaff, and D. Molenar, 2012: Tropical cyclone lightning and rapid intensity change. *Mon. Wea. Rev.*, **140,** 1828–1842.

Donaldson, R. J., 1970: Vortex signature recognition by a Doppler radar. *J. Appl.*

doi:10.6342/NTU202403267

Meteor. Climatol., **9**, 661–670.

Doviak, R. J., and D. S. Zrnic, 1993: *Doppler radar and weather observations*. 2d ed. Academic Press, 562 pp.

Eastin, M. D., W. M. Gray, and P. G. Black, 2005: Buoyancy of convective vertical motions in the inner core of intense Hurricanes. Part II: case studies. *Mon. Wea. Rev.*, **133,** 209–227.

Eilts, M. D., and S. D. Smith, 1990: Efficient dealiasing of Doppler velocities using local environment constraints. *J. Atmos. Oceanic Technol.*, **7,** 118–128.

Fang, W.-T., P.-L. Chang, and M.-J. Yang, 2024: An observational study on the rapid intensification of Typhoon Chanthu (2021) near the complex terrain of Taiwan. *Mon. Wea. Rev.*, **152,** 769-791.

Finocchio, P. M., and R. Rios-Berrios, 2021: The intensity- and size-dependent response of tropical cyclones to increasing vertical wind shear. *J. Atmos. Sci.*, **78,** 3673-3690.

Finocchio, P. M., S. J. Majumdar, D. S. Nolan, and M. Iskandarani, 2016: Idealized tropical cyclone responses to the height and depth of environmental vertical wind shear. *Mon. Wea. Rev.*, **144**, 2155–2175.

Fischer, M. S., P. D. Reasor, B. H. Tang, K. L. Corbosiero, R. D. Torn, and X. Chen, 2023: A tale of two vortex evolutions: using a high-resolution ensemble to assess

doi:10.6342/NTU202403267

the impacts of ventilation on a tropical cyclone rapid intensification event. *Mon. Wea. Rev.*, **151,** 297-320.

Fischer, M. S., R. F. Rogers, and P. D. Reasor, 2020: The rapid intensification and eyewall replacement cycles of Hurricane Irma (2017). *Mon. Wea. Rev.*, **148,** 981–1004.

Frank, W. M., and E. A. Ritchie, 1999: Effects on environmental flow upon tropical cyclone structure. *Mon. Wea. Rev.*, **127,** 2044–2061.

Frank, W. M., and E. A. Ritchie, 2001: Effects of vertical wind shear on the intensity and structure of numerically simulated hurricanes. *Mon. Wea. Rev.*, **129 ,** 2249–2269.

Franklin, J. L., M. L. Black, and K. Valde, 2003: GPS dropwindsonde wind profiles in hurricanes and their operational implications. *Wea. Forecasting*, **18,** 32–44.

Frisch, A. S., L. J. Miller, and R. G. Strauch, 1974: Three-dimensional air motion measured in snow. *Geophys. Res. Lett.*, **1**, 86–89.

Frush, C. L., 1991: A graphical representation of the radar velocity dealiasing problem. Preprints, *25th Int. Conf. on Radar Meteoroloy*, Paris, France, *Amer. Meteor. Soc.*, 885-888.

doi:10.6342/NTU202403267

Fu, H., Y. Wang, M. Riemer, and Q. Li, 2019: Effect of unidirectional vertical wind shear on tropical cyclone intensity change—Lower-layer shear versus upper-layer shear. *Journal of Geophysical Research: Atmospheres*, **124,** 6265–6282.

Gao, J., M. Xue, A. Shapiro, and K. K. Droegemeier, 1999: A variational method for the analysis of three-dimensional wind fields from two Doppler radars. *Mon. Wea. Rev.*, **127**, 2128–2142.

Gong, J., L. Wang, and Q. Xu, 2003: A three-step dealiasing method for Doppler velocity data quality control. *J. Atmos. Oceanic Technol*., **20,** 1738–1748.

Guimond, S. R., P. D. Reasor, G. M. Heymsfield, and M. M. McLinden, 2020: The dynamics of vortex Rossby waves and secondary eyewall development in Hurricane Matthew (2016): New insights from radar measurements. *J. Atmos. Sci. 77***,** 2349–2374.

Guinn, T. A., and W. H. Schubert, 1993: Hurricane spiral bands. *J. Atmos. Sci.*, **50**, 3380–3403.

Heideman, M. T., D. H. Johnson, and C. S. Burrus, 1985: Gauss and the history of the fast Fourier transform. *Arch. Hist. Exact Sci.*, **34**, 265–277.

Heng, J., S. Yang, Y. Gong, J. Gu, and H. Liu, 2020: Characteristics of the convective bursts and their relationship with the rapid intensification of Super Typhoon Maria (2018). *Atmos. Oceanic Sci. Lett.*, **13**, 146–154.

doi:10.6342/NTU202403267

Hersbach, H., and Coauthors, 2020: The ERA5 global reanalysis. *Quart. J. Royal. Meteor. Soc.,* **146,** 1999–2049.

Hong, S.-Y., and J.-O. J. Lim, 2006: The WRF single-moment 6-class microphysics scheme (WSM6). *J. Korean Meteor. Soc.,* **42,** 129–151.

Hong, S.-Y., Y. Noh, and J. Dudhia, 2006: A new vertical diffusion package with an explicit treatment of entrainment processes. *Mon. Wea. Rev.*, **134**, 2318–2341.

Hsiao, L. F., C. S. Liou, T. C. Yeh, Y. R. Guo, D. S. Chen, K. N. Huang, C. T. Terng, and J. H. Chen, 2010: A vortex relocation scheme for tropical cyclone initialization in Advanced Research WRF. *Mon. Wea. Rev.*, **138**, 3298–3315.

Hsiao, L. F., D.-S. Chen, Y.-H. Kuo, Y.-R. Guo, T. C. Yeh, J.-S. Hong, C.-T. Fong, and C.-S. Lee, 2012: Application of WRF 3DVAR to operational typhoon prediction in Taiwan: Impact of outer loop and partial cycling approaches. *Wea. Forecasting*, **27**, 1249–1263.

Hsu, L.-H., H.-C. Kuo, and R. G. Fovell, 2013: On the geographic asymmetry of typhoon translation speed across the mountainous island of Taiwan. *J. Atmos. Sci.*, **70,** 1006–1022.

Hsu, L.-H., S.-H. Su, and H.-C. Kuo, 2021: A numerical study of the sensitivity of typhoon track and convection structure to cloud microphysics. *J. Geo. Res.: Atmospheres*, **126**, 1–17.

doi:10.6342/NTU202403267

Hsu, L.-H., S.-H. Su, R. G. Fovell, and H.-C. Kuo, 2018: On typhoon track deflections near the east coast of Taiwan. *Mon. Wea. Rev.*, **146**, 1495–1510.

Hu, Y., and X. Zou, 2021: Tropical cyclone center positioning using single channel microwave satellite observations of brightness temperature. *Remote Sens.*, **13,** 2466.

Huang, C.-Y., C.-A. Chen, S.-H. Chen, and D. S. Nolan, 2016: On the upstream track deflection of tropical cyclones past a mountain range: Idealized experiments. *J. Atmos. Sci.*, **73**, 3157–3180.

Huang, C.-Y., C.-H. Huang, and W. C. Skamarock, 2019: Track deflection of Typhoon Nesat (2017) as realized by multiresolution simulations of a global model. *Mon. Wea. Rev.*, **147**, 1593–1613.

Huang, C.-Y., T.-C. Juan, H.-C. Kuo, and J.-H. Chen, 2020: Track deflection of Typhoon Maria (2018) during a westbound passage offshore of northern Taiwan: topographic influence. *Mon. Wea. Rev.*, **148,** 4519–4544.

Huang, H.-L., M.-J. Yang, and C.-H. Sui, 2014: Water budget and precipitation efficiency of Typhoon Morakot (2009). *J. Atmos. Sci.*, **71,** 112–129.

Huang, K.-C., and C.-C. Wu, 2018: The impact of idealized terrain on upstream tropical cyclone track. *J. Atmos. Sci.*, **75**, 3887–3910.

Huang, Y.-H., C.-C. Wu, and Y. Wang, 2011: The influence of island topography on typhoon track deflection. *Mon. Wea. Rev.*, **139,** 1708–1727.

doi:10.6342/NTU202403267

Iacono, M. J., J. S. Delamere, E. J. Mlawer, M. W. Shephard, S. A. Clough, and W. D. Collins, 2008: Radiative forcing by long–lived greenhouse gases: Calculations with the AER radiative transfer models. *J. Geophys. Res.*, **113,** D13103.

Janjić, T., and Coauthors, 2018: On the representation error in data assimilation. *Quart. J. Roy. Meteor. Soc.*, **144**, 1257–1278.

Jian, G.-J., and C.-C. Wu, 2008: A numerical study of the track deflection of Supertyphoon Haitang (2005) prior to its landfall in Taiwan. *Mon. Wea. Rev.*, **136**, 598–615.

Jones, S. C., 1995: The evolution of vortices in vertical shear. Part I: Initially barotropic vortices. *Quart. J. Roy. Meteor. Soc*, **121,** 821–851.

Jorgensen, D. P., 1984a: Mesoscale and convective-scale characteristics of mature hurricanes. Part I: General observations by research aircraft. *J. Atmos. Sci.*, **41**, 1268–1285.

Jorgensen, D. P., 1984b: Mesoscale and convective-scale characteristics of mature hurricanes. Part II: Inner core structure of Hurricane Allen (1980). *J. Atmos. Sci.*, **41**, 1287–1131.

Jorgensen, D. P., T. R. Shepherd, and A. S. Goldstein, 2000: A dual-pulse repetition frequency scheme for mitigating velocity ambiguities of the NOAA P-3 airborne Doppler radar. *J. Atmos. Oceanic Technol.*, **17**, 585–594.

doi:10.6342/NTU202403267

Jorgensen, D. P., T. R. Shepherd, and A. S. Goldstein, 2000: A dual-pulse repetition frequency scheme for mitigating velocity ambiguities of the NOAA P-3 airborne Doppler radar. *J. Atmos. Oceanic Technol.*, **17,** 585–594.

Jou, B. J.-D., W. C. Lee, S. P. Liu, and Y. C. Kao, 2008: Generalized VTD retrieval of atmospheric vortex kinematic structure. Part I: Formulation and error analysis. *Mon. Wea. Rev.*, **136,** 995–1012

Kao, Y. -C., B. J.-D. Jou, J. C -L. Chan, and W. -C Lee, 2019: An observational study of a coastal barrier jet induced by a landfalling typhoon. *Mon. Wea. Rev.*, **147,** 4589–4609.

Kaplan, J., and Coauthors, 2015: Evaluating environmental impacts on tropical cyclone rapid intensification predictability utilizing statistical models. *Wea. Forecasting*, **30**, 1374–1396.

Knapp, K. R., C. S. Velden, and A. J. Wimmers, 2018: A global climatology of tropical cyclone eyes. *Mon. Wea. Rev.*, **146,** 2089–2101.

Kuo, H.-C., R. T. Williams, and J.-H. Chen, 1999: A possible mechanism for the eye rotation of typhoon Herb. *J. Atmos. Sci.*, **56**, 1659–1673.

Lakshmanan, V., A. Fritz, T. Smith, K. Hondl, and G. Stumpf, 2007: An automated technique to quality control radar reflectivity data. *J. Appl. Meteor. Climatol.*, **46,** 288–305.

doi:10.6342/NTU202403267

Lee, C.-S., Y.-C. Liu, and F.-C. Chien, 2008: The secondary low and heavy rainfall associated with Typhoon Mindulle (2004). *Mon. Wea. Rev.*, **136,** 1260–1283.

Lee, T.-Y., C.-C. Wu, and R. Rios-Berrios, 2021: The role of low-level flow direction on tropical cyclone intensity changes in a moderate-sheared environment. *J. Atmos. Sci.*, **78,** 2859–2877.

Lee, W.-C., and F. D. Marks, 2000: Tropical cyclone kinematic structure retrieved from single-Doppler radar observations. Part II: The GBVTD-simplex center finding algorithm. *Mon. Wea. Rev.*, **128,** 1925–1936.

Lee, W.-C., B. J.-D. Jou, P.-L. Chang, and F. D. Marks Jr., 2000: Tropical cyclone kinematic structure retrieved from single-Doppler radar observations. Part III: Evolution and structure of Typhoon Alex (1987). *Mon. Wea. Rev.,* **128**, 3982–4001.

Lee, W.-C., B. J.-D. Jou, P.-L. Chang, and S.-M. Deng, 1999: Tropical cyclone kinematic structure retrieved from single-Doppler radar observations. Part I: Interpretation of Doppler velocity patterns and the GBVTD technique. *Mon. Wea. Rev.*, **127**, 2419–2439.

Lemon, L. R., D. W. Burgess, and R. A. Brown, 1978: Tornadic storm airflow and morphology derived from single-Doppler radar measurements. *Mon. Wea. Rev.*, **106**, 48–61.

Lhermitte, R. M, and D. Atlas 1961: Precipitation motion by Pulse Doppler radar.

doi:10.6342/NTU202403267

Proceedings of the 9th Weather Radar Conference, Boston, *Amer. Meteor. Soc*, 218-233.

Lhermitte, R., 1970: Dual-Doppler radar observations of convective storm circulation. *Preprints 14th Radar Meteorology Conference*, Tucson, Ariz., *Amer. Meteor. Soc.*, 139-144.

Liang, J., L. Wu, and G. Gu, 2018: Rapid weakening of tropical cyclones in monsoon gyres over the tropical Western North Pacific. *J. Clim.,* **31,** 1015–1028.

Liang, J., L. Wu, G. Gu, and Q. Liu, 2016: Rapid weakening of Typhoon Chan-Hom (2015) in a monsoon gyre. *J. Geophys. Res. Atmos.*, **121,** 9508–9520.

Lin, Y. L., D. B. Ensley, S. Chiao, and C. Y. Huang, 2002: Orographic influences on rainfall and track deflection associated with the passage of a tropical cyclone. *Mon. Wea. Rev.*, **130,** 2929-2950.

Lin, Y.-F., C.-C. Wu, T.-H. Yen, Y.-H. Huang, and G.-Y. Lien, 2020: Typhoon Fanapi (2010) and its interaction with Taiwan terrain – Evaluation of the uncertainty in track, intensity and rainfall simulations. *J. Meteorol. Soc. Japan. Ser. II*, **98,** 93–113.

Liou, Y.-C., and Y.-J. Chang, 2009: A variational multiple–Doppler radar three-dimensional wind synthesis method and its impacts on thermodynamic retrieval. *Mon. Wea. Rev.*, **137,** 3992–4010.

doi:10.6342/NTU202403267

Liou, Y.-C., T.-C. Chen Wang, and P.-Y. Huang, 2016: The inland eyewall reintensification of Typhoon Fanapi (2010) documented from an observational perspective using multiple-Doppler radar and surface measurements. *Mon. Wea. Rev.*, **144,** 241–261.

Liu, H., and V. Chandrasekar, 2000: Classification of hydrometeors based on polarimetric radar measurements: Development of fuzzy logic and neuro-fuzzy systems, and in situ verification. *J. Atmos. Oceanic Technol.*, **17,** 140–164.

Loew, E., and C. A. Walther; 1995: Real-time spectral moment calculations for a multi-frequency doppler radar. *Preprints, 9th Symp. on Meteor. Observ. and Instrumentation,* 27-31 March, 405–407.

Lorsolo, S., and A. Aksoy, 2012: Wavenumber analysis of azimuthally distributed data: Assessing maximum allowable gap size. *Mon. Wea. Rev.*, **140**, 1945–1956.

Marks, F. D., Jr., and R. A. Houze, Jr., 1987: Inner core structure of hurricane Alicia from airborne Doppler radar observations. *J. Atmos. Sci.*, **44,** 1296–1317.

May, P. T., 2001: Mesocyclone and microburst signature distortion with dual PRT radar. *J. Atmos. Oceanic Technol.,* **18,** 1229–1233.

Mazzarella, V., I. Maiello, R. Ferretti, V. Capozzi, E. Picciotti, P. P. Alberoni, F. S. Marzano, and G. Budillon, 2020: Reflectivity and velocity radar data assimilation for two flash flood events in central Italy: A comparison between 3D and 4D

doi:10.6342/NTU202403267

variational methods. *Quart. J. Roy. Meteor. Soc.*, **146**, 348–366.

Montgomery, M. T., and R. J. Kallenbach, 1997: A theory for vortex Rossby-waves and its application to spiral bands and intensity changes in hurricanes. *Quart. J. Roy. Meteor. Soc.*, **123,** 435–465.

Murillo, S. T., W. Lee, M. M. Bell, G. M. Barnes, F. D. Marks, and P. P. Dodge, 2011: Intercomparison of Ground-Based Velocity Track Display (GBVTD)-retrieved circulation centers and structures of Hurricane Danny (1997) from two coastal WSR-88Ds. *Mon. Wea. Rev.*, **139**, 153–174.

Pan, X., X. Tian, X. Li, Z. Xie, A. Shao, and C. Lu, 2012: Assimilating Doppler radar radial velocity and reflectivity observations in the weather research and forecasting model by a proper orthogonal-decomposition-based ensemble, three-dimensional variational assimilation method. *J. Geophys. Res.*, **117**, D17113.

Potvin, C. K., D. Betten, L. J. Wicker, K. L. Elmore, and M. I. Biggerstaff, 2012: 3DVAR versus traditional dual-Doppler wind retrievals of a simulated supercell thunderstorm. *Mon. Wea. Rev.*, **140**, 3487–3494.

Rappin, E. D., and D. S. Nolan, 2012: The effect of vertical shear orientation on tropical cyclogenesis. *Q. J. R. Meteorol. Soc.*, **138,** 1035–1054.

Ray, P. S., R. J. Doviak, G. B. Walker, D. Sirmans, J. Carter, and B. Bumgarner, 1975: Dual-Doppler observation of a tornadic storm. *J. Appl. Meteor.,* **14,** 1521–1530.

doi:10.6342/NTU202403267

Reasor, P. D., and M. D. Eastin, 2012: Rapidly intensifying Hurricane Guillermo (1997). Part II: Resilience in shear. *Mon. Wea. Rev.*, **140,** 425–444.

Reasor, P. D., M. D. Eastin, and J. F. Gamache, 2009: Rapidly intensifying Hurricane Guillermo (1997). Part I: Low-wavenumber structure and evolution. *Mon. Wea. Rev.*, **137,** 603–631.

Reasor, P. D., R. Rogers, and S. Lorsolo, 2013: Environmental flow impacts on tropical cyclone structure diagnosed from airborne Doppler radar composites. *Mon. Wea. Rev.*, **141,** 2949–2969.

Rennie, S., L. Rikus, N. Eizenberg, P. Steinle, and M. Krysta, 2020: Impact of Doppler radar wind observations on Australian high-resolution numerical weather prediction. *Wea. Forecasting*, **35**, 309–324.

Riemer, M., M. T. Montgomery, and M. E. Nicholls, 2010: A new paradigm for intensity modification of tropical cyclones: Thermodynamic impact of vertical wind shear on the inflow layer. *Atmos. Chem. Phys.*, **10**, 3163–3188, doi:10.5194/acp-10-3163-2010.

Rihan, F. A., C. G. Collier, S. P. Ballard, and S. Swarbrick, 2008: Assimilation of Doppler radial winds into a 3D-Var system: Errors and impact of radial velocities on the variational analysis and model forecasts. *Quart. J. Roy. Meteor. Soc.*, **134**, 1701–1716.

doi:10.6342/NTU202403267

Rios-Berrios, R., and R. D. Torn, 2017: Climatological analysis of tropical cyclone intensity changes under moderate vertical wind shear. *Mon. Wea. Rev.*, **145,** 1717-1738.

Ryglicki, D. R., Velden, C. S., Reasor, P. D., Hodyss, D., and Doyle, J. D., 2021: Observations of atypical rapid intensification characteristics in Hurricane Dorian (2019). *Mon. Wea. Rev*. **149,** 2131–2150.

Shapiro, A., C. K. Potvin, and J. Gao, 2009: Use of a vertical vorticity equation in variational dual-Doppler wind analysis. *J. Atmos. Oceanic Technol.*, **26,** 2089–2106.

Shimada, U., 2022: Variability of environmental conditions for tropical cyclone rapid intensification in the western North Pacific. *J. Clim.*, **35,** 4437–4454.

Simonin, D., S. P. Ballard, and Z. Li, 2014: Doppler radar radial wind assimilation using an hourly cycling 3D-Var with a 1.5 km resolution version of the Met Office Unified Model for nowcasting. *Quart. J. Roy. Meteor. Soc.*, **140**, 2298–2314.

Sirmans, D., D. S. Zrnic, and B. Bumgarner, 1976: Extension of maximum unambiguous Doppler velocity by use of two sampling rates. *Preprints, 17th Conf. on Radar Meteorology,* Seattle, WA, Amer. Meteor. Soc., 23–28.

Sun, J., and N. A. Crook, 2001: Real-time low-level wind and temperature analysis using single WSR-88D data. *Wea. Forecasting*, **16**, 117–132.

doi:10.6342/NTU202403267

Tabary, P., F. Guiber, L. Périer, and J. Parent-du-Châtelet, 2006: An operational triple-PRT Doppler scheme for the French radar network. *J. Atmos. Oceanic Technol.*, **23**, 1645–1656.

Tabary, P., G. Scialom, and U. Germann, 2001: Real-time retrieval of the wind from aliased velocities measured by Doppler radars. *J. Atmos. Oceanic Technol.*, **18**, 875–882.

Tang, C. K., and J. C. Chan, 2015: Idealized simulations of the effect of local and remote topographies on tropical cyclone tracks. *Quart. J. Roy. Meteor. Soc.*, **141**, 2045–2056.

Tang, C. K., and J. C. L. Chan, 2014: Idealized simulations of the effect of Taiwan and Philippines topographies on tropical cyclone tracks. *Quart. J. Roy. Meteor. Soc.*, **140**, 1578–1589.

Tewari, M., F. Chen, W. Wang, J. Dudhia, M. A. LeMone, K. Mitchell, M. Ek, G. Gayno, J. Wegiel, and R. H. Cuenca, 2004: Implementation and verification of the unified NOAH land surface model in the WRF model. *20th conference on weather analysis and forecasting/16th conference on numerical weather prediction,* pp. 11–15.

doi:10.6342/NTU202403267

Torgerson, W. S., J. Schwendike, A. Ross, and C. Short, 2023a: Comparing short term intensity fluctuations and an Eyewall replacement cycle in Hurricane Irma (2017) during a period of rapid intensification. *EGUsphere,* 2023, 1-36.

Torgerson, W., J. Schwendike, A. Ross, and C. J. Short, 2023b: Intensity fluctuations in Hurricane Irma (2017) during a period of rapid intensification. *Wea. Climate Dyn.,* **4,** 331-359.

Velden, C., and L. Leslie, 1991: The basic relationship between tropical cyclone intensity and the depth of the environmental steering layer in the Australian region. *Wea. Forecasting*, **6**, 244–253

Vinour, L., S. Jullien, A. Mouche, C. Combot, and M. Mangeas, 2021: Observations of tropical cyclone inner-Core fine-scale structure, and its link to intensity variations. *J. Atmos. Sci.*, **78,** 3651–3671.

Wada, A., 2021: Roles of oceanic mesoscale eddy in rapid weakening of Typhoons Trami and Kong-Rey in 2018 simulated with a 2-km-mesh atmosphere-wave-ocean coupled model. *J. Meteorol. Soc. Japan. Ser. II*, **99,** 1453–1482.

Wadler, J. B., J. J. Cione, J. A. Zhang, E. A. Kalina, and J. Kaplan, 2022: The effects of environmental wind shear direction on tropical cyclone boundary layer thermodynamics and intensity change from multiple observational datasets. *Mon. Wea. Rev.,* **150,** 115-134.

doi:10.6342/NTU202403267

Waldteufel P, and Corbin H. 1979: On the analysis of single Doppler data. *J. Appl. Meteorol.* **18,** 532–542.

Wang, M., K. Zhao, W. C. Lee, B. J.-D. Jou, and M. Xue, 2012: The gradient velocity track display (GrVTD) technique for retrieving tropical cyclone primary circulation from aliased velocities measured by single-Doppler radar. *J. Atmos. Oceanic Technol.*, **29**, 1026–1041.

Wang, Y.-F., and Z.-M. Tan, 2020: Outer rainbands-driven secondary eyewall formation of tropical cyclones. *J. Atmos. Sci.*, **77**, 2217–2236

Wong, M. L. M., and J. C. L. Chan, 2004: Tropical cyclone intensity in vertical wind shear. *J. Atmos. Sci.*, **61**, 1859–1876.

Wood, K. M., and E. A. Ritchie, 2015: A definition for rapid weakening of North Atlantic and eastern North Pacific tropical cyclones. *Geophys. Res. Lett.,* **42,** 10,091–10,097.

Wood, V. T., and R. A. Brown, 1992: Effects of radar proximity on single-Doppler velocity signatures of axisymmetric rotation and divergence. *Mon. Wea. Re*v., **120,** 2798–2807.

Wu, C.-C., 2013: Typhoon Morakot: Key findings from the journal TAO for improving prediction of extreme rains at landfall. *Bull. Amer. Meteor. Soc.*, **94,** 155–160.

doi:10.6342/NTU202403267

Wu, C.-C., T.-H. Li, and Y.-H. Huang, 2015: Influence of mesoscale topography on tropical cyclone tracks: Further examination of the channeling effect. *J. Atmos. Sci.*, **72**, 3032–3050.

Wu, C.-C., and Y-H. Kuo, 1999: Typhoons affecting Taiwan: Current understanding and future challenges. *Bull. Amer. Meteor. Soc.,* **80,** 67–80.

Wu, C.-C., T.-H. Yen, Y.-H. Kuo, and W. Wang, 2002: Rainfall simulation associated with Typhoon Herb (1996) near Taiwan. Part I: The topographic effect. *Wea. Forecasting***, 17,** 1001–1015.

Xiao, Q., Y. Kuo, J. Sun, W. Lee, E. Lim, Y. Guo, and D. M. Barker, 2005: Assimilation of Doppler radar observations with a regional 3DVAR System: Impact of Doppler velocities on forecasts of a heavy rainfall case. *J. Appl. Meteor.*, **44**, 768–788

Xu, Q., P. Zhang, S. Liu, and D. Parrish, 2011: A VAD-based dealiasing method for radar velocity data quality control. *J. Atmos. Oceanic Technol.*, **28,** 50–62.

Yang, M.-J., D.-L. Zhang, and H.-L. Huang, 2008: A modeling study of Typhoon Nari (2001) at landfall. Part I: Topographic effects. *J. Atmos. Sci.*, **65,** 3095–3115.

Yang, M.-J., D.-L. Zhang, X.-D. Tang, and Y. Zhang, 2011a: A modeling study of Typhoon Nari (2001) at landfall: 2. Structural changes and terrain-induced asymmetries, *J. Geophys. Res.*, **116,** D09112, doi:10.1029/2010JD015445.

doi:10.6342/NTU202403267

Yang, M.-J., S. A. Braun, and D.-S. Chen, 2011b: Water budget of Typhoon Nari (2001). *Mon. Wea. Rev.*, **139,** 3809–3828.

Yang, M.-J., Y.-C. Wu, and Y.-C. Liou, 2018: The study of inland eyewall reformation of Typhoon Fanapi (2010) using numerical experiments and vorticity budget analysis. *J. Geophys. Res. Atmos.*, **123,** 9604–9623, https://doi. org/10.1029/2018JD02828.

Yeh, T.-C., and R. L. Elsberry, 1993a: Interaction of typhoons with the Taiwan topography. Part I: Upstream track deflections. *Mon. Wea. Rev.*, **121**, 3193–3212.

Yeh, T.-C., and R. L. Elsberry, 1993b: Interaction of typhoons with the Taiwan topography. Part II: Continuous and discontinuous tracks across the island. *Mon. Wea. Rev.*, **121**, 3213–3233.

Yeh, T.-C., L.-F. Hsiao, D.S. Chen, and K.-N. Huang, 2012: A study on terrain-induced tropical cyclone looping in East Taiwan: case study of Typhoon Haitang in 2005. *Nat. Hazards*, **63,** 1497–1514.

Yu, C.-K., and L.-W. Cheng, 2013: Distribution and mechanisms of orographic precipitation associated with Typhoon Morakot (2009). *J. Atmos. Sci.*, **70,** 2894–2915.

Zhang, J. A., and E. W. Uhlhorn, 2012: Hurricane sea surface inflow angle and an observation-based parametric model. *Mon. Wea. Rev.*, **140**, 3587–3605.

Zhang, J., and S. Wang, 2006: An automated 2D multipass Doppler radar dealiasing scheme. *J. Atmos. Oceanic Technol.,* **23,** 1239–1248.

doi:10.6342/NTU202403267

Zrnic, D. S., and P. Mahapatra, 1985: Two methods of ambiguity resolution in pulsed Doppler weather radars. *IEEE Trans. Aerosp. Electron. Syst.*, **16**, 1351–1363.

doi:10.6342/NTU202403267